SOLUTION CHARACTERIZATION OF

INORGANIC NANOSCALE CLUSTER SPECIES VIA ^{1}H-NMR AND DOSY

by

ANNA F. OLIVERI

A DISSERTATION

Presented to the Department of Chemistry and Biochemistry
and the Graduate School of the University of Oregon
in partial fulfillment of the requirements
for the degree of
Doctor of Philosophy

December 2014

DISSERTATION APPROVAL PAGE

Student: Anna F. Oliveri

Title: Solution Characterization of Inorganic Nanoscale Cluster Species via ^{1}H-NMR and DOSY

This thesis has been accepted and approved in partial fulfillment of the requirements for the Doctor of Philosophy degree in the Department of Chemistry and Biochemistry by:

Catherine J. Page	Chair
Darren W. Johnson	Advisor
Kenneth M. Doxsee	Core Member
Mark Reed	Institutional Representative

and

J. Andrew Berglund	Dean of the Graduate School

Original approval signatures are on file with the University of Oregon Graduate School

Degree awarded December 2014

DISSERTATION ABSTRACT

Anna F. Oliveri

Doctor of Philosophy

Department of Chemistry and Biochemistry

December 2014

Title: Solution Characterization of Inorganic Nanoscale Cluster Species via ^{1}H-NMR and DOSY

Completely inorganic nanoscale clusters play an essential role in many aspects of inorganic chemistry, materials chemistry, and geochemistry. The underlying dynamic behavior of these species in solution defines how and why they make successful thin film precursors as well as exist naturally in the environment. There have been a limited number of previous solution studies involving inorganic nanoscale clusters due to the lack of spectroscopic handles and availability of analytical techniques. This dissertation outlines the available and appropriate characterization techniques needed for identifying and studying inorganic nanoscale species and then uses proton Nuclear Magnetic Resonance (^{1}H-NMR) and Diffusion Ordered Spectroscopy (DOSY) to fully characterize the $Ga_{13-x}In_x(\mu_3\text{-}OH)_6(\mu\text{-}OH)_{18}(H_2O)_{24}(NO_3)_{15}$ ($0 \leq x \leq 6$) cluster series in solution. This research lays a foundation for a multitude of future studies on the dynamic behavior of these species that was previously unachievable.

This dissertation includes previously published and unpublished co-authored material.

CURRICULUM VITAE

NAME OF AUTOR: Anna F. Oliveri

GRADUATE AND UNDERGRADUATE SCHOOLS ATTENDED:

University of Oregon, Eugene, Oregon
Juniata College, Huntingdon, Pennsylvania

DEGREES AWARDED:

Doctor of Philosophy, Chemistry, 2014, University of Oregon
Master of Science, Chemistry, 2010, University of Oregon
Bachelor of Science, Chemistry, Education (Minor), 2009, Juniata College

AREAS OF SPECIAL INTEREST:

Solution Analysis of Inorganic Nanoscale Clusters
Science Outreach and Education

PROFESSIONAL EXPERIENCE:

Outreach/Education Fellow, NSF CSMC, Hermiston, Oregon, 2012-2014

GK-12 Teaching Fellow, NSF, Heppner, Oregon, 2011-2012

Teaching Assistant, Department of Chemistry, University of Oregon, Eugene, 2009-2010

Lab Assistant, Science in Motion, Huntingdon, Pennsylvania, 2005-2009

Summer Research Intern, University Palackého, Olomouc, Czech Republic, 2008

Summer Research Intern, Pacific Northwest National Lab, Richland, Washington 2007

GRANTS, AWARDS, AND HONORS:

NSF CSMC Outreach/Education Fellowship, 2012-2014

NSF GK-12 Fellowship, 2011-2012

Graduate Teaching Fellowship, Chemistry, 2009-2011

Rockwell Chemistry Prize, Juniata College, 2009

Cum Laude, Juniata College, 2009

PUBLICATIONS:

Oliveri, A. F.; Wills, L. A.; Hazlett, C. R.; Carnes, M. E.; Chang, I.-Y.; Cheong, P. H.-Y.; Johnson, D. W. "Solution Phase Structural Characterization of an Array of Nanoscale Aqueous Inorganic $Ga_{13-x}In_x$ ($0 \leq x \leq 6$) Clusters by ^{1}H-NMR and QM Computations" *Journal of the American Chemical Society.* **2014**, Submitted.

Carnes, M. E; Knutson, C. C.; Nadarajah, A.; Jackson Jr., M. N.; Oliveri, A. F.; Norelli, K. M.; Crockett, B. M.; Bauers, S. R; Moreno-Luna, H. A.; Taber, B. N.; Pacheco, D. J.; Olson, J. Z.; Brevick, K. R.; Sheehan, C. E.; Johnson, D. W.; Boettcher, S. W. "Electrochemical Synthesis of Flat-$[Ga_{13-x}In_x(\mu_3\text{-}OH)_6(\mu\text{-}OH)_{18}(H_2O)_{24}(NO_3)_{15}]$ Clusters as Aqueous Precursors for Solution-Processed Semiconductors" *Journal of Materials Chemistry C.* **2014**, 2(40), 8492-8496.

Oliveri, A. F.; Elliott, E. W.; Carnes, M. E.; Hutchison, J. E.; Johnson, D. W. "Elucidating Inorganic Nanoscale Species in Solution: Complementary and Corroborative Approaches" *ChemPhysChem : A European Journal of Chemical Physics and Physical Chemistry.* **2013**, 14(12), 2655–2661.

Oliveri, A. F.; Carnes, M. E.; Baseman, M. M.; Richman, E. K.; Hutchison J. E.; Johnson, D. W., "Single Nanoscale Cluster Species Revealed by ^{1}H-NMR Diffusion-Ordered Spectroscopy and Small-Angle X-ray Scattering" *Angewandte Chemie International Edition.* **2012**, 51(44), 10992-10996.

Kouzes, R. T.; Ely, J.H.; Seifert, A.; Siciliano, E. R.; Weirer, D. R.; Windsor, L. K.; Woodring, M. L.; Borgardt, G.; Buckley, E.; Flumerfelt, E.; Oliveri, A. F.; Salvitti, M., "Cosmic-Ray-Induced Ship-Effect Neutron Measurements and Implications for Cargo Scanning at Borders" *Nuclear Instruments and Methods in Physics Research A.* **2007**, 587, 89–100.

ACKNOWLEDGMENTS

I would like to thank the following people for helping me successfully reach this point in my life.

Family: Wendy Weyant, Tony Oliveri, John Allison, Vikki Latta, Grandma Pat Smith, Grandpa Jim Smith, Grandma Anna Weyant, Grandpa Jack Allison, Grandma Dottie Allison, my entire extended Oliveri, Weyant, and Allison families, my best friend Hilary Wicks (Getz), and my god parents Carol Eklund and Lewin Wicks.

Teachers: Greenwood Elementary (Mrs. Magill, Mrs. Cameron, Mrs. Numer, Mrs. Weger, Mr. Stroup, Mrs. Watts, Mrs. Blair, Mr. King, Miss Sinner, Mrs. Gregory, Mr. Syslo, Señora Bendorf) and Greenwood High School (Mr. Houser, Mrs. Miller, Mrs. Rice, Mr. Rice, Mr. Gantt, Mrs. Gantt, Mrs. Deimler, Mrs. Selby, Mrs. Jones, Señora Holtz, Mr. Folk, Mrs. Roberts, Mr. Lyter, Mr. T. Magill, Mr. J. Magill, and Mrs. Troutman).

Professors: Juniata College (Dr. I. Dave Reingold, Dr. Richard Hark, Dr. Ruth Reed, Dr. Tom Fisher, Dr. Peter Baran, Dr. Paul Schettler, Dr. Loraine Mulfinger, Dr. James Brogardt, and Dr. Kathy Jones) and University of Oregon, my graduate advisor (Dr. Darren W. Johnson), and my graduate committee (Dr. Cathy Page, Dr. Ken Doxsee, and Dr. Mark Reed).

Friends: My supervisor at SIM Tara Yorke (Fitzsimmons), my fellow hellbenders (Kelly McErlean), my past room/housemates (Emma Houck, Dr. Bryan Nell, Dr. Emma Downs, Dr. Michelle Watt, Dr. Edmundo Guzmán Percástegui, Dr. Lena Trotochaud, and Kara Nell), my lab mates in the DWJ lab, my undergraduate mentee Caitlyn Hazlett, and **all** of my other friends.

This work is dedicated to Brandon Heath Wellentin, who would be tremendously proud of my progress, resolve, and success despite the situation.

TABLE OF CONTENTS

Chapter Page

Chapter Page

Chapter Page

LIST OF FIGURES

Figure Page

Figure Page

LIST OF TABLES

LIST OF SCHEMES

Scheme Page

CHAPTER I

ELUCIDATING INORGANIC NANOSCALE SPECIES IN SOLUTION: COMPLEMENTARY AND CORROBORATIVE APPROACHES

Contributions

As co-first authors of this requested concept piece, Dr. Edward W. Elliot III and I outlined the importance of using complementary and corroborative techniques when measuring size of a nanoscale species in solution. This manuscript was requested by *ChemPhysChem* after our initial $\mathbf{Ga_{13}}$ results were published in *Angewandte Chemie International Edition* (Chapter II). With the help of Dr. Matthew E. Carnes, we wrote and edited this "*Concept*" article resulting in a request for cover art. I made the majority of the images for this manuscript. Prof. James E. Hutchison and Prof. Darren W. Johnson were the principle investigators for this work and provided editorial assistance. This concept piece was published with cover art in 2013 in *ChemPhysChem: A European Journal of Chemical Physics and Physical Chemistry*, a publication of Wiley-VCH Verlag GmbH & Co. KGaA, volume 14 pages 2655-2661.[1]

Introduction

Corroborating the solid-state structure to solution structure and elucidating solution dynamics have been challenging goals confronted by many researchers, particular in supramolecular chemistry and nanoscience. If a substance can be crystallized, solid-state structures can confidently be determined using single crystal X-ray diffraction (XRD), but what exists in the solid-state does not always reflect the

relevant species in solution. Small molecule synthetic chemists have adopted a set of complementary techniques commonly used to identify and confirm a molecular structure in solution (NMR, UV-Vis, IR, and Mass Spec).[2] Inorganic clusters, nanoparticles, and related species, together referred to henceforth as "inorganic nanoscale species", are not as easily structurally characterized using these techniques. In this Chapter, the complementary combination of Small Angle X-ray Scattering (SAXS) and Diffusion Ordered SpectroscopY (DOSY), as well as other analytical techniques, are reviewed and discussed for their use in the study of inorganic nanoscale species.

The dynamic behavior of inorganic nanoscale species in solution is of fundamental interest to inorganic, materials, and geological chemists; however, it is first necessary to identify the predominant species in solution before more thorough investigations can occur. One such inorganic nanoscale species which possesses interesting solution behavior is the cluster $Ga_7In_6(\mu_3\text{-}OH)_6(\mu\text{-}OH)_{18}(H_2O)_{24}(NO_3)_{15}$ (**Ga_7In_6**) (Figure 1.1). The solid-state structure of this discrete nanoscale cluster has been determined by single crystal X-ray diffraction. Researchers have discovered that these clusters make superb precursors for homogenous, smooth, defect free $InGaO_3$ thin films when using a simple spin coating method from aqueous solution, followed by mild annealing.[3] This type of solution processing has then been used to produce transistors incorporated into a functioning prototype liquid crystal display (LCD).[4] This finding raises the question of how and why do these clusters form and subsequently condense to produce films of far superior quality than the corresponding simple inorganic salts? Similar questions can be asked about nanoparticle behavior in solution. How do reaction conditions drive nanoparticle formation and subsequent ligand passivation of the core?

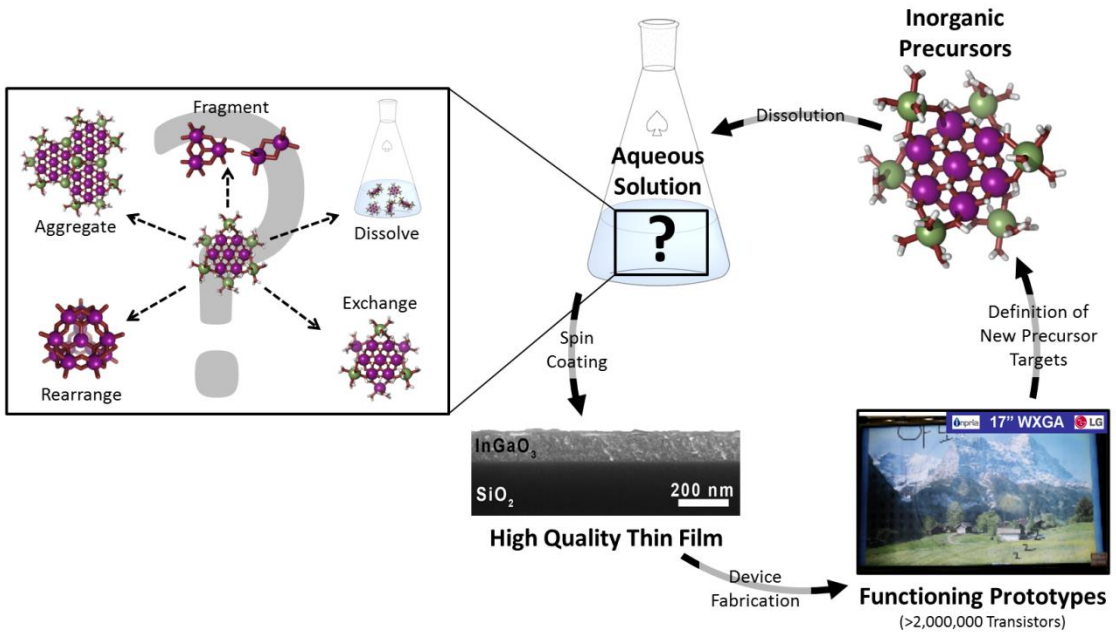

Figure 1.1. Precursors, films, and devices cycle. Determining the fundamental solution behavior of inorganic nanoscale species allows for the design and control of the syntheses of new precursors used in the production of functional materials. In this specific example, understanding the fundamental dynamic behavior of the nanoscale cluster $\mathbf{Ga_7In_6}$ in solution allows for better design of clusters for similar application cycles.

Also, how do functionalized nanoparticles undergo self-assembly into more complicated devices? Before these more challenging questions can be answered, we must first find or develop techniques that are able to detect and define the relevant inorganic nanoscale species in solution.[5]

Some standard methods used to identify stable inorganic nanoscale species rely on significant sample preparation (SEM, TEM, AFM, XPS, and X-ray crystallography). These techniques each require species to be isolated from solution, which necessitates a large change in concentration and, in some cases, exposure to ultra-high vacuum (UHV). This makes it impossible to verify that the results of these experiments describe the properties of the relevant species when in solution. For the analysis of the core dimensions of inorganic nanoscale species in solution, recent literature makes it clear that

SAXS sells.[6–8] While powerful, this technique is not a stand-alone source for the identification and characterization of inorganic molecules and particles in solution. The best source of verification comes from a complement of solution analysis techniques. While NMR spectroscopy has been attractive to many fields, not until recently has interest in NMR resonated with inorganic cluster and nanoparticle researchers. Corroborative techniques such as DOSY NMR or Dynamic Light Scattering (DLS), which measure hydrodynamic radius, seem like ideal mates for SAXS analysis.

Solid-state analytical techniques are information rich, and would be even more powerful assets if related directly to complementary solution based characterization. In order to leverage the information available, the species in solution must first be observed. From there a combination of techniques can answer the more complicated questions of interest to researchers. In this Concept paper we illustrate how new strategies to elucidate the dimensions of inorganic nanoscale species in solution lead to significant advances in the understanding of solution structure and dynamics. These advances will, in turn, lead to better control and refinement of the chemistry and resultant materials properties.

Complementary and Corroborative Solution Techniques

This chapter will first review a variety of techniques commonly available for the analysis of size in solution (UV-Vis, ESI-MS, DOSY, SAXS, and DLS). Techniques that can provide complementary spectral signatures for the inorganic nanoscale species in solution are also discussed (NMR, Zeta-potential, UV-Vis, IR, and Raman). While there are a number of other information-rich techniques, the focus here is on those that are commonly available at a typical research institution. Although each of these techniques has an important function in the analysis of certain compounds, this Chapter focuses on

the characterization of clusters, nanoparticles, and other inorganic species in solution from the perspective of synthetic materials chemists.

Given the limited literature precedence and the restrictions of the techniques used for the characterization of nanoscale inorganic species in solution, researchers must first be able to predict an expected size range for the stable species making this an iterative process. This necessity demonstrates that size actually does matter. In an ideal case, a solid-state technique such as crystallography can be used to guide the search in solution while keeping in mind that the isolated solid-state species may not be the same as the relevant species in solution. There are several dimensions of well-defined nanoscale inorganic species that can be measured and described as size. The concept of size is fundamentally ambiguous as it may be related to the core, shell, or outer solvation sphere of the structure in question (Figure 1.2). While alone each technique is able to provide some indirect measure of size, the complete determination of the size-properties of any given material requires corroboration or the correlation of multiple complementary techniques. Once the size- properties have been determined, the material may be subjected to a multitude of techniques to determine more detailed structural properties. These techniques can be used in concert to elucidate more complex dynamic behavior in solution.

Small Angle X-ray Scattering (SAXS)

SAXS uses the elastic scattering of monochromatic X-ray radiation to determine the size, shape, and volume of nanoscale particles in solution. For inorganic clusters and nanoparticles the technique is best suited to the measurement of the core, where the

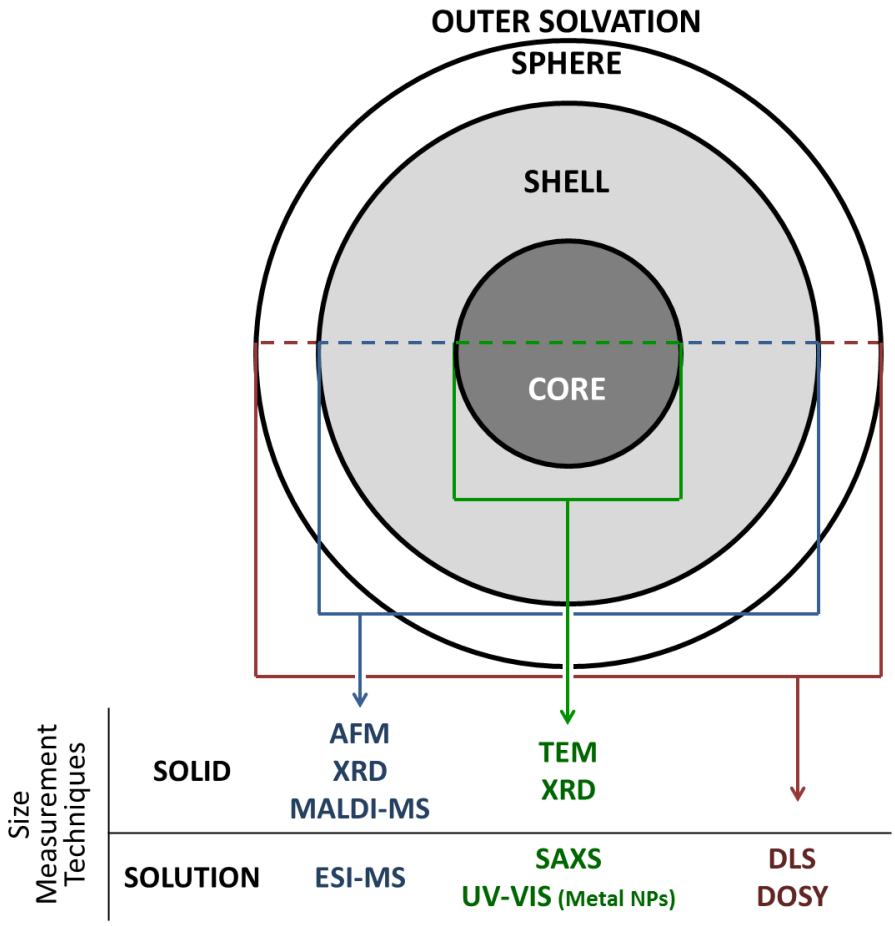

Figure 1.2. Core, shell, and outer solvation sphere dimensions in inorganic nanoscale species. The multiple corroborative techniques capable of measuring the same dimension are grouped in columns by color. Techniques in separate columns complement one another by measuring different regions.

elements are of significantly higher or lower electron density than the solvent. SAXS was developed for the determination of the shapes of large biomolecules using synchrotron radiation sources. Advances in X-ray generator technology and the use of line source collimation now enables this technique at the lab-scale. While scattering data may be analyzed using model-independent approaches, much of the utility of SAXS for the analysis of small (< 5 nm) inorganic clusters is derived from direct modeling. The information that can be obtained from a SAXS experiment depends on the type of sample

being analyzed as well as what is already known about the material.[9] For polydisperse materials, a size distribution can be determined if information about shape is known. If the material is well-defined and monodisperse, information about shape can be extracted along with size. For this reason it is important to couple SAXS analysis with another technique in order to maximize the information gained. The core size can be corroborated with solid-state measurements (XRD or TEM), or complementary techniques can be used to measure the shell or solvation sphere in solution in order to correlate with the core size (Figure 1.2). One obvious advantage of the use of SAXS for core size determination is the ability to characterize the material in solution without the risk of artifacts from sample preparation. SAXS also allows for the variation of sample parameters such as solvent, temperature, or pH. However, in order to produce scattering there must be a contrast in electron density between the material of interest and the solvent used.[10] Additionally, solvents with a very high X-ray absorbance, including many halogenated organic solvents such as chloroform and dichloromethane, are not well suited to analysis by lab scale instruments because the majority of photons will not reach the X-ray detector.

Nuclear Magnetic Resonance (NMR)

NMR spectroscopy can provide information about structure, concentration, dynamics, reaction rate, and chemical environment, among others. Using a magnetic field, NMR aligns the spin of nuclei in a molecule then measures their relaxation. Depending on the atom and its environment, the frequency of relaxation will result in a signal with a specific chemical shift. Structural information can be gained from NMR based on symmetry and environment, but prior chemical shift information is helpful but not readily available for many inorganic species. To assign chemical shifts in molecules

with no literature precedence complicated and time intensive computations are beneficial. When working with ^{1}H nuclei there can be sample-dependent solvent limitations due to exchange between the protons of the molecule in question and the solvent. This is usually not an issue when working with other NMR-active nuclei. Unfortunately, any paramagnetic metal will lead to broadening of NMR signals making it more difficult to gain useful information from the spectrum.[2,11] Two-dimensional NMR techniques have allowed for complex structural problems to be tackled more easily. By applying field gradients, Diffusion Ordered Spectroscopy (DOSY) has allowed for the measurement of the translational diffusion coefficient, caused by Brownian motion, of a molecule relative to the solvent. Once the viscosity of the sample is measured, the Stokes-Einstein equation can be used to approximate the solvation sphere of a spherical species.[12,13] This measurement can be corroborated in solution with DLS measurements and complemented with techniques measuring the core or shell (Figure 1.2).

Electrospray Ionization Mass Spectrometry (ESI-MS)

ESI-MS is capable of determining the molecular weight and fragmentation pattern of many discrete molecular species. Ions are evaporated by producing a fine spray of a very dilute (10^{-5} M) solution of the species of interest allowing the mass to charge ratio of the resulting fragments to be determined. This has recently been used to identify intermediates in order to infer assembly mechanisms in polyoxometallates.[14] ESI-MS is potentially very powerful for the characterization of suitably stable inorganic species especially when corroborative techniques are used (Figure 1.2). There are several drawbacks to using this technique for the investigation of inorganic nanoscale species with more dynamic speciation such as hydroxy-bridged aqueous clusters where pH, ionic

strength and the role of smaller ion intermediates can have a large effect. Due to the low concentrations necessary for this measurement, the species being investigated may not represent the species present at the higher concentrations relevant to materials scientists. In addition, during measurement the samples undergo drastic changes in concentration and pH resulting in shifts to the equilibrium of speciation. This technique can therefore lend itself to over interpretation due to the copious amounts of data that can be gathered from fragmentation patterns. Caution should be taken when applying information on charged particles in the gas phase to solvated inorganic nanoscale species.[15] These issues may be mitigated with complementary core and solvation sphere measurements.

Dynamic Light Scattering (DLS)

DLS allows indirect measurement of the solvation sphere of a species by measuring changes in Rayleigh scattering. DLS uses the time dependent scattering intensity fluctuations to measure the same Brownian motion as DOSY NMR making them ideal corroborative techniques. DLS can determine the size and polydispersity of an inorganic nanoscale material and does not require the use of potentially expensive deuterated solvents. Many of the disadvantages of DLS result from the intensity weighing of the measurement. This means that the technique is biased to larger particles with more scattering. As a result, detection limits are inversely proportional to the size of the object being analyzed, and the largest objects in solution dominate the signal from samples with multiple populations.[16] DLS has a major limitation in studying metal nanoparticles when the wavelength of the laser excites the surface plasmonic resonance (SPR). For instance, gold's SPR absorbance overlaps with the wavelength of the green laser at 532 nm in some DLS instruments, reducing signal to noise. This can easily be resolved by choosing

a different wavelength of laser, but finding a second instrument is not always an easy task and purchasing a second laser is costly. DLS instruments can also be used to measure zeta potential. The zeta potential is a way of characterizing the surface charge of the solvation sphere in a given solvent system.[17] This can then be related to the relative stability of the particles in the solvent of choice.

UV-Visible Spectroscopy (UV-Vis)

UV-Vis provides information about the wavelengths of light that a species absorbs. For inorganic cluster chemistry UV-Vis can provide information about the coordination and the electronic structure of constituent atoms. UV-Vis can also measure absorbance caused by the SPR of electrons in the metal core of a nanoparticle. This absorbance can be used indirectly to calculate the core size of metal nanoparticles and quantum dots, which can be corroborated by SAXS.[18] This also provides a handle for determining concentration, as well as, changes in speciation over time. However, this technique is limited to inorganic nanoscale species that absorb in the wavelengths of light accessible to the spectrometer. This is particularly well suited for the measurement of metal nanoparticles with a SPR in the visible range or clusters composed of transition elements because of well-known excitations involving d-orbitals. This limits the utility of the technique for main group elements containing closed d shells.[11]

Infrared (IR) and Raman

IR and Raman spectroscopy are techniques that can be used to complement the determination of size by providing structural information about a molecule based on rotational and vibrational frequencies. By using them in tandem, scientists are able to characterize both the symmetric and asymmetric vibrational modes of bonds in inorganic

species in the solid and solution phases. Although IR is the less expensive and more common technique, it is essentially impossible to collect usable data in aqueous solutions. This is due to the large dipole moment of water that causes an enormous signal across the entire spectrum. Useful IR data can be collected in an array of other solvents including alcohols and organics. On the other hand the Raman spectra are clearly visible in water, because water is not readily distorted by an external electric field (polarizability). IR and Raman cannot be used to identify inorganic species directly unless there are analogs in the literature. To assign vibrational modes in molecules with no literature precedence, high-level computations are necessary. These complementary techniques are best used to study the solution dynamics, formation, and exchange kinetics of a species that has been identified and characterized in solution. By using these techniques on inorganic nanoscale species one can gain structural information by characterizing the vibrational modes, as well as, study kinetics and dynamics of the inorganic species in solution.[2,11]

Multiple Techniques Provide More Detailed Information

The understanding of the dynamic behavior of inorganic nanoscale species in solution is rapidly evolving, and a gap exists in relating solid-state and solution structures. As a result, the literature tends to report size measurements in an inconsistent manner and rarely provides detail about which dimension is being defined. For inorganic nanoscale species the core can describe different size aspects. For instance, "core" could describe the metal core of a ligand-stabilized nanoparticle or the kinetically stable covalently-bonded metal hydroxide/oxide portion of aqueous clusters or even the coordination network surrounding the hollow core of cage clusters (Figure 1.3). For solvated species the shell comprises either well-defined organic capping ligands or tightly

associated counter ions of an inorganic cluster. The outer solvation sphere of all of these species includes organized solvent and will be related to the solvent of choice. In much of the literature that reports size, these distinctions are often overlooked.

Starting from the outside, the outer solvation sphere can be probed by techniques measuring the diffusion of the stable inorganic nanoscale species in solution such as DOSY and DLS. By varying the solvent system, changes in solvation can be probed. By identifying a weakly interacting solvent this diffusion information can also be used to approximate the outer dimensions of the shell. SAXS data can be modeled to provide core size and volume or thickness of a cage cluster. By subtracting the core size from the shell or outer solvation sphere dimensions, thicknesses and volumes of these regions can be calculated.

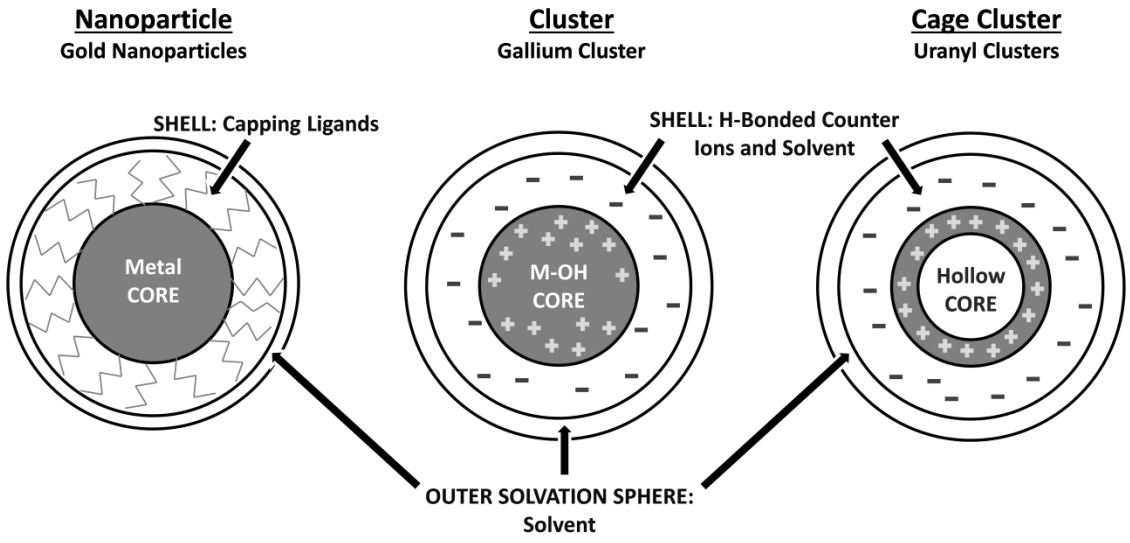

Figure 1.3. Generalization of regions within inorganic nanoscale species. Schematic diagram relating the various layers of inorganic nanoscale species to the generic regions referred to as the core, shell, and outer solvation sphere. Each of these examples is further explored in the case studies presented.

These types of inorganic nanoscale species represent examples of the need to use complementary characterization methods. More information can be gained by combining multiple techniques and using iterative investigations to observe dynamic behaviors in solution. The authors have chosen three examples that exemplify this approach in practice.

Observing Ga_{13}: More Complex than a Disappearing Spoon

Similarly to the Ga_7In_6 example, $Ga_{13}(\mu_3\text{-}OH)_6(\mu\text{-}OH)_{18}(H_2O)_{24}(NO_3)_{15}$ (**Ga_{13}**) can be used as a precursor to make high quality Ga_2O_3 thin films.[3] Until recently, very little was known about the existence or stability of this cluster in solution. Johnson, Hutchison, and co-workers were recently able to observe **Ga_{13}** in solution via ^{1}H-NMR in the non-exchanging solvent d_6-DMSO.[19] With no literature precedence it was impossible to confirm that the ^{1}H signals observed in the spectrum belonged to the bridging hydroxo and capping aquo ligands of the cluster. After acquiring a DOSY spectrum with a corrected diffusion coefficient of $0.955 \times 10^{-10} \pm 0.064 \times 10^{-10}$ m^2s^{-1} in d_6-DMSO, a hydrodynamic radius of 11.2 ± 0.8 Å was assigned to the species in solution (Figure 1.4). This alone was not sufficient evidence to confirm the existence of **Ga_{13}** in solution because the radius is significantly larger than a cluster in the solid-state. However, SAXS data indicated a core radius of 5.5 ± 1.5 Å in solution, which corroborates the size measured in the solid-state via single crystal XRD (r = 5.6 Å). Thus, we were able to confidently report that **Ga_{13}** is stable in DMSO at a concentration of 2 mM.

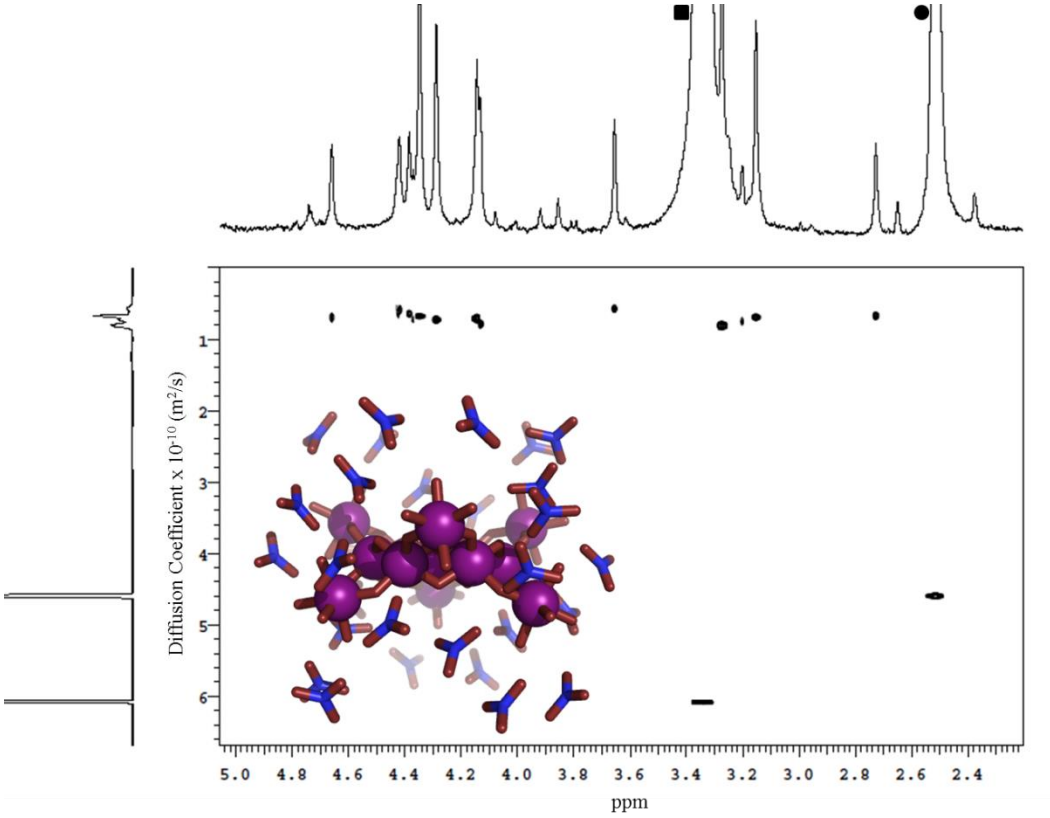

Figure 1.4. ^{1}H-DOSY NMR of Ga_{13}. Representative ^{1}H-DOSY NMR spectrum of a 2 mM sample of **Ga_{13}** cluster in d_6-DMSO ($D_{avg} = 0.955x10^{-10} \pm 0.064x10^{-10}$ m^2/s) (■) H_2O peak and (●) DMSO peak. [20,21]

This confirmation allows for more complex studies to be initiated. Currently we are studying **Ga_{13}** in the solid and solution phase via Raman spectroscopy.[22] This research indicates that the cluster observed in solution has significantly different vibrational characteristics than the solid. These results support previous hypotheses that the clusters are very dynamic in solution. Using comparisons between NMR, Raman, SAXS, and DLS we seek to learn about the growth, stability, degradation, and aggregation of this cluster in solution. We hope to gain information on the mechanism of cluster formation and the pathway by which **Ga_{13}** becomes a thin film

Probing Nanoparticles: Worth More than Their Weight in Gold

Gold nanoparticles (AuNPs) are of continued interested due to their unique size-dependent optoelectronic properties. Characterization of these materials can be challenging as they are often polydisperse which complicates measurement. While high vacuum techniques such as TEM are effective in determining the core size and polydispersity, the low number of particles sampled makes statistically significant population characterization difficult. In addition, there are concerns over the effect that sample preparation may have on the nanomaterials analyzed. Hutchison and co-workers have synthesized and isolated a well-defined particle with the formula $Au_{11}(PPh_3)_8Cl_3$ (**Au_{11}**).[8]

Early investigations into the properties of **Au_{11}** led to the comparison and corroboration of TEM measurements with synchrotron SAXS data (Figure 1.5). The ability to perform these experiments with a lab scale SAXS followed and characterization was further corroborated with single crystal XRD.[8] While these experiments are a powerful way to confirm the stability of these nanoparticles in solution, they are only able to determine the size of the gold core. There have been conflicting reports in the literature about the solvation sphere of monolayer protected AuNPs. Early studies of AuNPs using DOSY NMR demonstrated the interdigitation of the ligand shell with neighboring particles when at high concentrations.[23] Other research groups have proposed that alkane thiol protected AuNPs in organic solvents may diffuse at a rate equivalent to the gold core alone.[24] This raises significant questions about the nature of solvated ligand-protected AuNPs.

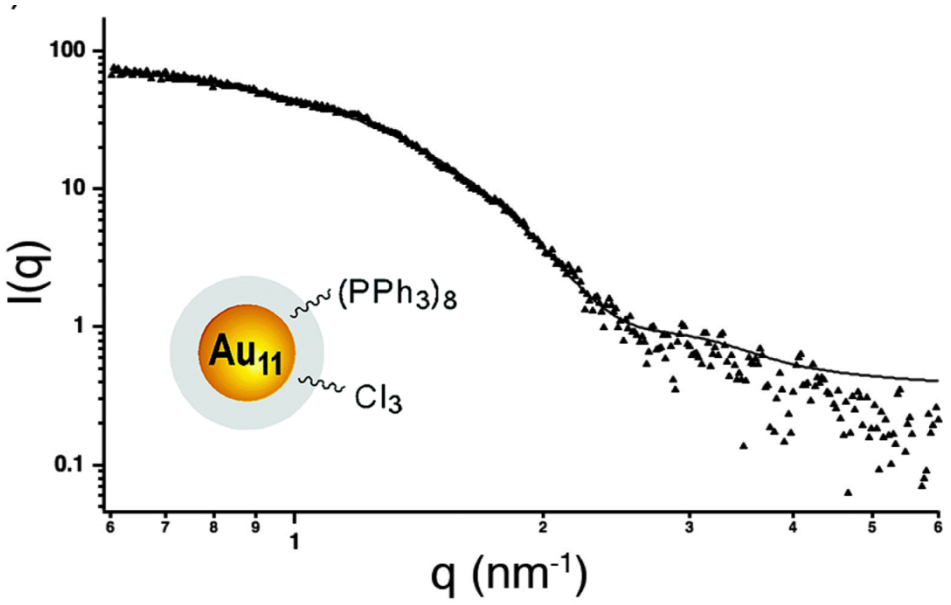

Figure 1.5. SAXS of Au_{11}. Schematic of $Au_{11}(PPh_3)_8Cl_3$ and SAXS scattering pattern from steady state flow measurements performed at the Advanced Light Source.[8]

In order to elucidate the behavior of the ligand shell, current studies aim to measure the effect of solvent interaction with these classes of AuNPs. Monodisperse particles with sharp NMR signals such as **Au_{11}** enable the use of DOSY to determine the hydrodynamic radius, which we will discuss in more detail in a subsequent paper.[25] By varying the solvent and then complementing the measurement of the hydrodynamic radius using DOSY with the determination of the core size by SAXS we aim to uncover information previously unavailable about the nature of the ligand shell.

Depleting the Controversy around Clusters Containing Uranium: A Glowing Review

Widespread interest in the remediation of spent uranium fuel and other waste products has spurred recent research into the controlled growth and speciation of uranyl clusters. Under appropriate conditions the Burns group has shown that uranyl salts form cage compounds including self-assembled core-shell clusters with fullerene topology.[26–29]

Single crystals were isolated of a variety of these cage clusters including compounds with oxalate, pyrophosphate, and peroxide bridging ligands. SAXS data were collected and fit to a core-shell model allowing for the determination of the inner and outer dimensions of the cage cluster confirming the persistence of these species in solution. To follow the growth of these cage clusters in solution, ESI-MS and SAXS were used in tandem to measure the molecular weight and size of the species in solution over time**.** ESI-MS suggests that one of the isolated cluster fragments forms within an hour of mixing. After 15 days the desired fullerene-like core-shell structure begins to form, a full 16 days before crystal formation! At the time of crystallization, ESI-MS showed that the solution still consists of a mixture of species.[26] However, these data alone are not sufficient to fully describe the growth of the clusters for the reasons outlined above. To bolster the ESI-MS findings, SAXS was used to follow the maximum vector length of particles in solution as a function of time. SAXS revealed a nearly linear increase in size from the initial cluster fragment to the final core shell structure (Figure 1.6).

In a recent collaboration between the Burns and Casey labs, the structure and reaction dynamics of the pyrophosphate cage cluster[29] in solution were studied using ^{31}P DOSY to obtain information about the hydrodynamic radius.[30] By using ^{31}P instead of ^{1}H DOSY the issues associated with solvent and proton exchange are eliminated. Studies of this type allow for the characterization of these inorganic nanoscale species in water, the solvent most pertinent to their potential applications in the environment. This demonstrates a potential expansion of this combined technique to a wider variety of materials.

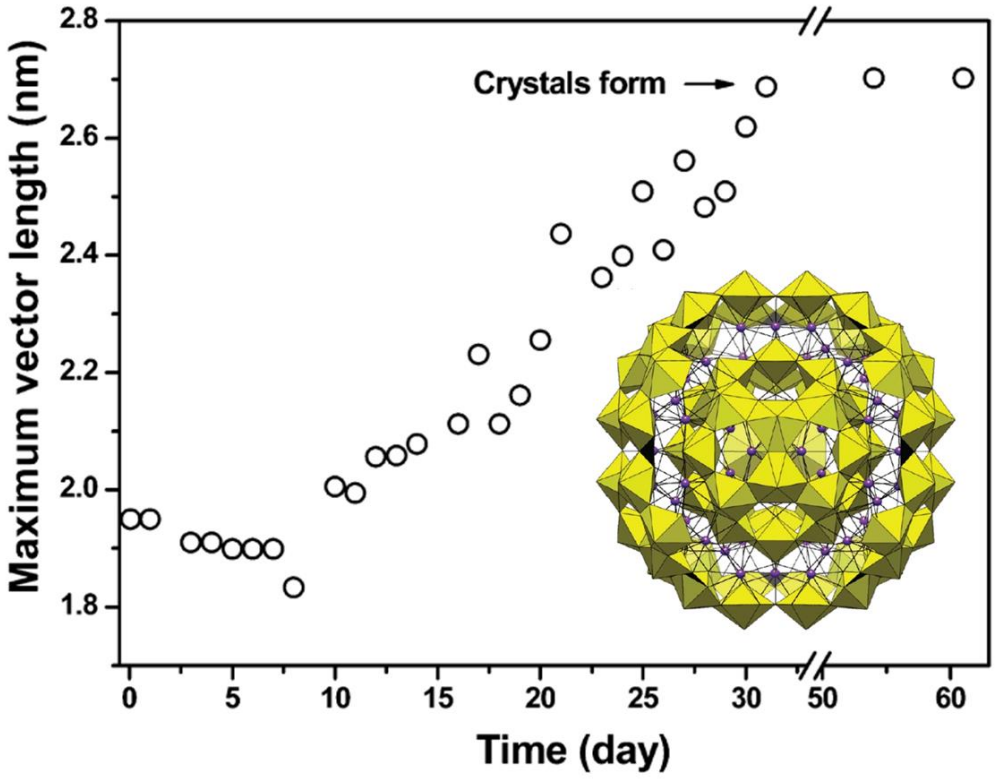

Figure 1.6. Structure of a uranyl cage and cluster growth monitored by SAXS in solution. Adapted with permission from (J. Qiu, J. Ling, A. Sui, J. E. S. Szymanowski, A. Simonetti, P. C. Burns, *J. Am. Chem. Soc.* **2012**, *134*, 1810–1816.).Copyright (2012) American Chemical Society.

Conclusion

While there are a number of techniques available to determine the size of inorganic nanoscale species, the dimensions measured are often misrepresented. By recognizing that these techniques measure different dimensions, a complementary approach can be utilized to map out the core, shell, and outer solvation sphere. Solid-state techniques can be used to characterize the core and shell of a material isolated from solution. To confirm that the relevant species in solution is the same as the solid-state structure, related dimensions of the species must be measured in solution to corroborate the solid-state data. Once this has been verified, additional techniques can provide a

wealth of information. The ability to confirm and observe these inorganic nanoscale species in solution is the essential first step towards the understanding of dynamic behavior. This allows inorganic, materials, and geological chemists to perform more complex investigations to determine the mechanisms of formation, pacification, degradation, polymerization, and aggregation of nanoscale species.

Bridge to Chapter II

By outlining the proper approach to characterize nanoscale species, we can now look into the solution behavior of the $\mathbf{Ga_{13}}$ cluster effectively. Using a combination of two or more techniques listed above is ideal for conformation of stability in solution. In Chapter II, I describe the use of ^{1}H-NMR, DOSY, and SAXS to characterize $\mathbf{Ga_{13}}$ in solution in further detail.

CHAPTER II

SINGLE NANOSCALE CLUSTER SPECIES REVEALED BY ^{1}H-NMR DIFFUSION-ORDERED SPECTROSCOPY AND SMALL ANGLE X-RAY SCATTERING

Contributions

I contributed to this work through the synthesis, ^{1}H-NMR, and DOSY analysis of samples. I also did the majority of the primary writing and editing, as well as, made the figures. Dr. Matthew E. Carnes and Matthew M. Baseman conducted the preliminary ^{1}H-NMR experiment. Dr. Matthew E. Carnes provided experimental insight throughout the scientific process. Dr. Erik K. Richman collected and analyzed the SAXS data and contributed to writing the corresponding section of the manuscript. Prof. James E. Hutchison and Prof. Darren W. Johnson were the principle investigators for this work and provided editorial, experimental design, and data interpretation assistance. This communication was published with frontispiece art included in 2012 in *Angewandte Chemie International Edition* a publication of Wiley-VCH Verlag GmbH & Co. KGaA, volume 51 pages 10992-10996.[19]

Introduction

Considerable attention has been drawn to inorganic nanoscale clusters[31] due to their value and effectiveness as catalysts and catalyst precursors,[32–36] single-molecule magnets,[37,38] sensors,[31] and single source precursors for thin films and other materials;[39] as well as, their important roles in geological, environmental, and life sciences.[40] In

recent work, we have developed new techniques for synthesizing nanoscale clusters and transforming them into high-quality films and other designed nanostructures.[3,41–44] To date we have developed high-yielding, greener techniques to synthesize a variety of M_{13} (Figure 2.1) precursor clusters (Ga, Al, Ga/ In, and Al/In) in gram scale quantities.[3,41,42]

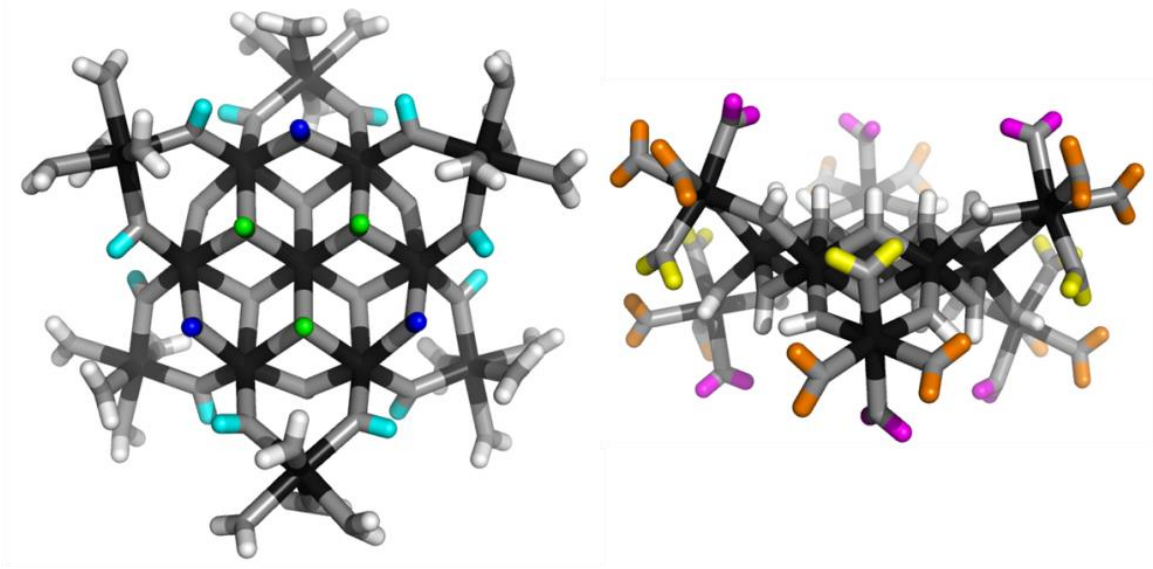

Figure 2.1. Top and side view of M_{13}. Representations of the molecular structure of $[Ga_{13}(\mu_3\text{-}OH)_6(\mu\text{-}OH)_{18}(H_2O)_{24}](NO_3)_{15}$ (**Ga_{13}**) determined by single-crystal X-ray diffraction. Left: Top view of **Ga_{13}** depicting 3 types of hydroxide bridges. The μ_3-OH are green and the μ-OH are blue and cyan. Right: Side view of **Ga_{13}** depicting the 3 types of capping water ligands.

Currently, the main technique for analysis of these and related fully inorganic clusters is single crystal x-ray diffraction. This method provides a detailed understanding of their solid-state structure; however, due to the lack of clear spectroscopic handles, little is known about solution speciation and stability of these discrete inorganic complexes at the millimolar to molar concentrations of interest to synthetic chemists, geochemists, and material scientists. What is the dominant species in a solution of dissolved clusters? Are aggregates present? Methods such as Small Angle X-ray Scattering (SAXS),[29,45,46] Wide Angle X-ray Scattering (WAXS),[45] and Dynamic Light Scattering (DLS)[46] are often used

to probe solution dynamics and speciation via size analysis, but are not widely available. Electrospray Ionization Mass Spectrometry (ESIMS) is a powerful technique for detecting cluster species and monitoring reaction intermediates; however, high-resolution instruments are not routinely available, and the technique evaluates a narrow and dilute concentration range that selects for detection of the most ionizable species at a concentration often below that of relevance to speciation studies for materials applications.[15,47] Herein we present a powerful tandem method to provide conclusive characterization data for such aqueous inorganic nanoscale clusters in polar solvents using SAXS to probe the core inorganic structure and the universal technique of ^{1}H-NMR and Diffusion Ordered SpectroscopY (DOSY) to assess the hydrodynamic radius of the cluster.

Ga_{13} SAXS Results

SAXS was used to test for the presence of distinct **Ga_{13}** clusters (Figure 2.1) in solution at 2 mM concentration in DMSO. After background subtraction and desmearing, the data were analyzed for size distribution using the scattering program IRENA.[48,49] The scattering was consistent with discrete spherical particles of radius 5.5 ± 1.5 Å and showed no signs of significant aggregation (Figure 2.2). Gratifyingly, this result matches the value measured directly from the crystal structure from centroid to centroid of the high-Z gallium atom core (r = 5.6 Å).[41] This result is consistent with the presence of the **Ga_{13}** cluster in DMSO solution and prompted analysis of the cluster by solution phase NMR spectroscopy.

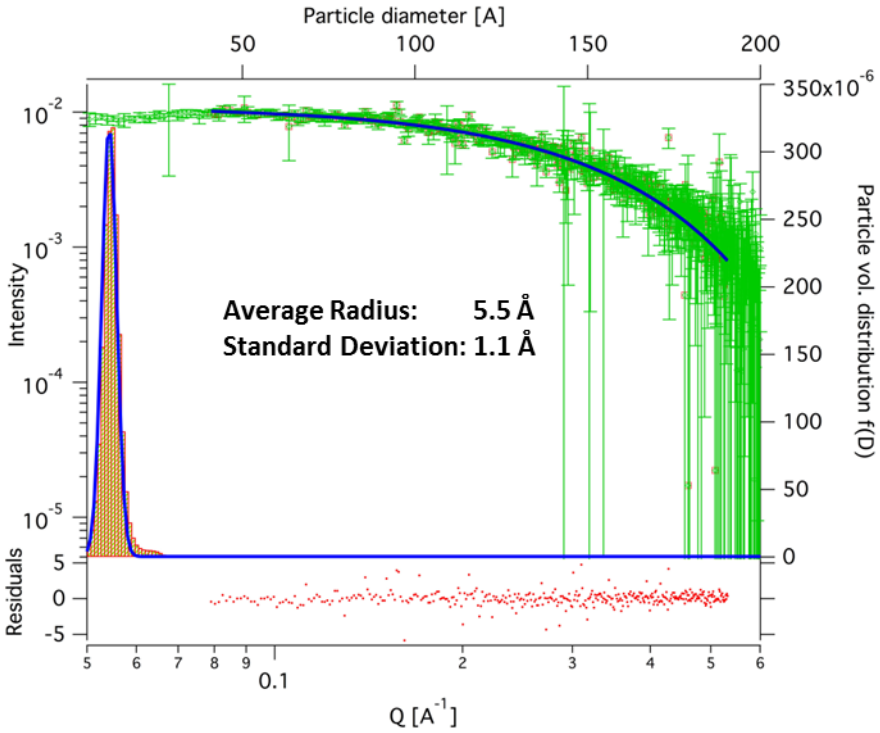

Figure 2.2. SAXS of Ga_{13}. SAXS pattern and fit that confirms the presence of Ga_{13} cluster in solution. Spherical particles of radius 5.5 ± 1.1 Å and no significant aggregation were detected. Particle vol. distribution f(D) is a function of particle diameter.

Ga_{13} ^{1}H-NMR Results

The ^{1}H NMR spectra of **Ga_{13}** in deuterated acetone, water, and methanol are completely silent. Therefore, we were shocked to observe that the acidic protons of the hydroxo and aquo ligands of **Ga_{13}**, shown in Figure 2.1, are clearly visible in wet d_6-DMSO (Figure 2.3A). ^{1}H-NMR has been sparingly used to analyze aqueous inorganic clusters, presumably due to fast exchange of the acidic hydroxo and aquo protons with protic solvents and solubility issues associated with the high charge of the clusters.[50–52] Consequently, DOSY has been used infrequently on such inorganic structures and only in the presence of organic supporting ligands.[53,54] To the best of our knowledge, these two

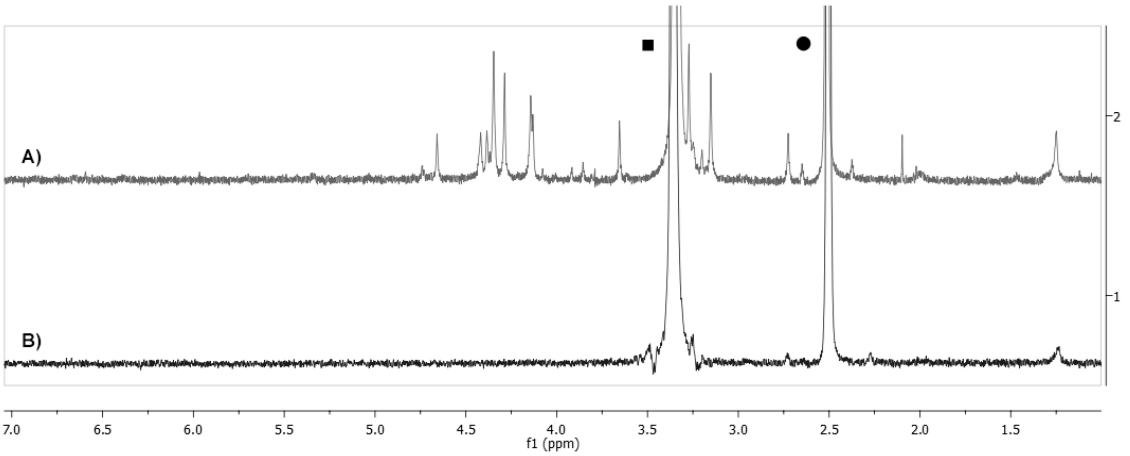

Figure 2.3. ^{1}H-NMR of Ga_{13}. ^{1}H-NMR spectra of gallium complexes in d_6-DMSO: (A) 2 mM **Ga_{13}** solution after 5 days. (B) Control spectrum of a saturated $Ga(NO_3)_3$ solution showing only solvent peaks; presumably the coordinated aquo ligands are in fast exchange with solvent. (■) H_2O peak and (●) DMSO peak.

techniques have not been used in tandem to characterize completely inorganic nanoscale structures of relevance to materials science (inks) and aqueous hydrolysis chemistry. The fact that **Ga_{13}** can be observed by ^{1}H-NMR spectroscopy in solution enables investigation of the cluster by DOSY and provides insight into the hydration sphere of these nanoscale species. DOSY experiments confirmed the presence of cluster-sized species in solution. Figure 1.4, from the previous chapter, displays the DOSY spectra for a 2 mM d_6-DMSO solution of **Ga_{13}**. The small differences between diffusion coefficients produced by the signals of the cluster can be attributed to water exchange,[55] peak overlap, and/or data processing.[12,56] The average diffusion coefficient of all the cluster related peaks based on quadruplicate measurements is $0.955\text{x}10^{-10} \pm 0.064\text{x}10^{-10}$ m^2/s (see representative DOSY spectrum in Figure 1.4).[20,21] By applying the Einstein-Stokes Equation 2.1 a radius of 11.2 ± 0.8 Å was determined. The error in hydrodynamic radius arises from averaging the

$$D = \frac{k_B T}{6 \pi \eta r_H} \qquad \textbf{(Eqn. 2.1)}$$

multiple diffusion constants observed for the cluster that result from the numerous exchanging protons present on the cluster. Regardless, all diffusing species are consistent in size with a single highly solvated, hydrogen bonding nanoscale cluster. (Similar behavior has been observed for sucrose in wet solvents, see below.)[55] The hydrodynamic radius is obviously larger than would be expected for the **Ga_{13}** cluster (r = 8.0 Å based on the crystallographic unit cell parameters and assuming a spherical particle). However, interactions with counter ions, hydrogen bonding to solvent, and solvation spheres dramatically increase the size of the observed species drifting through solution due to Brownian motion.[57] Preliminary DLS data, which also measures hydrodynamic radius, substantiates the presence of a cluster sized species in DMSO under the same conditions. The difference between the radius calculated from the DOSY results and the crystallographic unit cell data can be explained by comparison to the characteristics of sucrose, a small-molecule model containing multiple hydroxyl groups.[55] Sucrose was chosen for three reasons: 1) like the **Ga_{13}** cluster, it is highly solvated in DMSO solution, 2) it possesses numerous hydrogen bond donors and acceptors, and 3) it is the only related molecule we could find in the literature with both XRD and DOSY data available in DMSO solution. Sucrose has a crystallographically measured radius of 4.38 Å, and under the same conditions run for the **Ga_{13}** samples, a DOSY-calculated hydrodynamic radius of 6.1 Å. An even larger increase in hydrodynamic radius (11.2 Å) over crystallographic radius (5.6 Å) is observed in **Ga_{13}**, presumably resulting from the high charge (+15) and correspondingly higher solvation energy and weakly associated counterions, which corroborates the SAXS data showing a single cluster species persists in solution at mM concentrations.

Consequently, it should be noted that immediately after dissolving crystalline **Ga_{13}** in d_6-DMSO, the ^{1}H-NMR spectrum is complicated (Figure 2.4). Depending on the concentration of water in the sample, the spectrum simplifies between a few hours to a few days (H_2O concentrations tested: 0.1 M-2.0 M, see Chapter IV, Figure 4.11 for more detail). Once simplified, the spectrum remains constant for at least 2 months, indicating long-term stability of the observed cluster species in solution (Figure 2.3A). Alternately, if this initial solution is heated to 50°C, the simplified spectrum appears immediately and again persists for months when the sample returns to room temperature (Figure 2.3A). We believe the original complexity of the spectrum is due to the establishment of a slow equilibrium between coordinated aquo and DMSO ligands in the peripheral ligand shell (and corresponding hydrogen bonding to the first solvation sphere). This hypothesis is supported by DOSY evidence (Figure 2.5) confirming that the size of the species in solution remains constant during this exchange process (Figure 2.4). Further details of

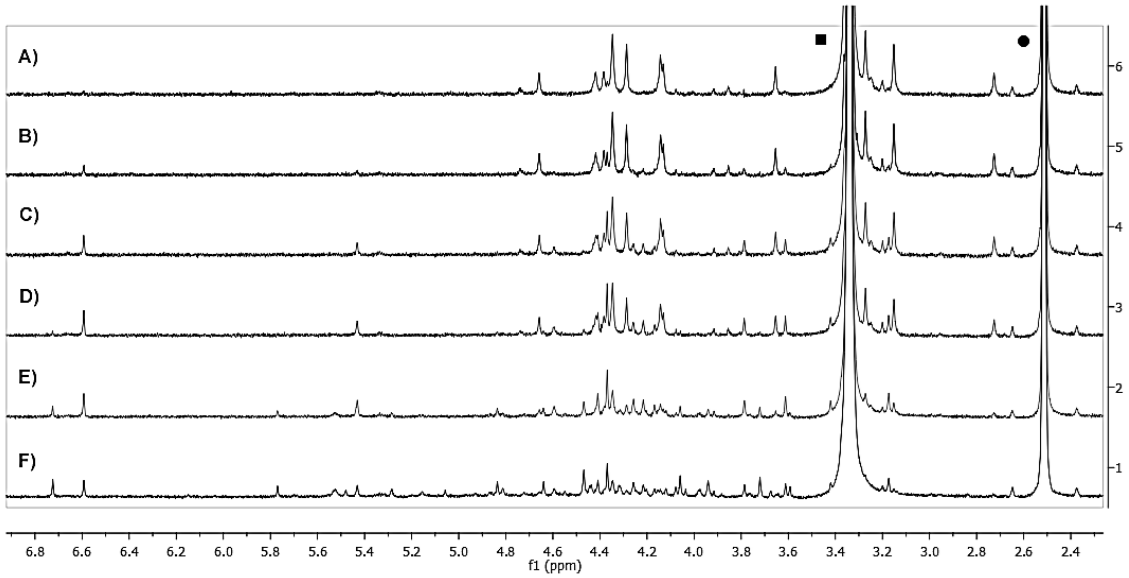

Figure 2.4. ^{1}H-NMR spectra of 2 mM Ga_{13} in d_6-DMSO over time. (A) Δt = 76.0 Hours (B) Δt = 51.5 Hours (C) Δt = 30.5 (D) Δt = 24.0 Hours (E) Δt = 6.5 Hours (F) Δt = 0.5 Hours (■) H_2O peak and (●) DMSO peak.

this equilibrium will be reported in Chapter IV, along with studies related to the kinetics of ligand and metal exchange reactions on these and related clusters.

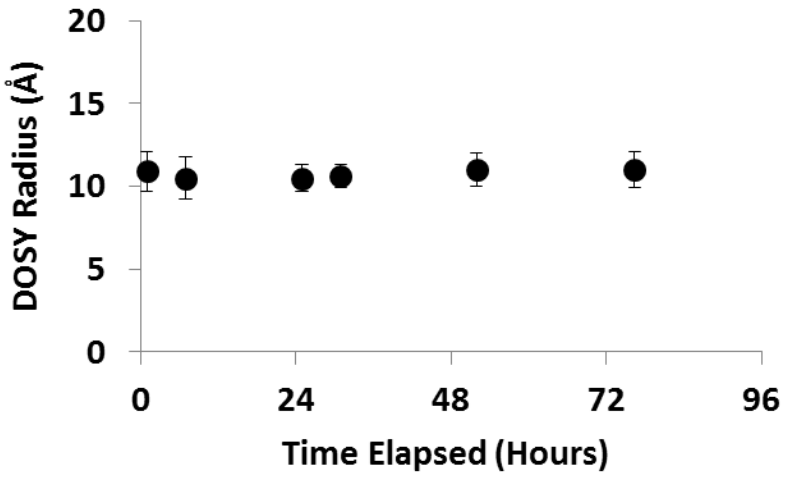

Figure 2.5. DOSY data for 2 mM Ga_{13} in d_6-DMSO over time.

Conclusion

In conclusion, it is possible to detect ^{1}H-NMR spectral signals from the hydroxide bridges and capping water molecules of a completely inorganic nanoscale **Ga_{13}** cluster in wet d_6-DMSO. This enabled the solution phase identification of the single cluster species in the wet polar solvent DMSO by DOSY NMR in tandem with SAXS. These complementary techniques have not been previously used together to examine the solution speciation of aqueous inorganic clusters, yet they provide a powerful and convenient approach for structural investigation of clusters and particles in solution, enabling unique capabilities across a broad spectrum of polyoxometal and nano chemistries. In addition, our findings suggest that ^{1}H-NMR spectroscopy is likely to be a valuable tool for elucidating the solution dynamics and reactivity of clusters, identifying compositional isomers in heterometallic clusters,[3,58] and determining the mechanisms of

cluster formation and degradation. We are currently working to develop a DOSY calibration curve using other structurally-characterized clusters to relate hydrodynamic radius in a predictable manner to solution structure. Given the emergent interest of these clusters in materials science as inks and precursors for electronic devices, developing solution phase techniques to characterize these precursor solutions is vital to enabling new applications.

Bridge to Chapter III

We have now successfully characterized the $\mathbf{Ga_{13}}$ cluster in solution. In Chapter III, we will use this knowledge to characterize all of the $\mathbf{Ga_{13-x}In_x}$ ($0 \leq x \leq 6$) clusters, as well as, assign the specific peaks to protons in the clusters.

CHAPTER III

SOLUTION PHASE STRUCTURAL CHARACTERIZATION OF AN ARRAY OF NANOSCALE AQUEOUS INORGANIC $Ga_{13-x}In_x$ ($0 \leq x \leq 6$) CLUSTERS BY ^{1}H-NMR AND QM COMPUTATIONS

Contributions

Lindsay A. Wills and I primarily conducted the work in this manuscript. I ran the ^{1}H-NMR experiments and did all of the experimental peak assignments. Lindsay A. Wills, a graduate student at Oregon State University, calculated all of the computational peak assignments. Caitlyn R. Hazlett, an undergraduate researcher, synthesized all of the mixed clusters used in these studies. Dr. Matthew E. Carnes provided essential initial insight on the topic. Prof. Paul H.-Y.Cheong and Prof. Darren W. Johnson were the principle investigators for this work and provided editorial assistance.[59] This work was recently submitted to *The Journal of the American Chemical Society* for publication.

Introduction

Proton Nuclear Magnetic Resonance spectroscopy (^{1}H-NMR) is an important tool heavily utilized by chemists and biochemists since its discovery in 1945.[60] Unfortunately, it is often not a viable technique for characterizing purely inorganic clusters due to the fast exchange of protons and/or ligands in aqueous coordination clusters dissolved in wet/polar solvents. The reliable trends and generalizations in ^{1}H-NMR shifts tabulated for numerous carbon-containing molecules do not translate to this purely inorganic world. The focus of this manuscript is to correlate the ^{1}H-NMR spectral shifts of nanoscale

aqueous clusters dissolved in wet solvents to their hydroxo ligands to substantiate cluster characterization and speciation in solution. The ^{1}H-NMR spectrum of $[Ga_{13}(\mu_3\text{-}OH)_6(\mu_2\text{-}OH)_{18}(H_2O)_{24}](NO_3)_{15}$ (**Ga_{13}**) in wet d_6-DMSO is known.[19] Due to the spectral complexity, no peaks were assigned to specific hydroxo and aquo protons in the structure at that time. Further analysis coupled with computations of the complete series of $[Ga_{13-x}In_x(\mu_3\text{-}OH)_6(\mu_2\text{-}OH)_{18}(H_2O)_{24}](NO_3)_{15}$ clusters ($1\leq x\leq 6$: **$Ga_{12}In_1$**, **$Ga_{11}In_2$**, **$Ga_{10}In_3$**, **Ga_9In_4**, **Ga_8In_5**, **Ga_7In_6**) provides trends and clarity, allowing partial ^{1}H signal assignment and complete assignment of all hydroxo bridges in the "mother clusters" (i.e., clusters entirely capped with water molecules that potentially undergo exchange with coordinating solvents, Figure 3.1).

^{1}H-NMR spectroscopy is the first characterization technique used in modern organic, organometallic, and coordination chemistry, yet such data are only sporadically reported for aqueous inorganic clusters. We have found that under the right conditions

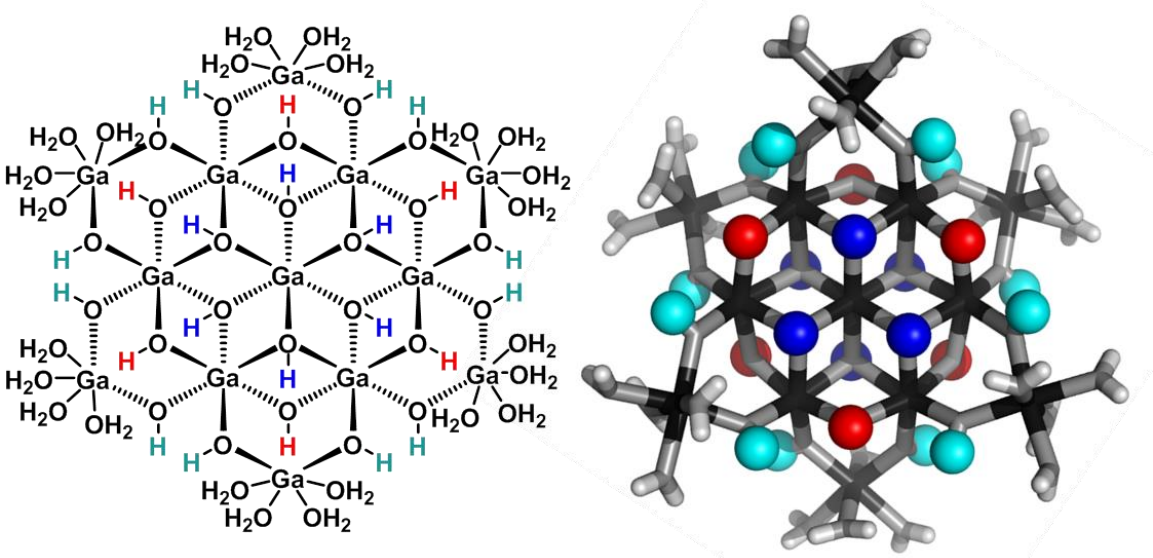

Figure 3.1. Structure of $Ga_{13-x}In_x$ ($0\leq x\leq 6$, pictured x=0) **mother clusters**. Left: Full bonding scheme for clusters including atom identity. Right: Top view of 3 dimensional structure depicting 3 types of hydroxide bridges. The μ_3-OH are blue, internal μ_2-OH are red, and external μ_2-OH are cyan.

such clusters often exhibit rich ^{1}H-NMR spectra that enable characterization by 2D NMR techniques as well.[19] A bottleneck in determining solution structure by NMR spectroscopy has been the lack of tabulated data for such clusters and predictive methods for peak assignment. For instance, there is no known way for predicting where M-H_2O or M-(μ_2-OH)-M ^{1}H-NMR signals should resonate like there is for organic compounds. In this manuscript we provide a literature survey of ^{1}H-NMR spectroscopic resonances reported for known hydroxo- and aquo-coordinated metal complexes. To the best of our knowledge, such data have not been aggregated in one location. We then use this information and complementary quantum mechanical (QM) computations to provide the complete solution structure and peak assignment for a series of clusters.

The $\mathbf{Ga_{13-x}In_x}$ clusters in this work are completely inorganic. Clusters of this type are often more difficult to isolate and challenging to characterize[3] than organic ligand-supported versions, because the ligands lower the cluster charge and can increase stability.[61] However, the lack of organic ligands makes these species attractive candidates as precursors (inks) for metal oxide films, as the lack of organic additives that must be "burned" off during film formation/condensation leads to fewer defects and increases density of thin films. These clusters also serves as excellent inks/precursors due to their high solubility in aqueous and alcoholic solutions, which eliminates toxic solvents often used in thin film production. Minimizing the organic ligands for such applications has produced superior precursors,[3] but the lack of spectroscopic handles has limited the complete understanding of the solution behavior of these species.

Previously, single crystal X-ray diffraction (XRD) and elemental analysis were the techniques used to differentiate the seven known flat-$\mathbf{Ga_{13-x}In_x}$ clusters.[62] These

techniques suggest that multiple cluster species might co-crystallize during isolation (for example, $\mathbf{Ga_{10.2}In_{2.8}}$ has been isolated, which could be an 80/20 mixture of $\mathbf{Ga_{10}In_3}$ and $\mathbf{Ga_{11}In_2}$ or some other such combination). $\mathbf{Ga_{13}}$ has been recently characterized in solution using NMR, Small Angle X-ray Scattering (SAXS), and Raman.[19,22] Although single crystal XRD can provide excellent solid-state data, it cannot answer pressing current questions. Does $\mathbf{Ga_{10}In_3}$ even exist or are all of the mixed clusters simply various ratios of $\mathbf{Ga_{13}}$ and $\mathbf{Ga_7In_6}$? Do all of the possible isomers in the $\mathbf{Ga_9In_4}$-$\mathbf{Ga_{11}In_2}$ clusters (Figure 3.1) co-crystallize or are certain ones thermodynamically or kinetically favored? Is there a way to determine the ratio of isomers present in a sample? Using ^{1}H-NMR, we have established a quick technique for characterizing samples that could address these questions and will accelerate the synthesis and identification of cluster species in solution.

^{1}H-NMR Spectra of Hydroxo/Aquo Bridged Coordination Compounds

Only a limited number of reports of completely inorganic, hydroxo bridged species have been studied via ^{1}H-NMR spectroscopy. However, the moderate chemical shift library of hydroxo protons identified in ligand-supported metal complexes and coordinated water allows for some comparison. The typical chemical shifts of coordinated water ligands are generally downfield (Table 3.1). Typically hexaaquo species have proton signals in the range of 8.3 to 11.3 ppm, while water ligands on metal oligomers tend to appear slightly upfield between 6.3 and 10 ppm.

Little is known about the potential trends for these hydroxide bridges in inorganic species, although it appears that the metal atom and its coordination number are main contributors to the chemical shift of these hydroxo protons. The collected chemical shifts

Table 3.1. ^{1}H-NMR data for water ligands bound to metal atoms.

Metal	Type of Complex	Chem. Shift (ppm)	NMR Conditions	Ref.
Al^{III}	Hexaaquo	10.2	d_6-Acetone; 400 MHz	63
Ga^{III}	Hexaaquo	8.3	d_6-Acetone;-50°C; 500 Hz	64
Rh^{III}	Hexaaquo	9.0—9.2	d_6-Acetone; -83°C; 400 MHz	65
Sn^{IV}	Hexaaquo	10.1—11.3	d_6-Acetone;-100°C; 60 MHz	66
Al^{III}	Oligomer (Al_{13}-Keggin)	7.5	d_6-Acetone; -30°C; 400 MHz	50
Al^{III}	Oligomer (Al_{13}-Keggin)	6.3	d_3-Acetonitrile; 400 MHz	50
Al^{III}	Oligomer (Al_{13}-Keggin)	8.0	H_2O/d_6-Acetone (2.5:1); -20.6 to -5.2°C; 500 MHz	67
Al^{III}	Oligomers	7—10	d_6-Acetone; 400 MHz	63
Al^{III}	Oligomers	8—9.5	-	50,65
Rh^{III}	Oligomers	8.4, 8.7	d_6-Acetone; -83°C; 400 MHz	65

have been tabulated and discussed for the readers benefit. (Tables 3.2-3.5) For diamagnetic complexes, μ_2-OH protons fall between -4.5 and 7 ppm; while μ_3-OH proton signals occur from -1.05 to 6.79 ppm (Figure 3.2). The observation of these ^{1}H-NMR signals at lower chemical shifts than that of the hexaaquo species and the free hydroxide ions is caused by the increased electron density around the proton in the bridge.[65] These are fairly large regions that are not distinguishable from one another, but can be differentiated from water ligands. By looking more closely at specific metals, coordination environments, and groups on the periodic table, refined assignments of chemical shift regions and apparent trends emerge.

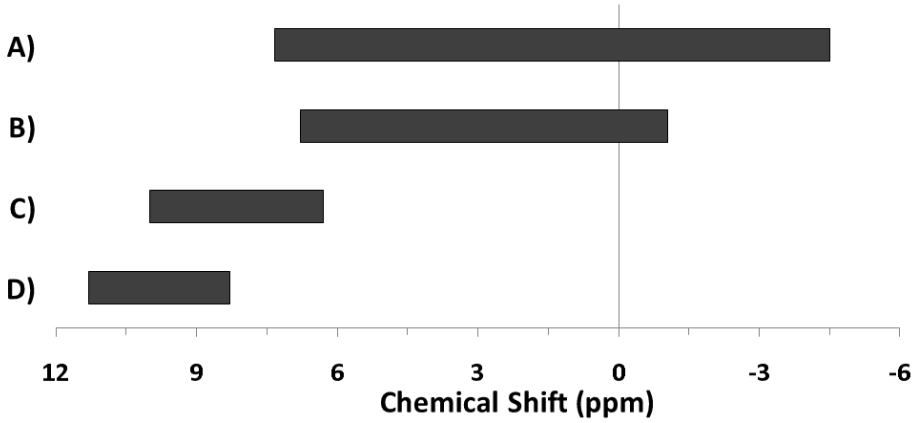

Figure 3.2. General ^{1}H-NMR signal regions for bridging hydroxides and aquo ligands in all metal complexes surveyed. A) μ_2-OH bridges (-4.5—7 ppm); B) μ_3-OH bridges (-1.05—6.79 ppm); C) aquo ligands in multimetallic complexes (6.3—10 ppm); D) hexaquo metal complexes (8.3—11.3 ppm).

Table 3.2. ^{1}H-NMR data for μ_2-OH bridges linking octahedral M(III) in homometallic complexes.

Metal	Molecular Geometry of M^{X+}	μ_2-OH Chem. Shift (ppm)	NMR Conditions	Ref.
Al^{III}	Octahedral (Al_{13}-Keggin)	3.8, 3.9	d_6-Acetone; -30°C; 400 MHz	50
Al^{III}	Octahedral (Al_{13}-Keggin)	2.8, 3.0	d_3-Acetonitrile; 400 MHz	50
Al^{III}	Octahedral (Al_{13}-Keggin)	3.8, 4.5	H_2O/d_6-Acetone (2.5:1); -20.6 to -5.2°C; 500 MHz	67
Al^{III}	Octahedral (Al_{13}-Keggin)	3.8	H_2O/d_6-DMSO (2:1); 3.7 to 95.2°C; 500 MHz	67
Al^{III}	Octahedral	4.8	-	65
Ga^{III}	Octahedral	2.03	d_6-DMSO; 400 MHz	73
Ga^{III}	Octahedral	4.2	d_3-Acetonitrile/D_2O; 250 MHz	74
Ir^{III}	Distorted Octahedral	1.6	*d*-Chloroform; 25°C; 270 MHz	75
Rh^{III}	Octahedral (Di/Trimer)	3.7, 4.3	d_6-Acetone; -83°C; 400 MHz	65
W^{III}	Octahedral	2.05	*d*-Chloroform; 19 and 55°C; 400 MHz	72

Octahedral M(III) ions (M=Al, Ga, Ir, Rh, and W), the most relevant for this work, tend to produce signals for μ_2-OH protons that range from 1.5—5.0 ppm, although this does not hold true for Co(III).[51,68–71] Geometries, chemical shift data, and available NMR conditions for these metal complexes are shown in Table 3.2. The majority of this data was referenced to TMS or residual protic peaks described in the primary papers. Solvent and temperature do not appear to significantly affect the chemical shifts.[72]

The top section of Table 3.3 indicates some metal complexes with different oxidation states and/or non-octahedral geometries exhibit resonance for hydroxide bridges similar to the ranges observed for "trivalent octahedral" metal complexes. In addition to experimental data, computational data is occasionally found for bridging hydroxides. For instance, computed ^{1}H-NMR shifts during the oligomerization of Be(II) species mirrors the experimental measurement of 4.3 ppm.[76,77] Like the trivalent octahedral complexes listed above, certain metals have distinct areas within the bigger region were the ^{1}H-NMR signals of μ_2-OH bridges appear. The data presented in the bottom section of Table 3.3 reveals these ranges. As previously mentioned, octahedral Co(III) complexes differ from the other trivalent octahedral complexes with signals appearing between -4.5 and 0.5 ppm.[51,68–71] Mixed valence Os(0/II) compounds tend to have bridges in the -2.8 to -0.44 ppm range.[92,93] Square planar Pd(II) and Pt(II) complexes have μ_2-OH bridges that range from -3 to 2 ppm.[94–102] Sn has the largest range producing signals anywhere from 1.63 to 7.33 ppm.[82–84,103,105] Yttrium hydroxo bridges tend to have chemical shift values downfield ranging from 5.2 to 6.4 ppm.[104] Zn(II) bridges fall into the -1.15 to 4.16 range.[85,86,89] The proton signal for the only example of a

Table 3.3. ^{1}H NMR data for μ_2-OH bridges in homometallic complexes.

Metal	Molecular Geometry of M^{X+}	μ_2-OH Chem. Shift (ppm)	NMR Conditions	Ref.
Be^{II}	Tetrahedral	4.3	-55°C; 220 MHz	76
Mg^{II}	Trigonal Bipyramidal	3.99	d_8-THF; 25°C; 300 MHz	78
Mo^{II}	Square Pyramidal‡	2.44	-	79
Mo^{II}	Pentagonal Bipyramidal	1.24	d_2-Dichloromethane; -78°C; 400 MHz	80
Ru^{II}	Five coordinate†	3.00, 2.94	d_6-Acetone; 60 & 220 MHz	81
Sn^{IV}	Trigonal Bipyramidal	2.61, 3.85, 2.3	*d*-Chloroform; 360 & 400 MHz	82–84
W^{II}	Pentagonal Bipyramidal	1.7	d_2-Dichloromethane; -78°C; 400 MHz	80
Zn^{II}	Trigonal bipyramidal	4.16	d_3-Acetonitrile; 270 MHz	85
Zn^{II}	Octahedral	2.08	d_6-DMSO	86
Zr^{IV}	Pentagonal Bipyramidal	3.8	d_8-THF; 200MHz	87
Zr^{IV}	Octahedral‡	1.39 – 1.57Ł	d_6-DMSO; 400MHz	88
Cd^{II}	Trigonal Bipyramidal	-2.43	d_3-Acetonitrile; 20°C; 400 MHz	89
Co^{III}	Octahedral	-2	d_6-DMSO	51
Co^{III}	Octahedral	0.63	d_3-Acetonitrile; 250 MHz	68
Co^{III}	Octahedral	-4.18	d_6-DMSO	69
Co^{III}	Octahedral	-0.15, -2.56, -4.95	d_6-DMSO; 20°C; 300 MHz	71
Co^{III}	Octahedral	-1.195, 1.397	d_6-DMSO; 25°C; 600 MHz	70
Co^{III}	Octahedral	-0.702, -0.670	D_2O; 4°C; 600 MHz	70
Ga^{III}	Tetrahedral	0.14	d_6-Benzene; 300 MHz	90
In^{I}	Square Pyramidal	0.93	d_6-Benzene; 400 MHz	91

Table 3.3 Continued. ^{1}H NMR data for μ_2-OH bridges in homometallic complexes.

Metal	Molecular Geometry of M^{X+}	μ_2-OH Chem. Shift (ppm)	NMR Conditions	Ref.
$Os^{0/II}$	Six/Seven coordinate†	-2.8	d_2-Dichloromethane; 400 MHz	92
$Os^{0/II}$	Octahedral	-1.98 – -0.44Ł	*d*-Chloroform; 200 MHz	93
Pd^{II}	Square Planar	-1.58, -1.66, -2.96, -3.09	-	94
Pd^{II}	Square Planar	-2.84, -1.53, -1.67	*d*-Chloroform; 200 MHz	95
Pd^{II}	Square Planar	-1.01, -1.17, -1.25	d_6-Acetone; 200 and 300 MHz	96
Pd^{II}	Square Planar	-0.9, -1.0	*d*-Chloroform; -3 and 27°C; 600 MHz	97
Pd^{II}	Square Planar	-0.85	*d*-Chloroform; 200 MHz	98
Pt^{II}	Square Planar	-0.14	d_2-Dichloromethane; 200 MHz	99
Pt^{II}	Square Planar	-2.04, -1.22, -1.03, -0.56	*d*-Chloroform; 25°C; 80 MHz	100
Pt^{II}	Square Planar	1.9, -0.8, -0.46	*d*-Chloroform; 80 and 200 MHz	101
Pt^{II}	Square Planar	2.0, -0.9, -0.45	d_2-Dichloromethane; 80 and 200 MHz	101
PtI^{I}	Square Planar	2.12	*d*-Chloroform; 300 MHz	102
Sn^{IV}	Octahedral	7.33	d_6-DMSO; 300 MHz	103
Sn^{IV}	Octahedral	7.02	d_2-Dichloromethane; 300 MHz	103
Y^{III}	Eight coordinate†	6.4, 5.45	d_3-Acetonitrile; 300 MHz	104
Y^{III}	Dodecahedral‡	5.4	d_3-Acetonitrile; 300 MHz	104
Y^{III}	Bicapped Trig. Prismatic	5.23, 5.35	d_3-Acetonitrile; 300 MHz	104
Y^{III}	Square Antiprismatic‡	6.2	d_2-Dichloromethane; 300 MHz	104
Zn^{II}	Trigonal Bipyramidal‡	-1.15, -0.66	d_3-Acetonitrile; 20°C; 300 & 400 MHz	89

†No indication of Molecular Geometry. ‡Distorted Geometry. ŁSix or more proton signals in this range.

Cd-(μ_2-OH)-Cd bridge appeared at -2.43 ppm.[89] The typical ranges of these metal hydroxo bridges have been plotted in Figure 3.3 to allow for easy comparison.

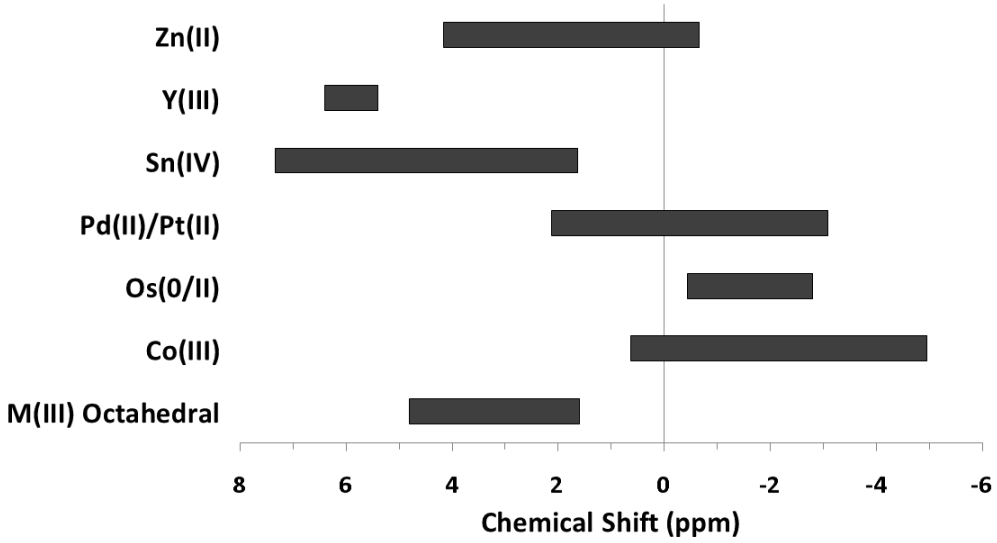

Figure 3.3. General ^{1}H-NMR signal regions for homometallic μ_2-OH bridges in a variety of metal complexes.

Table 3.4. ^{1}H-NMR data for μ_2-OH bridges in heterometallic complexes.

Metals	Molecular Geometry of M^{X+}	μ_2-OH Chem. Shift (ppm)	NMR Conditions	Ref.
Fe^0 / \ Ru^I-(OH)-Ru^I	Octahedral	-2.16, -1.78, -1.75	*d*-Chloroform	106
Fe^{II} / \ Sn^{II}-(OH)-Sn^{II}	Tetrahedral	1.7	d_6-Benzene; 27°C; 300 and 500 MHz	105
Co^{III} / \ Sn^{II}-(OH)-Sn^{II}	Tetrahedral	1.63	d_6-Benzene; 27°C; 300 and 500 MHz	105
Ga^{III}-(OH)-Ca^{II}	Octahedral (Ga)	4.73	*d*-Chloroform; 25°C; 500 MHz	107
Ga^{III}-(OH)-Sr^{II}	Octahedral (Ga)	4.49	*d*-Chloroform; 25°C; 500 MHz	107

Data from the literature for heterometallic complexes was also analyzed because the present work focuses on heterometallic Ga/In clusters as well. Not all of the heterometallic complexes in Table 3.4 feature bridging hydroxides between two different metal atoms, but for completeness they were included.

The hydroxo bridges in trivalent Group 13 octahedral metal complexes are the most relevant for this report. Akitt and colleagues suggests a range of 3 to 6 ppm for Al(III) μ_2-OH bridges.[63] However, the data listed above suggests these resonances should fall within the 2.0 to 4.8 ppm region. The heterometallic octahedral Ga-(μ_2-OH)-M (M ≠ Ga) bridges have very similar chemical shifts to the homometallic hydroxo bridges listed in Table 3.2. This indicates that Ga-(μ_2-OH)-Ga bridges may not easily be distinguished from Ga-(μ_2-OH)-In bridges. Figure 3.4 illustrates the regions where μ_2-OH bridges and capping water ligands on the $\mathbf{Ga_{13-x}In_x}$ clusters most likely will resonate.

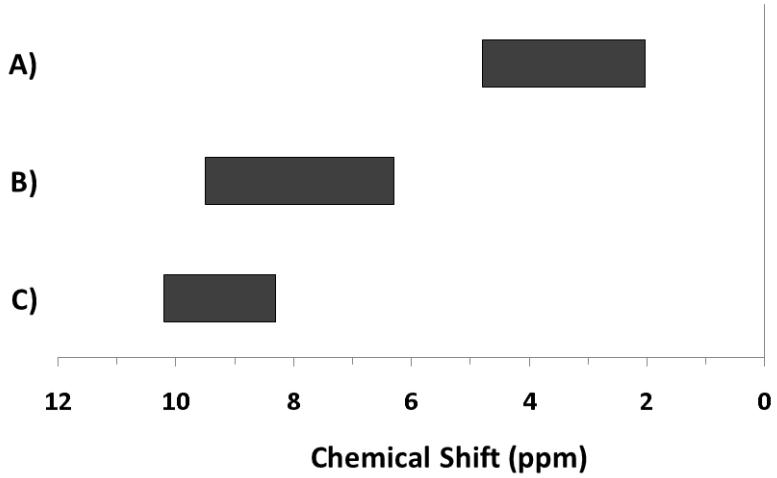

Figure 3.4. General ^{1}H-NMR signal regions for hydroxo bridges and aquo ligands on Group 13 Metals. A) μ_2-OH ligands; B) aquo ligands in multimetallic complexes; C) hexaaquo metal complexes.

One trend that stood out in the general data was that hydroxide bridges shift downfield with increased coordination number of the metal. This trend is visible with

metals such as Sn, Ga, and Zr (Figure 3.5). These were the only metals that had data from several independent sources allowing reasonable conclusions to be made. This trend holds true for all of Group 13, not just gallium (Figure 3.6). Tetrahedral gallium has a Ga-(μ_2-OH)-Ga bridge at 0.14 ppm,[90] Square Pyramidal gallium and indium have peaks in the 1 to 1.5 ppm range,[91,108] and as stated above octahedral aluminum and gallium produce signals between 2 and 5 ppm.

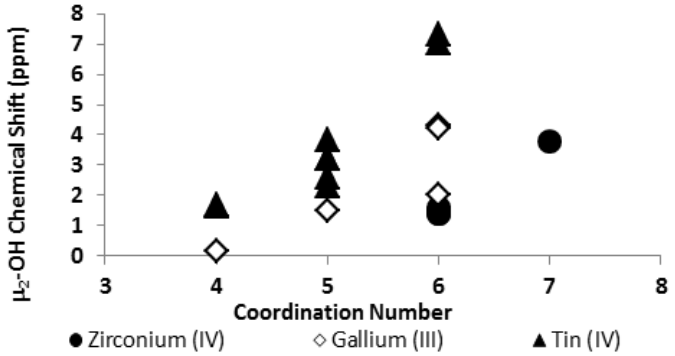

Figure 3.5. As the coordination number of a cation increases, the ^{1}H-NMR signals shift downfield (Tables 3.2 and 3.3).

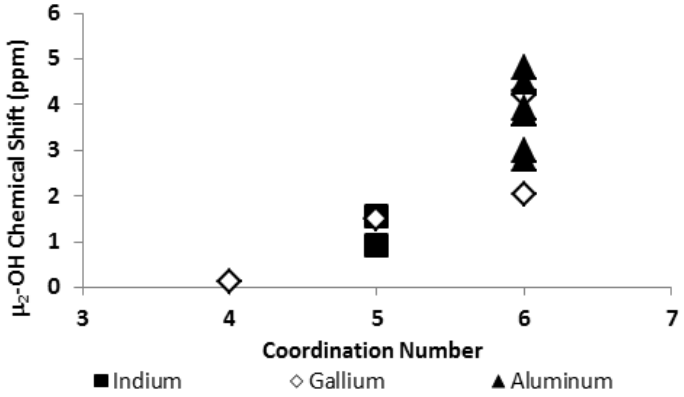

Figure 3.6. As the coordination number in Group 13 increases, the ^{1}H-NMR signals shift downfield (Tables 3.2 and 3.3).

^{1}H-NMR data reported for μ_3-OH protons are even scarcer. As previously stated, these signals appear from -1.05 to 6.79 ppm. The proton chemical shifts in these complexes are listed in Table 3.5. No examples of Group 13 metals with μ_3-OH ligands

were found. The most relevant is the Y(III) complex with a proton signal at 6.05 ppm.[113] Related hydroxide ligands in Th(IV) and Zn(II) compounds also resonate in this region.[111,114] Unfortunately, there are not enough examples of μ_3-OH protons to suggest any trends or regions for specific metals or coordination geometries.

Table 3.5. ^{1}H-NMR data for μ_3-OH bridges linking homometallic atoms.

Metal	Molecular Geometry of M^{X+}	μ_3-OH Chem. Shift (ppm)	NMR Conditions	Ref.
Ca^{II}	Octahedral	1.32, 2.77, 4.57	d_6-Benzene; 25°C; 300 MHz	78
Rh^{I}	Six coordinate†	-1.05	d_4-Methanol; 300 MHz	109
Rh^{I}	Six coordinate†	-0.61, -0.48, -0.02	d_2-Dichloromethane; 300 MHz	109
Sn^{IV}	Trigonal Bipyramidal	3.219, 3.221	*d*-Chloroform; 500 MHz	110
Th^{IV}	Square Pyramidal‡	5.97, 6.16, 6.79	d_6-DMSO; 500 MHz	111
Y^{III}	Dodecahedral£	2.93, 3.1	d_3-Acetonitrile; 300 MHz	112
Y^{III}	Dodecahedral	6.05	d_3-Acetonitrile	113
Zn^{II}	Trig. Bipyramidal/Octahedral	5.4	*d*-Chloroform; 25°C; 300 MHz	114

†No indication of Molecular Geometry. ‡Distorted Geometry. £Associated CuI_3^{2-}.

This brief literature survey will not only help the structural study and assignments presented herein, but we hope this serves as a useful resource for others seeking to assign aquo and bridging hydroxo ligands in inorganic clusters and related compounds. This survey highlights some of the challenges in interpreting even the most basic NMR signals. For example, when two distinct μ_2-OH signals arise in the same ^{1}H-NMR spectrum, it can be difficult to tell them apart. Two examples of this from above are the Al-(μ_2-OH)-Al bridges of Elders and colleagues' Keggin cluster,[50] and the hexanuclear yttrium species by Hubert-Pfalzgraf and coworkers.[112]

These data can also help with identifying possibly misassigned signals. For instance, in $[Al(\mu_2\text{-}OH)(hbo)_2]_2$ (hbo: 2-(2'-hydroxphenyl)-2-benzoxazole)) a peak at 11.47 ppm observed in $CDCl_3$ is proposed to be the bridging hydroxo ligands.[115] Is it possible that this is really a small amount of an aquo-Al(III) complex or some other aquo ligand-containing species? The data reported herein and our literature survey suggest that resonances this far downfield are typically due to aquo ligands; however, there are very few examples of NMR data reported for such species in $CDCl_3$, so much remains to be learned. Similarly, are the peaks assigned to aquo ligands in the spectra of Al(III) and Ga(III) porphyrins containing Ga-(μ_2-OH)-Ga and In-(μ_2-OH)-In bridges at 1.5 and 1.56 ppm, respectively, actually the hydroxide bridges?[108] Hopefully, these tabulated data can be helpful for the future assignment of μ_2-OH and μ_3-OH bridges in related compounds and help begin to develop a reliable database of such peak assignments.

Experimental Section

Chemicals were purchased from Sigma-Aldrich, TCI America, and STREM, and were used as received without further purification. The $\mathbf{Ga_{13-x}In_x}$ clusters were synthesized using previously published methods.[3,43,58,62] ^{1}H-NMR experiments were conducted at 25°C in 5 mm tubes on a 500 MHz Varian spectrometer. Data were collected using Varian Software, referenced to TMS, and processed using MestReNova. The DOSY experiments were performed using the gradient stimulated echo with spin-lock and convection compensation (DgsteSL_cc) pulse sequences. All Varian software standard default settings were kept for DOSY unless otherwise stated. The diffusion delay was increased to 200 ms, the number of increments was increased to 20, and the highest gradient value was set to 25,000. The alternate gradient sign on odd scans and

lock gating during gradient portions were also selected. All Varian software standard default settings were kept for NOESY unless otherwise stated. The NOESY experiment was performed after setting the 90° pulse-width to 13.0 ms, dscale increment to 700 ms, and the t1 increment to 256. To acquire quality resolution, 16 scans were performed.

Quantum mechanical computations were used to predict the chemical shifts of each hydroxo proton in the clusters. The geometries of all of the clusters were obtained from the crystal structures, including the counterions. The NMR chemical shifts were computed using gauge-independent atomic orbital (GIAO) method in B3LYP/def2-SVP level of theory in the gas-phase (Gaussian03). Since the position of the counterions was not perfectly symmetric, we computed the chemical shifts for multiple counterion positions for each cluster structure, in order to eliminate the effects of static, individual counterion positions on the proton shifts. For example, for $\mathbf{Ga_8In_5}$, with one external gallium, we computed the chemical shifts of 6 geometries of this cluster, one for each position the gallium could occupy relative to the counterion positions. Each computed shifts of each type of proton were averaged across clusters of the same geometry discounting counterions, and the shifts were scaled using constant factors for each type.[22] This method was chosen because exclusion of the counterions yielded incorrect ordering of the external and internal μ_2-OH protons, regardless of geometry.

Results and Discussion

The mixed $\mathbf{Ga_{13-x}In_x}$ clusters each yield a unique ^{1}H-NMR spectrum after one day in d_6-DMSO solution (Figure 3.7). The clusters were crystallographically resolved prior to ^{1}H-NMR analysis to determine the stoichiometric ratio of the metal atoms. Diffusion Ordered Spectroscopy (DOSY) was used to verify the presence and integrity of clusters

in solution (Figures 1.4 and 3.8). The calculated hydrodynamic radius of each heterometallic cluster matches that of **Ga_{13}** (Figure 3.9), which was previously characterized using complementary techniques.[1,19] The combination of consistent hydrodynamic radii and the absence of any other proton signals (other than solvent) suggest that the spectra of the clusters consist of bridging hydroxide and/or capping water ligand signals. The distinct combinations of resonances observed in each spectrum confirm that the heterometallic clusters exist as distinct species.

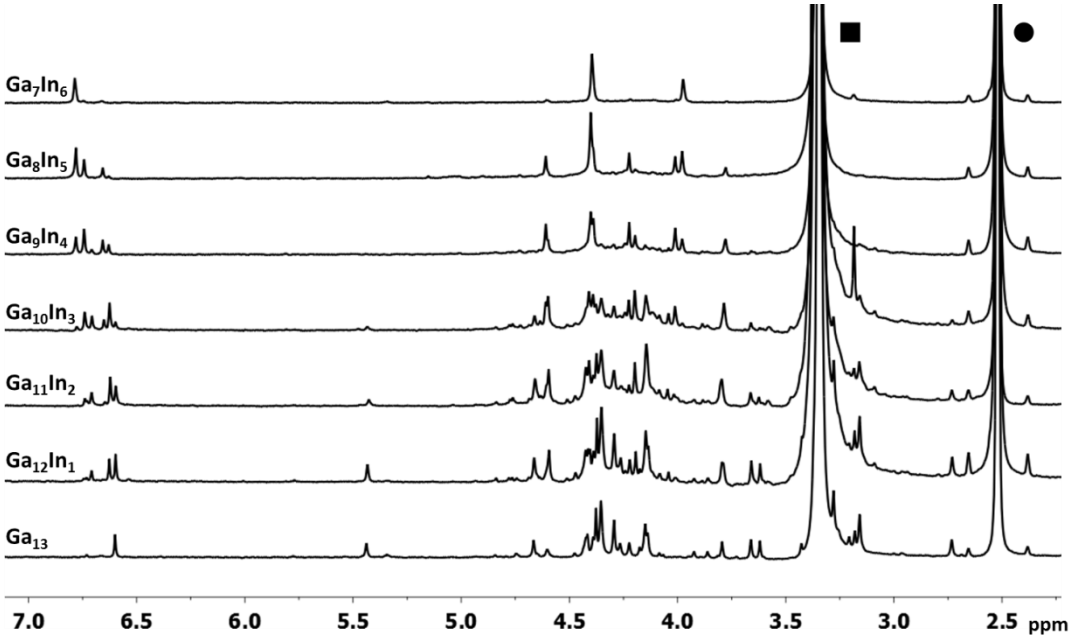

Figure 3.7. ^{1}H-NMR spectra of 2 mM clusters in d_6-DMSO one day after dissolution. H_2O peak (■) and DMSO peak (●).

Understanding the symmetry of these **$Ga_{13-x}In_x$** clusters is essential for analyzing and assigning the proton shifts from NMR. The symmetry of each cluster dictates the number of expected signals that the cluster will have from the hydroxyl protons and aquo ligands. For example, the **Ga_7In_6** and **Ga_{13}** clusters have identical symmetry, and therefore should only ideally yield three total signals from hydroxyl protons. Table 3.6 lists the symmetry of all **$Ga_{13-x}In_x$** clusters studied herein.

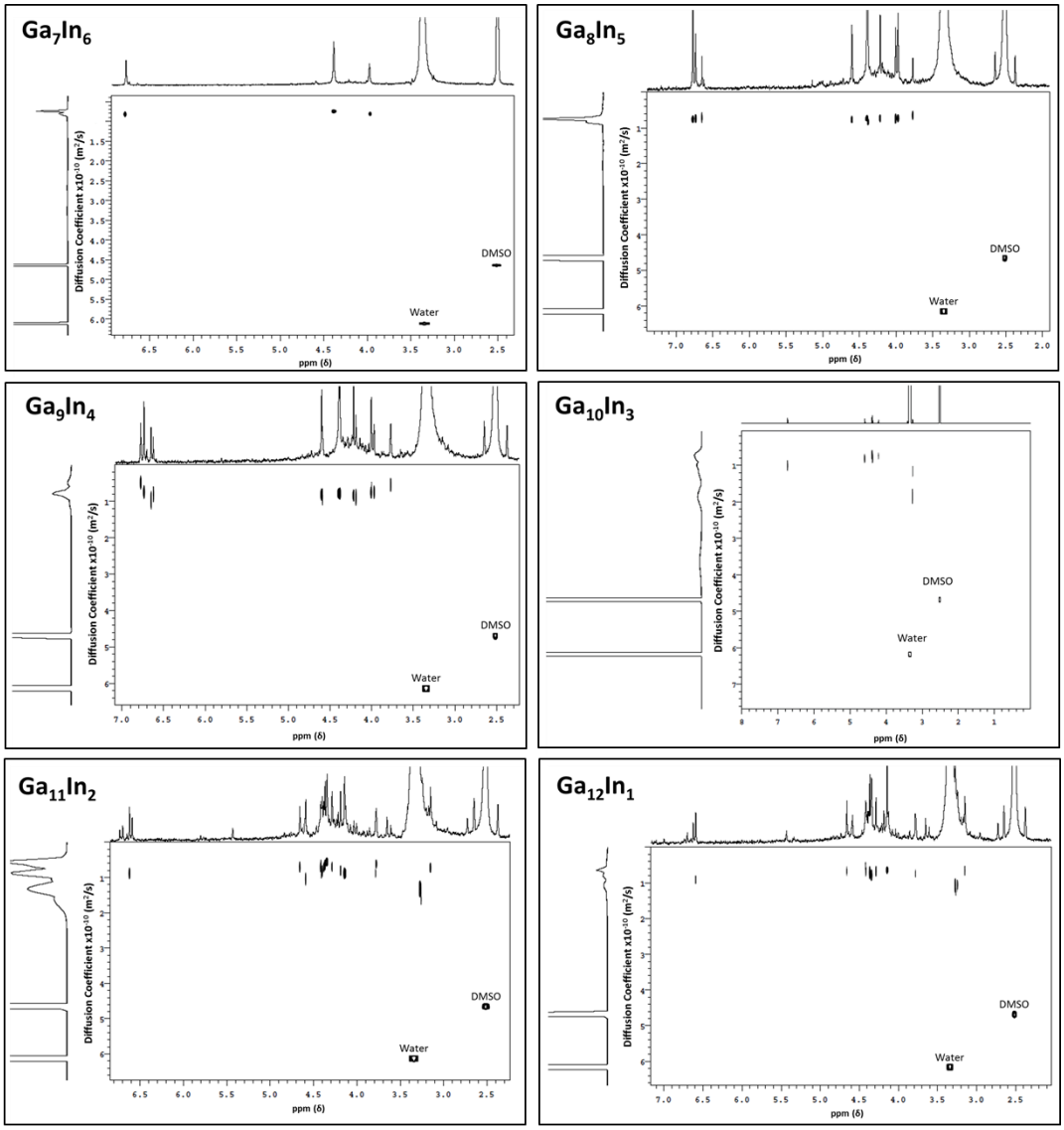

Figure 3.8. DOSY spectra for $Ga_{13-x}In_x$ ($1 \leq x \leq 6$) clusters.

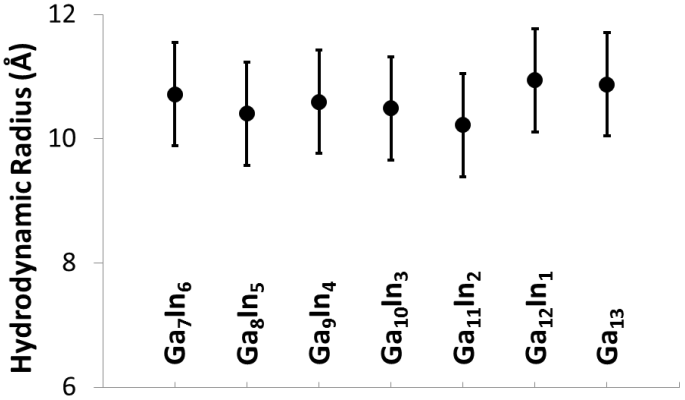

Figure 3.9. Hydrodynamic radii and standard deviation of the clusters measured via DOSY.

Table 3.6. The symmetry and expected proton signal ratios for each type of hydroxide for all studied $Ga_{13-x}In_x$ clusters. Green: Gallium. Purple: Indium.

Cluster	# of Isomers	Structure	Point Group	Expected Signals		
				6 μ_3-OH	6 μ_2-OHint	12 μ_2-OHext
Ga_7In_6	1	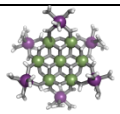	D_{3d}	6 $H^{\mu_3}_{\mathbf{InInIn}}$ (A)	6 $H^{\mu_{2int}}_{\mathbf{InInIn}}$ (G)	12 $H^{\mu_{2ext}}_{\mathbf{InIn}}$ (M)
Ga_8In_5	1	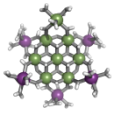	C_{2v}	3 $H^{\mu_3}_{\mathbf{InInIn}}$ (A) 2 $H^{\mu_3}_{\mathbf{InInGa}}$ (B) 1 $H^{\mu_3}_{\mathbf{InGaIn}}$ (D)	3 $H^{\mu_{2int}}_{\mathbf{InInIn}}$ (G) 2 $H^{\mu_{2int}}_{\mathbf{InInGa}}$ (H) 1 $H^{\mu_{2int}}_{\mathbf{InGaIn}}$ (J)	8 $H^{\mu_{2ext}}_{\mathbf{InIn}}$ (M) 2 $H^{\mu_{2ext}}_{\mathbf{InGa}}$ (N) 2 $H^{\mu_{2ext}}_{\mathbf{GaIn}}$ (O)
Ga_9In_4	3	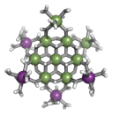	C_{2v}	2 $H^{\mu_3}_{\mathbf{InInIn}}$ (A) 2 $H^{\mu_3}_{\mathbf{InInGa}}$ (B) 2 $H^{\mu_3}_{\mathbf{GaGaIn}}$ (E)	2 $H^{\mu_{2int}}_{\mathbf{InInIn}}$ (G) 2 $H^{\mu_{2int}}_{\mathbf{InInGa}}$ (H) 2 $H^{\mu_{2int}}_{\mathbf{GaGaIn}}$ (K)	6 $H^{\mu_{2ext}}_{\mathbf{InIn}}$ (M) 2 $H^{\mu_{2ext}}_{\mathbf{InGa}}$ (N) 2 $H^{\mu_{2ext}}_{\mathbf{GaIn}}$ (O) 2 $H^{\mu_{2ext}}_{\mathbf{GaGa}}$ (P)
Ga_9In_4	3	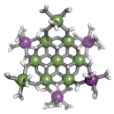	C_{2v}	1 $H^{\mu_3}_{\mathbf{InInIn}}$ (A) 2 $H^{\mu_3}_{\mathbf{InInGa}}$ (B) 1 $H^{\mu_3}_{\mathbf{GaInGa}}$ (C) 2 $H^{\mu_3}_{\mathbf{InGaIn}}$ (D)	1 $H^{\mu_{2int}}_{\mathbf{InInIn}}$ (G) 2 $H^{\mu_{2int}}_{\mathbf{InInGa}}$ (H) 1 $H^{\mu_{2int}}_{\mathbf{GaInGa}}$ (I) 2 $H^{\mu_{2int}}_{\mathbf{InGaIn}}$ (J)	4 $H^{\mu_{2ext}}_{\mathbf{InIn}}$ (M) 4 $H^{\mu_{2ext}}_{\mathbf{InGa}}$ (N) 4 $H^{\mu_{2ext}}_{\mathbf{GaIn}}$ (O)
		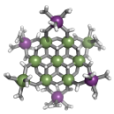	C_{2v}	4 $H^{\mu_3}_{\mathbf{InInGa}}$ (B) 2 $H^{\mu_3}_{\mathbf{InGaIn}}$ (D)	4 $H^{\mu_{2int}}_{\mathbf{InInGa}}$ (H) 2 $H^{\mu_{2int}}_{\mathbf{InGaIn}}$ (J)	4 $H^{\mu_{2ext}}_{\mathbf{InIn}}$ (M) 4 $H^{\mu_{2ext}}_{\mathbf{InGa}}$ (N) 4 $H^{\mu_{2ext}}_{\mathbf{GaIn}}$ (O)
$Ga_{10}In_3$	3	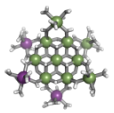	C_{2v}	1 $H^{\mu_3}_{\mathbf{InInIn}}$ (A) 2 $H^{\mu_3}_{\mathbf{InInGa}}$ (B) 2 $H^{\mu_3}_{\mathbf{GaGaIn}}$ (E) 1 $H^{\mu_3}_{\mathbf{GaGaGa}}$ (F)	1 $H^{\mu_{2int}}_{\mathbf{InInIn}}$ (G) 2 $H^{\mu_{2int}}_{\mathbf{InInGa}}$ (H) 2 $H^{\mu_{2int}}_{\mathbf{GaGaIn}}$ (K) 1 $H^{\mu_{2int}}_{\mathbf{GaGaGa}}$(L)	4 $H^{\mu_{2ext}}_{\mathbf{InIn}}$ (M) 2 $H^{\mu_{2ext}}_{\mathbf{InGa}}$ (N) 2 $H^{\mu_{2ext}}_{\mathbf{GaIn}}$ (O) 4 $H^{\mu_{2ext}}_{\mathbf{GaGa}}$ (P)
		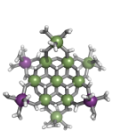	C_1	2 $H^{\mu_3}_{\mathbf{InInGa}}$ (B) 1 $H^{\mu_3}_{\mathbf{GaInGa}}$ (C) 1 $H^{\mu_3}_{\mathbf{InGaIn}}$ (D) 2 $H^{\mu_3}_{\mathbf{GaGaIn}}$ (E)	2 $H^{\mu_{2int}}_{\mathbf{InInGa}}$ (H) 1 $H^{\mu_{2int}}_{\mathbf{GaInGa}}$ (I) 1 $H^{\mu_{2int}}_{\mathbf{InGaIn}}$ (J) 2 $H^{\mu_{2int}}_{\mathbf{GaGaIn}}$ (K)	2 $H^{\mu_{2ext}}_{\mathbf{InIn}}$ (M) 4 $H^{\mu_{2ext}}_{\mathbf{InGa}}$ (N) 4 $H^{\mu_{2ext}}_{\mathbf{GaIn}}$ (O) 2 $H^{\mu_{2ext}}_{\mathbf{GaGa}}$ (P)
		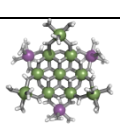	C_{3v}	3 $H^{\mu_3}_{\mathbf{GaInGa}}$ (C) 3 $H^{\mu_3}_{\mathbf{InGaIn}}$ (D)	3 $H^{\mu_{2int}}_{\mathbf{GaInGa}}$ (I) 3 $H^{\mu_{2int}}_{\mathbf{InGaIn}}$ (J)	6 $H^{\mu_{2ext}}_{\mathbf{InGa}}$ (N) 6 $H^{\mu_{2ext}}_{\mathbf{GaIn}}$ (O)
$Ga_{11}In_2$	3	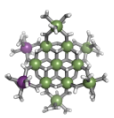	C_{2v}	2 $H^{\mu_3}_{\mathbf{InInGa}}$ (B) 2 $H^{\mu_3}_{\mathbf{GaGaIn}}$ (E) 2 $H^{\mu_3}_{\mathbf{GaGaGa}}$ (F)	2 $H^{\mu_{2int}}_{\mathbf{InInGa}}$ (H) 2 $H^{\mu_{2int}}_{\mathbf{GaGaIn}}$ (K) 2 $H^{\mu_{2int}}_{\mathbf{GaGaGa}}$(L)	2 $H^{\mu_{2ext}}_{\mathbf{InIn}}$ (M) 2 $H^{\mu_{2ext}}_{\mathbf{InGa}}$ (N) 2 $H^{\mu_{2ext}}_{\mathbf{GaIn}}$ (O) 6 $H^{\mu_{2ext}}_{\mathbf{GaGa}}$ (P)
		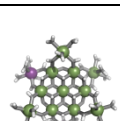	C_{2v}	2 $H^{\mu_3}_{\mathbf{GaInGa}}$ (C) 1 $H^{\mu_3}_{\mathbf{InGaIn}}$ (D) 2 $H^{\mu_3}_{\mathbf{GaGaIn}}$ (E) 1 $H^{\mu_3}_{\mathbf{GaGaGa}}$ (F)	2 $H^{\mu_{2int}}_{\mathbf{GaInGa}}$ (I) 1 $H^{\mu_{2int}}_{\mathbf{InGaIn}}$ (J) 2 $H^{\mu_{2int}}_{\mathbf{GaGaIn}}$ (K) 1 $H^{\mu_{2int}}_{\mathbf{GaGaGa}}$(L)	4 $H^{\mu_{2ext}}_{\mathbf{InGa}}$ (N) 4 $H^{\mu_{2ext}}_{\mathbf{GaIn}}$ (O) 4 $H^{\mu_{2ext}}_{\mathbf{GaGa}}$ (P)

Table 3.6 Continued. The symmetry and expected proton signal ratios for each type of hydroxide for all studied $Ga_{13-x}In_x$ clusters. Green: Gallium. Purple: Indium.

Cluster	# of Isomers	Structure	Point Group	Expected Signals		
				6 μ_3-OH	6 μ_2-OHint	12 μ_2-OHext
$Ga_{11}In_2$	3	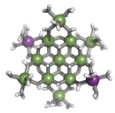	C_{2v}	2 $H^{\mu_3}_{\mathbf{GaInGa}}$ (C) 4 $H^{\mu_3}_{\mathbf{GaGaIn}}$ (E)	2 $H^{\mu_{2int}}_{\mathbf{GaInGa}}$ (I) 4 $H^{\mu_{2int}}_{\mathbf{GaGaIn}}$ (K)	4 $H^{\mu_{2ext}}_{\mathbf{InGa}}$ (N) 4 $H^{\mu_{2ext}}_{\mathbf{GaIn}}$ (O) 4 $H^{\mu_{2ext}}_{\mathbf{GaGa}}$ (P)
$Ga_{12}In_1$	1	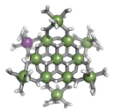	C_{2v}	1 $H^{\mu_3}_{\mathbf{GaInGa}}$ (C) 2 $H^{\mu_3}_{\mathbf{GaGaIn}}$ (E) 3 $H^{\mu_3}_{\mathbf{GaGaGa}}$ (F)	1 $H^{\mu_{2int}}_{\mathbf{GaInGa}}$ (I) 2 $H^{\mu_{2int}}_{\mathbf{GaGaIn}}$ (K) 3 $H^{\mu_{2int}}_{\mathbf{GaGaGa}}$(L)	2 $H^{\mu_{2ext}}_{\mathbf{InGa}}$ (N) 2 $H^{\mu_{2ext}}_{\mathbf{GaIn}}$ (O) 8 $H^{\mu_{2ext}}_{\mathbf{GaGa}}$ (P)
Ga_{13}	1	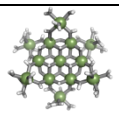	D_{3d}	6 $H^{\mu_3}_{\mathbf{GaGaGa}}$ (F)	6 $H^{\mu_{2int}}_{\mathbf{GaGaGa}}$(L)	12 $H^{\mu_{2ext}}_{\mathbf{GaGa}}$ (P)

Water ligands coordinated to multimetallic Group 13 complexes are known to produce signals from 7—10 ppm.[63] The $\mathbf{Ga_{13-x}In_x}$ clusters contain signals between 2.5—7 ppm, which falls into the range expected for μ_2-OH and μ_3-OH bridges. The spectrum of $\mathbf{Ga_7In_6}$ is much simpler than that of the $\mathbf{Ga_{13}}$ cluster.[19] We suspect this is due to the fact that the 1st order rate constant of water exchange for In(III) is 100x faster than for Ga(III) ($4x10^4$ s^{-1} and $4x10^2$ s^{-1}, respectively).[116] The lack of peaks in the 7—10 ppm region indicates that the exchange rate of the outer water ligands is too fast to observe on the NMR time scale.[19] The rapid aquo ligand exchange of the In(III) ions allows us to observe only the protons associated with the central 7-atom Ga(III) core of $\mathbf{Ga_7In_6}$ leading to 3 signals (μ_3-OH, μ_2-OH_{ext}, and μ_2-OH_{int}) are observable. This aquo ligand exchange process happens much slower with gallium; therefore, the symmetry within the core of $\mathbf{Ga_{13}}$ is not retained and results in a complex spectrum containing more proton signals.

Ga_7In_6 Peak Assignments: Establishing a Basis for Comparison

Ga_7In_6 is a great test case to understand the more complicated clusters where gallium occupies one or more of the peripheral metal sites. The simplicity of the experimental data and the high symmetry of this cluster makes this cluster ideal for the purpose of assigning regions of the spectrum to particular types of protons, which in turn may be used to assign shifts for the other clusters. This assignment was in turn used to determine an appropriate computational method for predicting the proton shifts of the remaining clusters. The computations resulted in subtle differences in the positions of the signals from different types of hydroxo bridges in the clusters, in particular, the μ_2-OH region, which shows strong overlap of the two types of signals (Figure 3.7). The μ_3-OH proton signals are observed between 6.5–7.0 ppm. The remaining μ_2-OH_{int} and μ_2-OH_{ext} proton signals are found between 3.5–5.0 ppm.

Ga_7In_6 ^{1}H-NMR spectra reveal 3 signals, which can be assigned to the three types of bridging hydroxides (Figure 3.10). These three signals integrate to a 1:2:1 ratio, matching the number of protons on specific hydroxide bridges within the 7-atom cluster core (μ_3-OH:μ_2-OH_{ext}:μ_2-OH_{int} ratio = 6:12:6) (Figure 3.1, Table 3.6). This suggests that the peak at 4.4 ppm corresponds to the μ_2-OH_{ext}, which bridge between the 7-atom gallium core and the exterior indiums ions. Other examples of mixed metal Ga-(μ_2-OH)-M bridges corroborate this assignment (Ga-(μ_2-OH)-Ca and Ga-(μ_2-OH)-Sr; 4.73 ppm and 4.49 ppm respectively).[107] As stated above, the signal furthest downfield (~6.8 ppm) corresponds to the protons of the μ_3-OH, similar to the chemical shift of the μ_3-OH bridge in the octahedral Y^{3+} complex.[113] The final peak at 4.0 ppm represents the μ_2-

OHint protons. This assignment is in agreement with M-(μ_2-OH)-M bridges reported for other Group 13 complexes.[50,65,67,73,74]

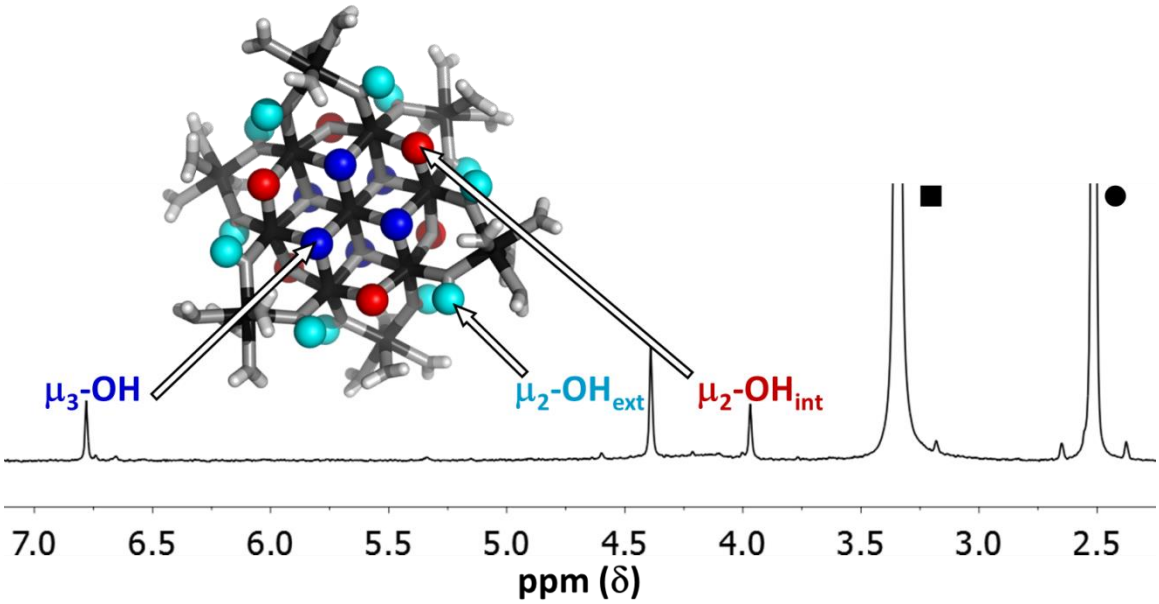

Figure 3.10. ^{1}H-NMR spectra of 2 mM Ga_7In_6 cluster in d_6-DMSO one day after dissolution: The visible signals correspond to the 3 types of bridging hydroxides. H_2O peak (■) and DMSO peak (●).

Due to the simplicity of **Ga_7In_6**, the spectra and analysis for this cluster make a good basis for determining a suitable theoretical method for computational elucidation of the μ_2-OH signals. Most importantly, computations performed without explicit counterions in the structure predict the exact opposite ordering of the internal and external μ_2-OH signals. This was so, regardless of the theoretical methods (HF, B3LYP), basis sets (6-31G*/LANL2DZ, def2-SVP, def2-TZVP, def2-QZVP, etc.), or solvation methods (gas, PCM, and CPCM) employed. From our observations, improvements in levels of theory are unlikely to address the discrepancy. However, when counterions are included, correct ordering is obtained, namely that the μ_2-OH_{ext} signals are downfield from the μ_2-OH_{int} protons (Figure 3.10). These results indicate that the presence, location, and identity of the counterions is immensely important for determining even the

qualitative assignments of ^{1}H-NMR chemical shifts of aqueous metal clusters. The ordering or the μ_2-OH_{int} and μ_2-OH_{ext} protons is more difficult to see for the remainder of the clusters due to significant overlap of μ_2-OH signals, and computations were diagnostic in discriminating these convoluted overlapping signals in all the clusters.

Hydroxo Ligand Naming Convention

As gallium is substituted for indium in the exterior positions of the cluster, a greater number of proton types emerge (Table 3.6). There are 16 unique types of protons in the clusters based on idealized symmetry: 6 μ_3-OH, 6 μ_2-OH_{int}, and 4 types of μ_2-OH_{ext} (Table 3.6). The environments of these protons were determined by the identity of the nearest external metal ion and its two nearest neighbors (i.e., Ga or In). For example, proton $H^{\mu_3}_{\mathbf{In}InIn}$ is a μ_3-OH proton in a section of the cluster with an exterior indium ion directly outside (always indicated in bold) possessing two additional exterior indium atoms on either side (Figure 3.11). Proton $H^{\mu_{2int}}_{\mathbf{In}InIn}$ corresponds to the symmetry-equivalent μ_2-OH_{int} proton bridging the same metals as proton $H^{\mu_3}_{\mathbf{In}InIn}$ (Figure 3.11) The

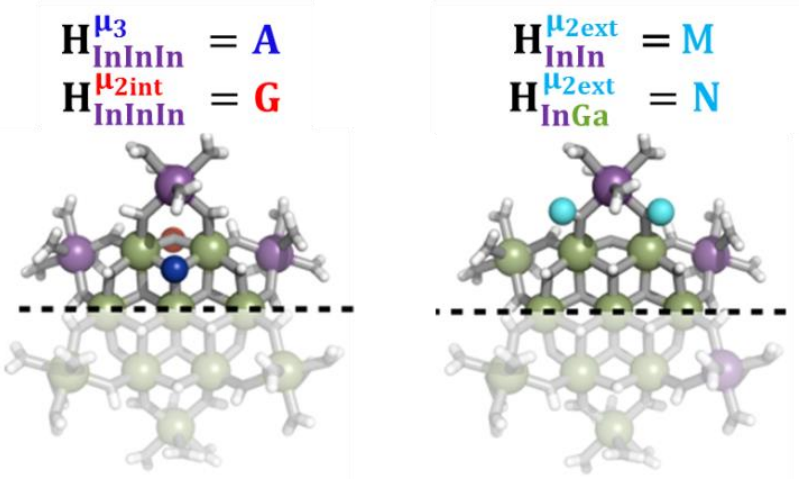

Figure 3.11. Sample naming system for protons in the $Ga_{13-x}In_x$ clusters. Green: Gallium. Purple: Indium.

μ_2-OH_{ext} protons are described in a similar manner. Proton $H^{\mu_2 ext}_{\mathbf{In}In}$ corresponds to the μ_2-OH_{ext} proton connected to an indium ion (indicated in bold) and positioned facing towards a second indium. This naming system is comprehensively represented by Table 3.6.

μ_3-OH Peak Assignments

The peak in the 6.55-6.85 ppm region of the **Ga_7In_6** spectrum corresponds to the μ_3-OH protons. This region contains the simplest set of signals in all the mixed clusters. We suspect that this is because the μ_3-OH protons are the farthest away from, and therefore, the least affected by the bound DMSO. Each peak in this region for the 7 NMR spectra is corresponds to one of the 6 types of μ_3-OH protons (Table 3.7). Proximity to the indium ion causes downfield shifting in the proton signal. This is best shown in **Ga_7In_6**, which has one type of proton ($H^{\mu_3}_{In\mathbf{In}In}$), and exhibits the farthest

Table 3.7. Unique μ_3-OH proton environments of each cluster and the corresponding ^{1}H-NMR fingerprint region. (*assuming 1:1:1 isomeric ratio)

Corresponding μ_3-OH NMR Spectra (ppm)	Cluster	Expected Proton Ratios (Observed Proton Ratios)						
		$H^{\mu_3}_{In\mathbf{In}In}$	$H^{\mu_3}_{In\mathbf{In}Ga}$	$H^{\mu_3}_{Ga\mathbf{In}Ga}$	$H^{\mu_3}_{In\mathbf{Ga}In}$	$H^{\mu_3}_{Ga\mathbf{Ga}In}$	$H^{\mu_3}_{Ga\mathbf{Ga}Ga}$	# of Isomers
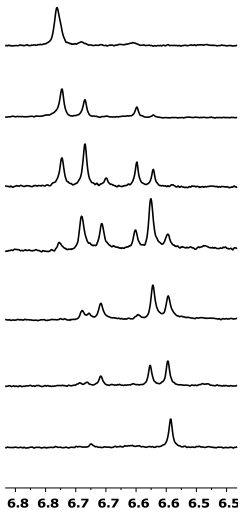	Ga_7In_6	6 (6)	-	-	-	-	-	1
	Ga_8In_5	3 (3)	2 (2)	-	1 (1)	-	-	1
	Ga_9In_4	3 (4)	8 (6)	1 (1)	4 (3)	2 (2)	-	3*
	$Ga_{10}In_3$	1 (1)	4 (6)	4 (3)	4 (3)	4 (6)	1 (1)	3*
	$Ga_{11}In_2$	-	2 (2)	4 (3)	1 (1)	8 (6)	3 (4)	3*
	$Ga_{12}In_1$	-	-	1 (1)	-	2 (2)	3 (3)	1
	Ga_{13}	-	-	-	-	-	6 (6)	1

downfield signal. **Ga_{13}** also has only one type of μ_3-OH proton ($H^{\mu_3}_{\mathrm{Ga}\mathbf{Ga}\mathrm{Ga}}$); however, the lack of indium atoms in the structure leads to the farthest upfield μ_3-OH signal. **Ga_8In_5** and **$Ga_{12}In_1$** each possess one isomer and 3 unique μ_3-OH proton types ($H^{\mu_3}_{\mathrm{In}\mathbf{In}\mathrm{In}}$, $H^{\mu_3}_{\mathrm{In}\mathbf{In}\mathrm{Ga}}$, $H^{\mu_3}_{\mathrm{In}\mathbf{Ga}\mathrm{In}}$ and $H^{\mu_3}_{\mathrm{Ga}\mathbf{Ga}\mathrm{Ga}}$, $H^{\mu_3}_{\mathrm{Ga}\mathbf{Ga}\mathrm{In}}$, $H^{\mu_3}_{\mathrm{Ga}\mathbf{In}\mathrm{Ga}}$, respectively) in 3:2:1 ratios. This is mirrored in the NMR spectra facilitating the assignment of each proton type to a peak (Table 3.7). **Ga_9In_4**, **$Ga_{10}In_3$**, and **$Ga_{11}In_2$** are slightly more complicated because each has 3 possible isomers (Table 3.6), but each predicted μ_3-OH peak is observed. The $H^{\mu_3}_{\mathrm{In}\mathbf{In}\mathrm{In}}$ type protons are shifted farthest downfield, while the $H^{\mu_3}_{\mathrm{Ga}\mathbf{Ga}\mathrm{Ga}}$ type protons are shifted the farthest upfield, for an overall ranking from highest to lowest ppm of $H^{\mu_3}_{\mathrm{In}\mathbf{In}\mathrm{In}}$> $H^{\mu_3}_{\mathrm{In}\mathbf{In}\mathrm{Ga}}$> $H^{\mu_3}_{\mathrm{Ga}\mathbf{In}\mathrm{Ga}}$> $H^{\mu_3}_{\mathrm{In}\mathbf{Ga}\mathrm{In}}$ > $H^{\mu_3}_{\mathrm{Ga}\mathbf{Ga}\mathrm{In}}$ > $H^{\mu_3}_{\mathrm{Ga}\mathbf{Ga}\mathrm{Ga}}$(Table 3.7). Computations support that these signals are produced by μ_3-OH protons and that the $H^{\mu_3}_{\mathrm{In}\mathbf{In}\mathrm{In}}$, $H^{\mu_3}_{\mathrm{In}\mathbf{In}\mathrm{Ga}}$, and $H^{\mu_3}_{\mathrm{Ga}\mathbf{In}\mathrm{Ga}}$ protons should be more deshielded than the $H^{\mu_3}_{\mathrm{In}\mathbf{Ga}\mathrm{In}}$, $H^{\mu_3}_{\mathrm{Ga}\mathbf{Ga}\mathrm{In}}$, and $H^{\mu_3}_{\mathrm{Ga}\mathbf{Ga}\mathrm{Ga}}$ protons. The calculations cannot corroborate or contradict the relative rankings within those two sets (Table 3.7).

In the case of clusters with multiple isomers, the peak integrations of the μ_3-OH protons in the NMRs can provide information about the ratio of each isomer present in the sample. The statistical probability of each isomer, along with the calculated % present in solution, is shown in Table 3.8. Due to a small impurity in the **$Ga_{11}In_2$**, the spectra could not accurately be integrated; therefore, the experimental percentages were not calculated. Similarities in the structures of **Ga_9In_4** and **$Ga_{11}In_2$** allow for comparisons. The NMR data remarkably show a strong correlation to the statistical ratio of isomeric heterometallic clusters. This data indicates that no specific substitution pattern of indium in the outer shell of the clusters is kinetically favorable.

Table 3.8. The isomers of Ga_9In_4, $Ga_{10}In_3$, and $Ga_{11}In_2$ with relative μ_2-OH peak intensities predicted using the integration of μ_3-OH protons, ratio of isomers in solution based on probability, and experimental percentage of isomers present in solution calculated using the μ_3-OH proton integrations. Green: Gallium. Purple: Indium.

Protons	$H^{\mu_{2int}}_{\mathbf{In}In\mathbf{In}In}$ (G)	$H^{\mu_{2int}}_{In\mathbf{In}Ga}$ (H)	$H^{\mu_{2int}}_{Ga\mathbf{In}Ga}$ (I)	$H^{\mu_{2int}}_{In\mathbf{Ga}In}$ (J)	$H^{\mu_{2int}}_{Ga\mathbf{Ga}In}$ (K)	$H^{\mu_{2int}}_{Ga\mathbf{Ga}Ga}$ (I)	$H^{\mu_{2ext}}_{\mathbf{In}In}$ (M)	$H^{\mu_{2ext}}_{\mathbf{In}Ga}$ (N)	$H^{\mu_{2ext}}_{\mathbf{Ga}In}$ (O)	$H^{\mu_{2ext}}_{\mathbf{Ga}Ga}$ (P)
Int.	4	6	1	3	2	-	12	8	8	2
Ga_9In_4 Isomers	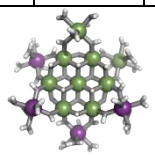			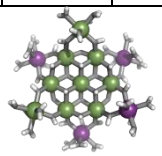			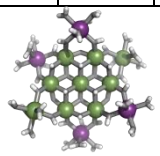			
Exp.	40%			40%			20%			
Prob.	40%			40%			20%			
Int.	1	6	3	3	6	1	8	13	13	8
$Ga_{10}In_3$ Isomers	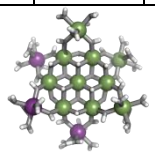			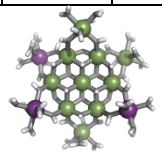			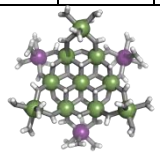			
Exp.	40%			50%			10%			
Prob.	30%			60%			10%			
Int.	-	2	3	1	6	4	2	8	8	12
$Ga_{11}In_2$ Isomers	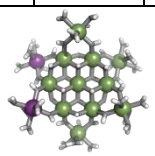			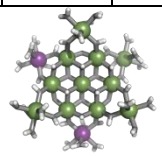			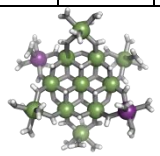			
Exp.	-			-			-			
Prob.	40%			40%			20%			

μ_2-OH Peak Assignments

The μ_2-OH regions of the NMR spectra are not as easily deconvoluted. Based on the **Ga_7In_6** spectrum, the upfield peaks correspond to μ_2-OH bridges, but as more gallium atoms are introduced into the outermost shell and exchange between the coordinating water ligands and DMSO slows, symmetry is broken, and complexity increases. We now propose to assign these peaks as well. As with the μ_3-OH protons, computations were used to establish the range in which the μ_2-OH protons should be found.

Ga_8In_5

After the **Ga_7In_6** cluster, **Ga_8In_5** is the next easiest to analyze because it only has one isomer. Using the information gained in the μ_3-OH assignment a similar analysis involving integrations of signals and protons signals can be assigned (Figure 3.12). The μ_2-OHint are the same as their μ_3-OH counterparts existing in a 3:2:1 ratio ($H^{\mu_{2int}}_{\mathbf{In}\mathbf{In}\mathbf{In}}$:$H^{\mu_{2int}}_{\mathbf{In}\mathbf{In}\mathbf{Ga}}$:$H^{\mu_{2int}}_{\mathbf{In}\mathbf{Ga}\mathbf{In}}$). The μ_2-OHext appear in an 8:2:2 ratio ($H^{\mu_{2ext}}_{\mathbf{In}\mathbf{In}}$: $H^{\mu_{2ext}}_{\mathbf{In}\mathbf{Ga}}$: $H^{\mu_{2ext}}_{\mathbf{Ga}\mathbf{In}}$), making it difficult to differen- tiate between protons $H^{\mu_{2ext}}_{\mathbf{In}\mathbf{Ga}}$ and $H^{\mu_{2ext}}_{\mathbf{Ga}\mathbf{In}}$. However, Nuclear Overhauser Effect Spectroscopy (NOESY) correlates protons that are near each other through space. The μ_3-OH protons are 3.34 Å and 3.24 Å away from the neighboring μ_2-OHext bridges in the solid state. Since the μ_3-OH and μ_2-OHext bridges are significantly less than 5 Å,[12] they exhibit strong through-space interactions allowing $H^{\mu_{2ext}}_{\mathbf{In}\mathbf{Ga}}$ and $H^{\mu_{2ext}}_{\mathbf{Ga}\mathbf{In}}$ to be assigned using NOESY (Figure 3.13).

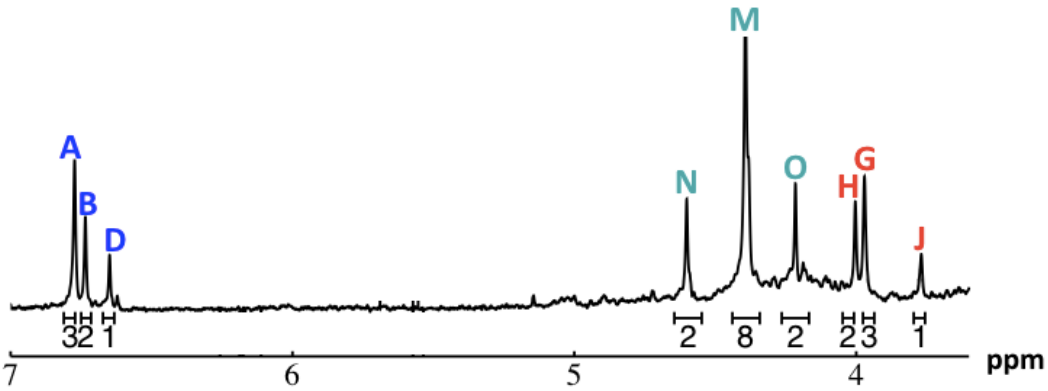

Figure 3.12. The ^{1}H-NMR of 2 mM Ga_8In_5 with peak assignment 1 day after dissolution in d_6-DMSO. $H^{\mu_3}_{\mathbf{In}\mathbf{In}\mathbf{In}}$ (A), $H^{\mu_3}_{\mathbf{In}\mathbf{In}\mathbf{Ga}}$ (B), $H^{\mu_3}_{\mathbf{In}\mathbf{Ga}\mathbf{In}}$ (D), $H^{\mu_{2int}}_{\mathbf{In}\mathbf{In}\mathbf{In}}$ (G), $H^{\mu_{2int}}_{\mathbf{In}\mathbf{In}\mathbf{Ga}}$ (H), $H^{\mu_{2int}}_{\mathbf{In}\mathbf{Ga}\mathbf{In}}$ (J), $H^{\mu_{2ext}}_{\mathbf{In}\mathbf{In}}$ (M), $H^{\mu_{2ext}}_{\mathbf{In}\mathbf{Ga}}$ (N), $H^{\mu_{2ext}}_{\mathbf{Ga}\mathbf{In}}$ (O).

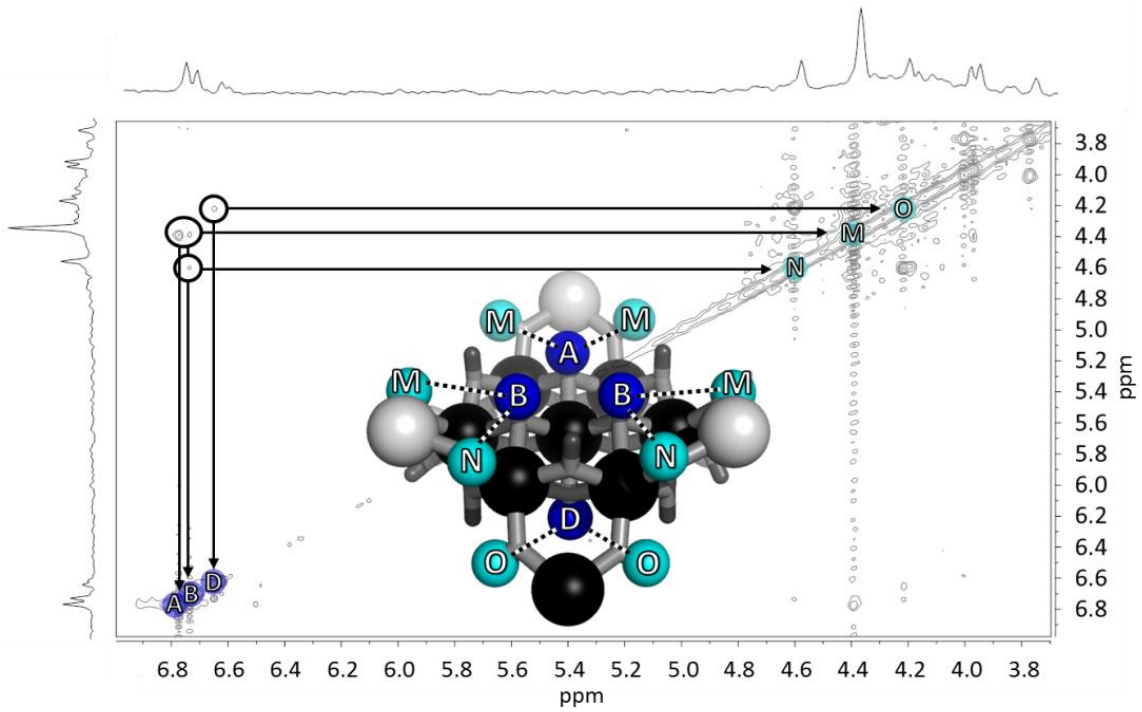

Figure 3.13. The NOESY of Ga_8In_5 indicating the proper peak assignment of the $H^{\mu_{2ext}}_{\mathbf{In}In}$ (M), $H^{\mu_{2ext}}_{\mathbf{In}Ga}$ (N), and $H^{\mu_{2ext}}_{\mathbf{Ga}In}$ (O) protons. Water ligands have been omitted from the structure for clarity. ● Gallium, ○ Indium, $H^{\mu_3}_{In\mathbf{In}In}$ (A), $H^{\mu_3}_{In\mathbf{In}Ga}$ (B), $H^{\mu_3}_{In\mathbf{Ga}In}$ (D).

The use of these experimental results allowed for additional verification of quantum mechanical methods. The assignments based on integration values and the NOESY spectra established a basis of comparison for determining the most accurate computational method. Using the average computed NMR shifts from the structures with counterions for each proton type, the computed proton rankings were an exact match with experimental results. Therefore, we know this computational method can be used to assign the protons in the more complicated spectra with a larger number of isomers and an increasing number of gallium centers.

Ga_9In_4

Ideally **Ga_9In_4** has 5 types of μ_2-OH_{int} and all 4 types of μ_2-OH_{ext} bridges. As previously stated, this cluster has 3 isomers which exist in a 2:2:1 ratio. This means that

the protons in **Ga_9In_4** should integrate to the ratios shown in Table 3.8. Based on these integrations, peaks have been experimentally assigned to the **Ga_9In_4** spectrum (Figure 3.14). Peaks $H^{\mu_{2int}}_{In\mathbf{In}In}$, $H^{\mu_{2int}}_{In\mathbf{In}Ga}$, and $H^{\mu_{2ext}}_{\mathbf{In}Ga}$ are the same as for **Ga_8In_5**. Proton $H^{\mu_{2int}}_{Ga\mathbf{In}Ga}$ which integrates to 1 is too small to identify in the baseline noise between 3.7 and 4.8 ppm. The peak for proton $H^{\mu_{2int}}_{In\mathbf{Ga}In}$ overlaps with $H^{\mu_{2int}}_{Ga\mathbf{Ga}In}$ giving an integration of 5 for the combined signal. There should still be a strong signal at 4.4 ppm from $H^{\mu_{2ext}}_{\mathbf{In}In}$ for **Ga_9In_4**; however, an integration of 14 suggests that proton $H^{\mu_{2ext}}_{\mathbf{Ga}Ga}$ also appears at this chemical shift. Interestingly, the signal for proton $H^{\mu_{2ext}}_{\mathbf{Ga}In}$ seems to have split into two peaks at ~4.2 ppm. This is most likely due to the slower exchange rate of the outer water ligands on gallium. Because $H^{\mu_{2ext}}_{\mathbf{Ga}In}$ is bridging an outer gallium atom this may be the first sign of the complex spectrum we see for **Ga_{13}**. This may also explain the small shoulder/splitting of peak $H^{\mu_{2ext}}_{\mathbf{In}Ga}$ and $H^{\mu_{2ext}}_{\mathbf{In}In}$/$H^{\mu_{2ext}}_{\mathbf{Ga}Ga}$.

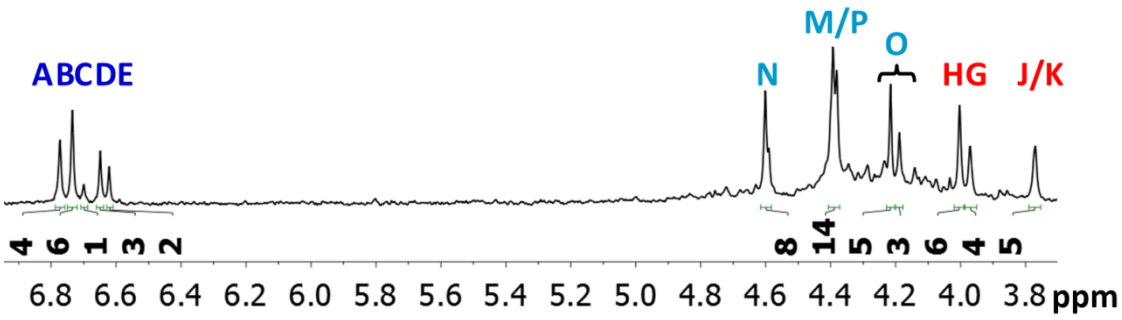

Figure 3.14. The ^{1}H-NMR of 2 mM Ga_9In_4 with experimental peak assignment 1 day after dissolution in d_6-DMSO. $H^{\mu_3}_{In\mathbf{In}In}$ (A), $H^{\mu_3}_{In\mathbf{In}Ga}$ (B), $H^{\mu_3}_{Ga\mathbf{In}Ga}$ (C), $H^{\mu_3}_{In\mathbf{Ga}In}$ (D), $H^{\mu_3}_{Ga\mathbf{Ga}In}$ (E), $H^{\mu_{2int}}_{In\mathbf{In}In}$ (G), $H^{\mu_{2int}}_{In\mathbf{In}Ga}$ (H), $H^{\mu_{2int}}_{In\mathbf{Ga}In}$ (J), $H^{\mu_{2int}}_{Ga\mathbf{Ga}In}$ (K), $H^{\mu_{2ext}}_{\mathbf{In}In}$ (M), $H^{\mu_{2ext}}_{\mathbf{In}Ga}$ (N), $H^{\mu_{2ext}}_{\mathbf{Ga}In}$ (O), $H^{\mu_{2ext}}_{\mathbf{Ga}Ga}$ (P).

Computations are particularly useful for corroborating the assignments in the spectra of **Ga_9In_4**. Because many of the peaks overlap with others, the integrations are no longer solely reliable for making full assignments. Therefore, the relative values of the computed NMR shiftswere used alongside the known assignments from **Ga_7In_6** and **Ga_8In_5** for the most precise results. This allowed for the $H^{\mu_{2ext}}_{\mathbf{In}In}$ and $H^{\mu_{2ext}}_{\mathbf{Ga}Ga}$ peaks to be distinguished, as well as the $H^{\mu_{2ext}}_{\mathbf{Ga}In}$ and $H^{\mu_{2int}}_{Ga\mathbf{In}Ga}$ peaks (Figure 3.15). For the $H^{\mu_{2ext}}_{\mathbf{In}In}$ and $H^{\mu_{2ext}}_{\mathbf{Ga}Ga}$ peaks, computations showed that the $H^{\mu_{2ext}}_{\mathbf{In}In}$ peak should have a slightly downfield chemical shift compared to $H^{\mu_{2ext}}_{\mathbf{Ga}Ga}$. Likewise, the computed shift for the $H^{\mu_{2int}}_{Ga\mathbf{In}Ga}$was compared to the signals from the other internal and external μ_2-OH protons. This analysis showed that I should have the farthest downfield shift of the internal μ_2-OH protons, but should not be higher than any of the external μ_2-OH protons. After determining the identity of the peaks in the **Ga_9In_4** spectrum, this method was used to further assign the peaks in the spectra of the clusters with increasing gallium content.

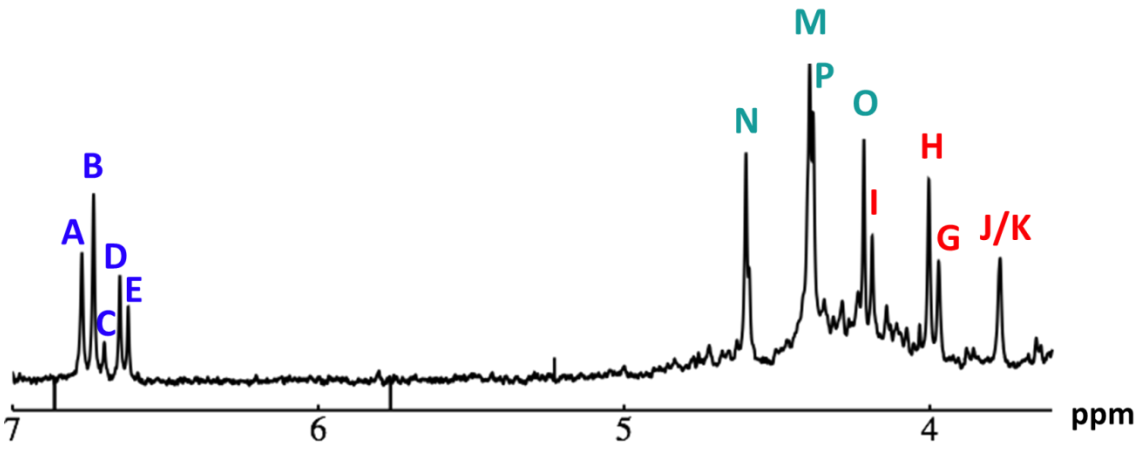

Figure 3.15. The ^{1}H-NMR of 2 mM Ga_9In_4 with computed peak assignment 1 day after dissolution in d_6-DMSO. $H^{\mu_3}_{In\mathbf{In}In}$ (A), $H^{\mu_3}_{In\mathbf{In}Ga}$ (B), $H^{\mu_3}_{Ga\mathbf{In}Ga}$ (C), $H^{\mu_3}_{In\mathbf{Ga}In}$ (D), $H^{\mu_3}_{Ga\mathbf{Ga}In}$ (E), $H^{\mu_{2int}}_{In\mathbf{In}In}$ (G), $H^{\mu_{2int}}_{In\mathbf{In}Ga}$ (H), $H^{\mu_{2int}}_{Ga\mathbf{In}Ga}$ (I), $H^{\mu_{2int}}_{In\mathbf{Ga}In}$ (J), $H^{\mu_{2int}}_{Ga\mathbf{Ga}In}$ (K), $H^{\mu_{2ext}}_{\mathbf{In}In}$ (M), $H^{\mu_{2ext}}_{\mathbf{In}Ga}$ (N), $H^{\mu_{2ext}}_{\mathbf{Ga}In}$ (O), $H^{\mu_{2ext}}_{\mathbf{Ga}Ga}$ (P).

$Ga_{10}In_3$-Ga_{13}

Experimental data suggests that **$Ga_{10}In_3$** also exists as three isomers but, in a 3:6:1 ratio leading to the peak integrations listed in Table 3.8. Unfortunately, the complexity caused by the increasing number of exterior gallium atoms and the isomers does not allow these signals to be assigned experimentally. Similar issues arise for **$Ga_{11}In_2$** to **Ga_{13}**. Given the complexity of the signals arising from the protons in these clusters, computations are particularly useful for peak assignment.

Computed shifts were used to assign the remaining types of protons for each of these clusters (Figure 3.16). Unfortunately, we are unable to compute the changes based on coordinated DMSO breaking the symmetry; therefore, only the peaks of the "mother cluster" (fully H_2O ligated) can be assigned in these spectra. Primarily, this involved computing the position of proton signal $H^{\mu_{2int}}_{\mathbf{Ga}Ga\mathbf{Ga}Ga}$, which represents the protons in a section of the cluster with three external gallium ions next to each other. Computed

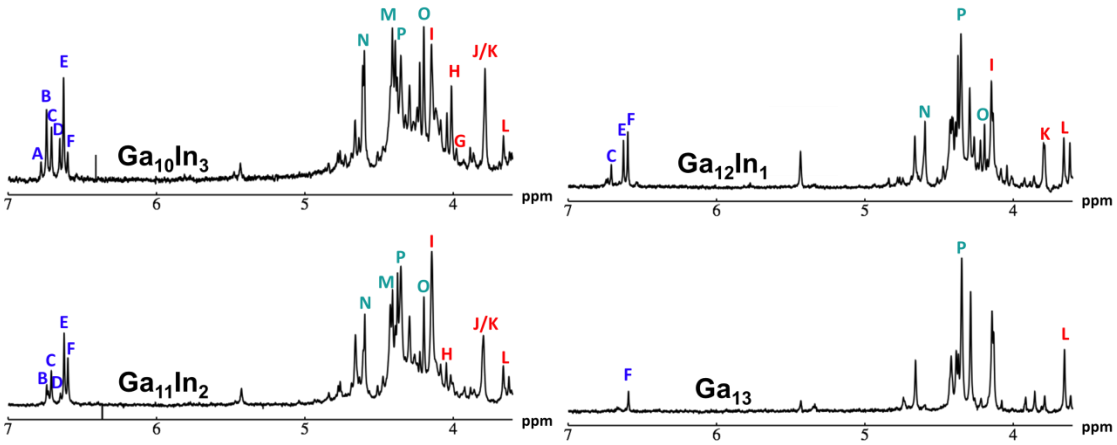

Figure 3.16. Computed results for μ_3-OH and μ_2-OH proton signals are shown overlaid with ^{1}H-NMR spectra of 2 mM $Ga_{10}In_3$, $Ga_{11}In_2$, $Ga_{12}In_1$, and Ga_{13} cluster in d_6-DMSO one day after dissolution $H^{\mu_3}_{In\mathbf{In}In}$ (A), $H^{\mu_3}_{In\mathbf{In}Ga}$ (B), $H^{\mu_3}_{Ga\mathbf{In}Ga}$ (C), $H^{\mu_3}_{In\mathbf{Ga}In}$ (D), $H^{\mu_3}_{Ga\mathbf{Ga}In}$ (E), $H^{\mu_3}_{Ga\mathbf{Ga}Ga}$ (F), $H^{\mu_{2int}}_{In\mathbf{In}In}$ (G), $H^{\mu_{2int}}_{In\mathbf{In}Ga}$ (H), $H^{\mu_{2int}}_{Ga\mathbf{In}Ga}$ (I), $H^{\mu_{2int}}_{In\mathbf{Ga}In}$ (J), $H^{\mu_{2int}}_{Ga\mathbf{Ga}In}$ (K), $H^{\mu_{2int}}_{Ga\mathbf{Ga}Ga}$ (L), $H^{\mu_{2ext}}_{\mathbf{In}In}$ (M), $H^{\mu_{2ext}}_{\mathbf{In}Ga}$ (N), $H^{\mu_{2ext}}_{\mathbf{Ga}In}$ (O), $H^{\mu_{2ext}}_{\mathbf{Ga}Ga}$ (P).

results suggest that $H^{\mu_{2int}}_{GaGaGaGa}$ should have the lowest shift of all of the internal μ_2-OH protons, which is the lowest ppm value for all of the computed signals.

The **Ga_{13}** mother cluster peaks ($H^{\mu_3}_{GaGaGaGa}$, $H^{\mu_{2int}}_{GaGaGaGa}$, and $H^{\mu_{2ext}}_{GaGa}$) assigned via computations were thereafter confirmed experimentally. By plotting the ^{1}H-NMR spectra of **Ga_{13}** dissolved in a variety of ratios of d_6-DMSO and d_7-DMF, it is clearly visible that only 3 peaks persist from 100% d_6-DMSO to 100% d_7-DMF (Figure 3.17). The other peaks visible in the spectra are caused by "daughter clusters" substituted with either DMSO or DMF ligands at the aquo sites; therefore, the only shared species must be the mother cluster.

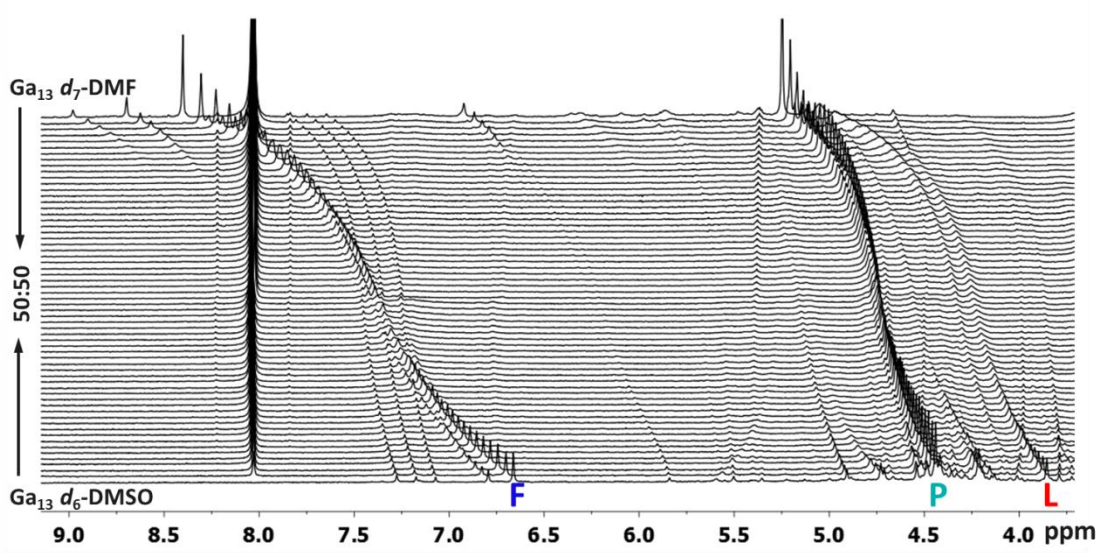

Figure 3.17. Stacked titration data indicating that only the $H^{\mu_3}_{GaGaGaGa}$(F), $H^{\mu_{2int}}_{GaGaGaGa}$ (L), and $H^{\mu_{2ext}}_{GaGa}$ (P) protons translate from the 100% d_6-DMSO to the 100% d_7-DMF spectrum. The triplet that persists in the 7.0 to 7.5 ppm region is attributed to ammonia in the sample.[117]

Conclusion

This research has led to quick and cost effective differentiation and structural characterization of the **$Ga_{13-x}In_x$** clusters in solution via ^{1}H-NMR spectrscopy.[117] We

have shown that each mixed $\mathbf{Ga_{13-x}In_x}$ cluster does independently exist in solution and that there are no kinetically or enthalpically favored isomers (i.e., only the expected statistical ratios of the various isomers were observed). These isomers exist in statistical ratios determined by probability of formation. In general, this study provides a complete method for experimentally and computationally predicting proton shifts for inorganic μ_3-OH and μ_2-OH signals in gallium and indium species, as well as, a literature review of hydroxide bridges for all diamagnetic metals available in the literature to the best of our knowledge. This knowledge will initiate the study of cluster dynamics in solution, allowing for better control and manipulation of precursor clusters. The solution behavior of clusters condensing into films is a primary interest of this research; however, inorganic cluster species are not only relevant to the thin film and electronics markets. Many small clusters, including the $\mathbf{Ga_{13-x}In_x}$ clusters have structures much like fragment of minerals. The reverse process, bulk material breaking down into smaller components (i.e. minerals dissolving in acid rain) is a promising environment for locating dynamic clusters. It is possible that a plethora of clusters form naturally as minerals dissolve, but we have had no way of detecting these intermediate molecules. Geoscience may be greatly affected by the use of ^{1}H-NMR for the observation of inorganic –OH bridges. Al_{13} Keggin and calcium carbonate clusters have both been detected in nature.[118,119] It would be beneficial for the geoscience community to investigate water samples from streams, caves, hot springs, geysers, and ocean vents for the presence of these observable hydroxo bridges. ^{1}H-NMR research on completely inorganic systems is limited, but this study shows that it can lead to a variety of information previously thought to be inaccessible.

Bridge to Chapter IV

By assigning the specific signals in the ^{1}H-NMR spectra of the clusters to protons in the structure, we can now focus on the initial goals of this project. In Chapter IV, we begin to investigate the solution dynamics of these clusters by looking at the kinetic and thermodynamic properties.

CHAPTER IV

SOLUTION DYNAMICS, KINETICS, AND THERMODYNAMICS OF $Ga_{13-x}In_x$ ($0 \leq x \leq 6$) CLUSTERS INVESTIGATED VIA ^{1}H-NMR

Contributions

I conducted the majority of the work for the first two sections of this chapter. I ran most of the NMR experiments and tabulated all of the data. Caitlyn R. Hazlett, an undergraduate research student, synthesized the mixed clusters used for the work. Mary K. Baumeister, a high school summer intern, conducted the experiments with **Ga_8In_5** and varying $In(NO_3)_3$ concentrations. Prof. Darren W. Johnson was the principle investigator for this work and provided editorial assistance.

Introduction

To date we have been able to observe and assign the proton signals of the $Ga_{13-x}In_x(\mu_3\text{-}OH)_6(\mu\text{-}OH)_{12}(H_2O)_{18}(NO_3)_{15}$ ($0 \leq x \leq 6$, **Ga_{13}**, **$Ga_{12}In_1$**, **$Ga_{11}In_2$**, **$Ga_{10}In_3$**, **Ga_9In_4**, **Ga_8In_4**, **Ga_7In_6**) clusters via ^{1}H-NMR in wet deuterated aprotic solvent.[19,59] The interesting role these clusters play in the formation of thin films brings them to our attention. The reverse process (dissolution of minerals) is also a fundamental area of inquiry. Due to the recent experimental and computational ^{1}H-NMR correlation of the solution to XRD solid state structure we can address the underlying questions involving the solution dynamics of these clusters more accurately. Thus far, two types of dynamic behavior have been observed using ^{1}H-NMR (Figure 4.1). In this manuscript we will discuss exterior metal ion exchange and capping ligand/solvent exchange.

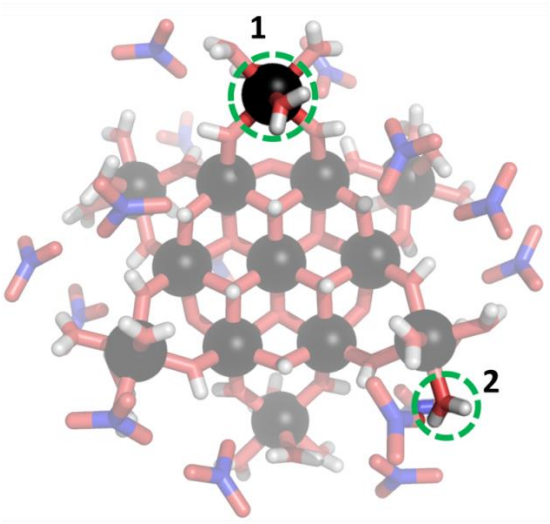

Figure 4.1. The two types of dynamic behavior observed by ^{1}H-NMR for the $Ga_{13-x}In_x(\mu_3\text{-}OH)_6(\mu\text{-}OH)_{12}(H_2O)_{18}(NO_3)_{15}$ ($0 \leq x \leq 6$) clusters: 1) exterior metal exchange and 2) ligand exchange.

Exterior Metal Ion Exchange

Ageing and stability studies indicated that **Ga_8In_5** and **Ga_9In_4** become **Ga_7In_6** over time. Additionally, **$Ga_{12}In_1$** and **$Ga_{11}In_2$** become **Ga_{13}** at the same relative rate. At room temperature, 2mM solutions of **$Ga_{13-x}In_x$** ($1 \leq x \leq 5$) in d_6-DMSO take approximately a week on average for this conversion to occur. By looking at the simplest example, **Ga_8In_5**, we can determine information about the exchange kinetics and thermodynamics of the outer metal ions in the clusters. It is proposed that Scheme 4.1 represents the

$$Ga_8In_5(\mu_3\text{-}OH)_6(\mu\text{-}OH)_{18}(H_2O)_{24}(NO_3)_{15} + In(NO_3)_3$$

$$\downarrow\uparrow$$

$$Ga_7In_6(\mu_3\text{-}OH)_6(\mu\text{-}OH)_{18}(H_2O)_{24}(NO_3)_{15} + Ga(NO_3)_3$$

Scheme 4.1. Conversion of Ga_8In_5 to Ga_7In_6.

transmetallation reaction if it is assumed there is $In(NO_3)_3$ contamination or partial dissociation of the cluster in solution leading to free monomer. This reaction is observed

by the disappearance of peaks $H^{\mu_3}_{\mathrm{In}\mathbf{In}\mathrm{Ga}}$, $H^{\mu_3}_{\mathrm{In}\mathbf{Ga}\mathrm{In}}$, $H^{\mu_{2int}}_{\mathrm{In}\mathbf{In}\mathrm{Ga}}$, $H^{\mu_{2int}}_{\mathrm{In}\mathbf{Ga}\mathrm{In}}$, $H^{\mu_{2ext}}_{\mathbf{In}\mathrm{Ga}}$ and $H^{\mu_{2ext}}_{\mathbf{Ga}\mathrm{In}}$, which are all in an environment with one Ga(III) ion. The peaks associated with external In(III) ion saturation ($H^{\mu_3}_{\mathrm{In}\mathbf{In}\mathrm{In}}$,$H^{\mu_{2int}}_{\mathrm{In}\mathbf{In}\mathrm{In}}$, and $H^{\mu_{2ext}}_{\mathbf{In}\mathrm{In}}$) persist as those peaks indicative of single Ga(III) substitution wane (Figure 4.2). Similar expected changes in proton signals occur as **Ga_9In_4** becomes **Ga_7In_6** and **$Ga_{11}In_2$** or **$Ga_{12}In$** convert to **Ga_{13}**.

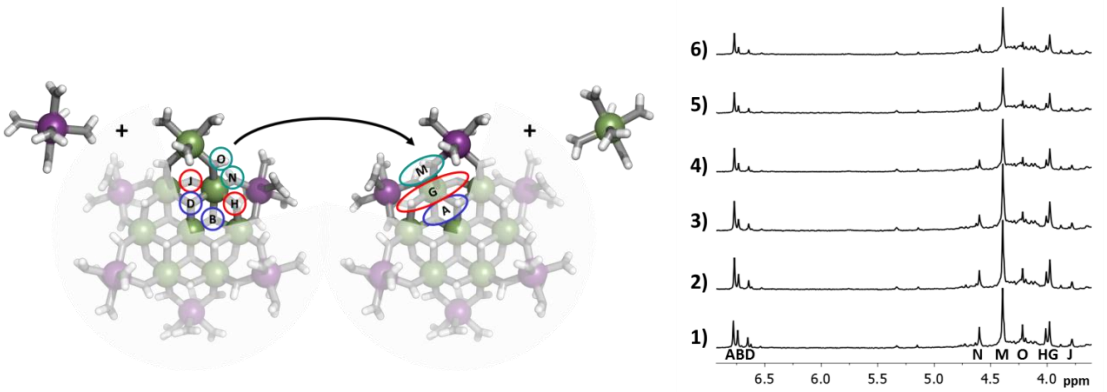

Figure 4.2. Ga_8In_5 to Ga_7In_6 conversion. As the exterior Ga(III) ion in **Ga_8In_5** is replaced with an In(III) ion, the environments of protons $H^{\mu_3}_{\mathrm{In}\mathbf{In}\mathrm{Ga}}$ (B), $H^{\mu_3}_{\mathrm{In}\mathbf{Ga}\mathrm{In}}$ (D), $H^{\mu_{2int}}_{\mathrm{In}\mathbf{In}\mathrm{Ga}}$ (H), $H^{\mu_{2int}}_{\mathrm{In}\mathbf{Ga}\mathrm{In}}$ (J), $H^{\mu_{2ext}}_{\mathbf{In}\mathrm{Ga}}$ (N), and $H^{\mu_{2ext}}_{\mathbf{Ga}\mathrm{In}}$ (O) become that of $H^{\mu_3}_{\mathrm{In}\mathbf{In}\mathrm{In}}$ (A), $H^{\mu_{2int}}_{\mathrm{In}\mathbf{In}\mathrm{In}}$ (G), and $H^{\mu_{2ext}}_{\mathbf{In}\mathrm{In}}$ (M). This can be seen in the ^{1}H-NMR data of a 2 mM **Ga_8In_5** sample in d_6-DMSO over time. 1) Δt = 2 days, 2) Δt = 3 days, 3) Δt = 5 days, 4) Δt = 6 days, 5) Δt = 7 days, 6) Δt = 8 days.

Concentration Studies

The rate at which **Ga_8In_5** becomes **Ga_7In_6** via metal ion exchange is not affected by the initial concentration of cluster in solution (Figure 4.3). Protons $H^{\mu_3}_{\mathrm{In}\mathbf{In}\mathrm{Ga}}$, $H^{\mu_3}_{\mathrm{In}\mathbf{Ga}\mathrm{In}}$, and $H^{\mu_{2int}}_{\mathrm{In}\mathbf{Ga}\mathrm{In}}$ were selected for data collection due to the ease of integration and the suitable adjoining baseline. Rearranging the first-ordered integrated rate law (Equation 4.1) into the formula for a line (Equation 4.2) allows rate constants to be easily obtained by plotting ln[proton X] (M, X = $H^{\mu_3}_{\mathrm{In}\mathbf{In}\mathrm{Ga}}$, $H^{\mu_3}_{\mathrm{In}\mathbf{Ga}\mathrm{In}}$, or $H^{\mu_{2int}}_{\mathrm{In}\mathbf{Ga}\mathrm{In}}$) vs time (s). The linear

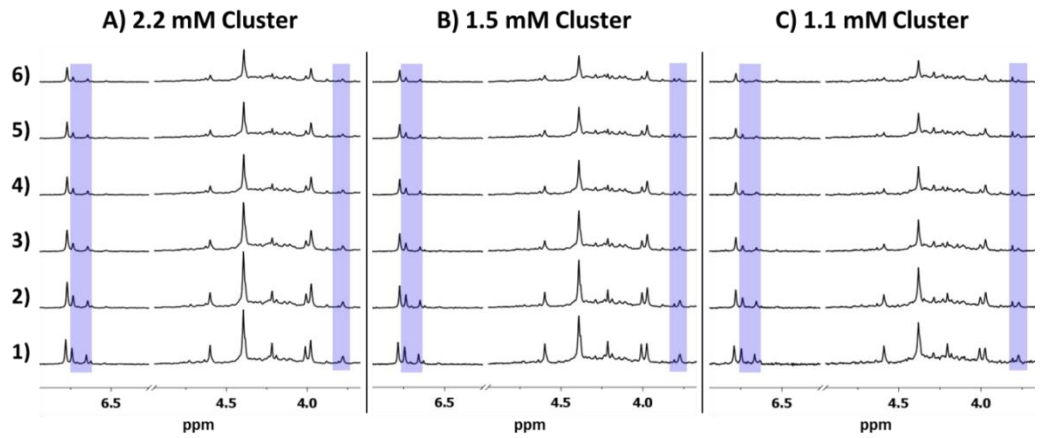

Figure 4.3. Various concentrations of Ga_8In_5 over time (d_6-DMSO). Peaks $H^{\mu_3}_{InInGa}$, $H^{\mu_3}_{InGaIn}$, and $H^{\mu_{2int}}_{InGaIn}$ are highlighted in blue. 1) Δt = 2 days, 2) Δt = 3 days, 3) Δt = 4 days, 4) Δt = 5 days, 5) Δt = 6 days, and 6) Δt = 7 days.

$$[A] = [A]_0\, e^{-kt} \qquad \textbf{(Eqn. 4.1)}$$

$$\ln[A] = -kt + \ln[A]_0 \qquad \textbf{(Eqn. 4.2)}$$

correlation of these plots indicates an overall first order reaction (Figure 4.4A).The consistency in k (-slope) from one concentration of cluster to the next reveals that the reaction is 0^{th} order with respect to cluster (Table 4.1). Interestingly, the reaction is also

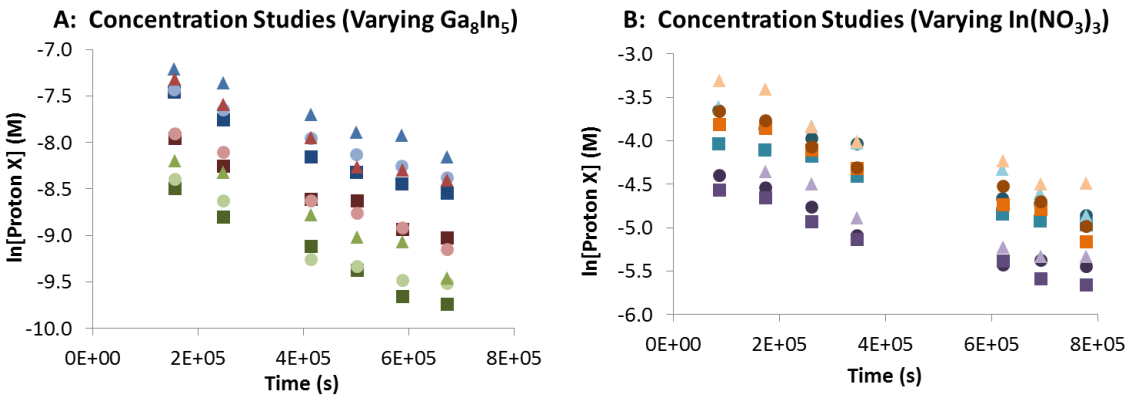

Figure 4.4. The change in concentration of protons $H^{\mu_3}_{InInGa}$ (■), $H^{\mu_3}_{InGaIn}$ (●), and $H^{\mu_{2int}}_{InGaIn}$ (▲) at three different Ga_8In_5/$In(NO_3)_3$ concentrations over time (A: blue = 2.2 mM **Ga_8In_5**, red = 1.5 mM **Ga_8In_5**, green = 1.1 mM **Ga_8In_5**; B: orange = no additional $In(NO_3)_3$ added, teal = 3x excess $In(NO_3)_3$, purple = 5x excess $In(NO_3)_3$).

0^{th} order with respect to $In(NO_3)_3$ salt (Figure 4.4B, Table 4.1). Therefore, the reaction is 1^{st} order with respect to an unknown species with a rate constant (k) at room temperature of $1.9x10^{-6} \pm 0.3x10^{-6}$ s^{-1}. The slight deviation in average k values between "the change in cluster concentration" and "the change in salt concentrations" is most likely due to variations in temperature of the ambient environment during the experiments.

Table 4.1. Rate constant (k) for the Ga_8In_5 conversion to Ga_7In_6 at room temperature calculated from data in Figure 4.4 (k = -slope). Average k at room temperature is $1.9x10^{-6} \pm 0.3x10^{-6}$ s^{-1}.

$[Ga_8In_5]$ (mM)	Additional $[In(NO_3)_3]$ (mM)	$H^{\mu_3}_{\mathrm{In}\mathbf{In}\mathrm{Ga}}$		$H^{\mu_3}_{\mathrm{In}\mathbf{Ga}\mathrm{In}}$		$H^{\mu_{2int}}_{\mathrm{In}\mathbf{Ga}\mathrm{In}}$		Average k x10^{-6} (s^{-1})
		k x10^{-6} (s^{-1})	R^2	k x10^{-6} (s^{-1})	R^2	k x10^{-6} (s^{-1})	R^2	
2.2	0	2.1	0.98	1.8	0.99	1.8	0.99	1.9 ± 0.2
1.5	0	2.0	0.97	2.4	0.99	2.2	0.97	2.2 ± 0.2
1.1	0	2.4	0.99	2.3	0.94	2.4	0.98	2.4 ± 0.1
1.8	0	1.5	0.98	1.8	0.96	1.6	0.93	1.6 ± 0.1
1.7	5.5	1.9	0.99	1.8	0.99	1.7	0.96	1.8 ± 0.1
1.8	8.8	1.6	0.97	1.6	0.93	1.7	0.94	1.6 ± 0.1

Variable Temperature Studies

By observing the metal exchange using NMR experiments at elevated temperatures of 45°C and 50°C, thermodynamic information is gained. Figure 4.5A plots the concentration changes of protons $H^{\mu_3}_{\mathrm{In}\mathbf{In}\mathrm{Ga}}$, $H^{\mu_3}_{\mathrm{In}\mathbf{Ga}\mathrm{In}}$, and $H^{\mu_{2int}}_{\mathrm{In}\mathbf{Ga}\mathrm{In}}$ over time at different temperatures using Equation 4.2. At elevated temperatures the signal for proton $H^{\mu_3}_{\mathrm{In}\mathbf{In}\mathrm{Ga}}$ overlaps with that of $H^{\mu_3}_{\mathrm{In}\mathbf{In}\mathrm{In}}$ making it impossible to integrate, proton $H^{\mu_{2int}}_{\mathrm{In}\mathbf{Ga}\mathrm{In}}$ eventually broadens into the baseline, but the signal from proton $H^{\mu_3}_{\mathrm{In}\mathbf{Ga}\mathrm{In}}$ is always acceptable for data analysis. The conversion time reduces from one week to a few hours with the addition of heat. The slope of each data set provides the rate constant at each temperature

(Table 4.2). Activation energy (E_a) can be determined using the Arrhenius equation (Equation 4.3). If this equation is rearranged into the formula for a line (Equation 4.4), then the slope of the line produced by plotting ln(k) vs. 1/RT is $-E_a$ (Figure 4.5B). For **Ga_8In_5** becoming **Ga_7In_6** the E_a is 140 kJ/mol (32 kcal/mol).

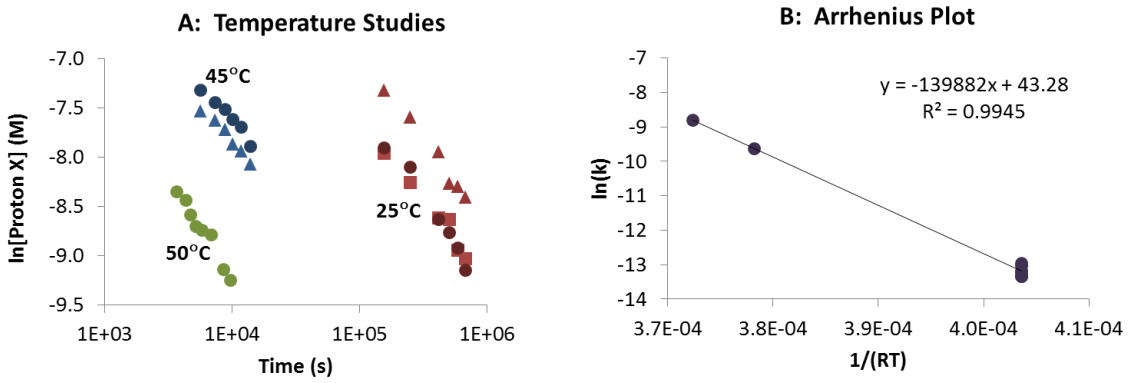

Figure 4.5. Temperature studies and Arrhenius plot. A) The change in concentration of protons $H^{\mu_3}_{\mathbf{In}\mathbf{In}\mathbf{Ga}}$(■), $H^{\mu_3}_{\mathbf{In}\mathbf{Ga}\mathbf{In}}$ (●), and $H^{\mu_{2int}}_{\mathbf{In}\mathbf{Ga}\mathbf{In}}$ (▲) at three different temperatures. B) The Arrhenius Plot determining Activation Energy (E_a).

Table 4.2. Rate constants (k) calculated for the Ga_8In_5 conversion to Ga_7In_6 at a variety of temperatures from data in Figure 4.5A (k = -slope). Standard deviations (STDEV) are reported for experiments with multiple trials. R^2 values are reported for experiments with only one trial.

Temperature (°C)	$H^{\mu_3}_{\mathbf{In}\mathbf{In}\mathbf{Ga}}$		$H^{\mu_3}_{\mathbf{In}\mathbf{Ga}\mathbf{In}}$		$H^{\mu_{2int}}_{\mathbf{In}\mathbf{Ga}\mathbf{In}}$		Average k (s^{-1})
	k (s^{-1})	R^2/STDEV	k (s^{-1})	R^2/STDEV	k (s^{-1})	R^2/STDEV	
25 (averages)	$1.9x10^{-6}$	$\pm 0.3x10^{-6}$	$2.0x10^{-6}$	$\pm 0.3x10^{-6}$	$1.9x10^{-6}$	$\pm 0.3x10^{-6}$	$1.9x10^{-6}$
45	-	-	$6.5x10^{-5}$	0.99	$6.6x10^{-5}$	0.99	$6.6x10^{-5}$
50	-	-	$1.5x10^{-4}$	0.97	-	-	-

$$k = Ae^{\frac{-E_a}{RT}} \qquad \textbf{(Eqn. 4.3)}$$

$$\ln(k) = -E_a\left(\frac{1}{RT}\right) + \ln(A) \qquad \textbf{(Eqn. 4.4)}$$

More thermodynamic data ($\Delta G^{\ddagger}$, $\Delta H^{\ddagger}$, and $\Delta S^{\ddagger}$) can be ascertained from this experiment using the previously determined rate constants (k), Activation Energy (E_a),

and temperatures. Equations 4.5-4.7 can be used to simply solve for the thermodynamic properties. $\Delta H^{\ddagger}$ and $\Delta S^{\ddagger}$ can also be found using the Erying Equation (Equation 4.8, Figure 4.6). A combination of these two methods ensures accuracy when determining the properties. Table 4.3 presents the thermodynamic data for the conversion of **Ga_8In_5** to **Ga_7In_6.**

$$\Delta G^{\ddagger} = RT\left[23.76 + \ln\left(\frac{T}{k}\right)\right] \quad \textbf{(Eqn. 4.5)}$$

$$\Delta H^{\ddagger} = E_a - RT \quad \textbf{(Eqn. 4.6)}$$

$$\Delta S^{\ddagger} = \frac{\left[(E_a - RT) - \Delta G^{\ddagger}\right]}{T} \quad \textbf{(Eqn. 4.7)}$$

$$\ln\left(\frac{k}{T}\right) = -\left(\frac{\Delta H^{\ddagger}}{R}\right)\left(\frac{1}{T}\right) + \left(\frac{\Delta S^{\ddagger}}{R} + 23.76\right) \quad \textbf{(Eqn. 4.8)}$$

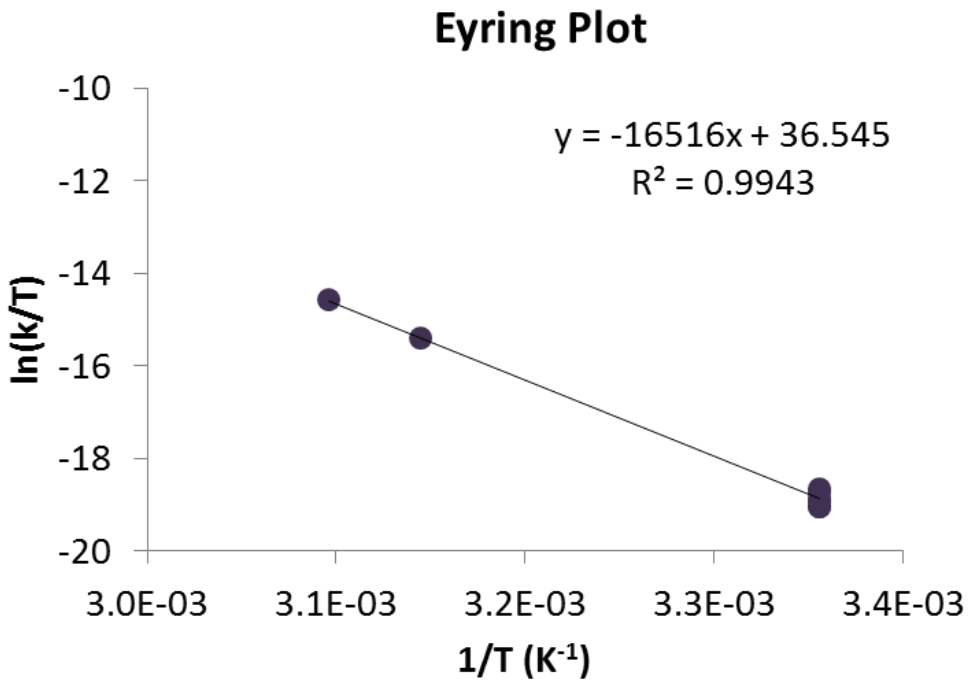

Figure 4.6. Erying plot from Equation 4.8 used to calculate $\Delta H^{\ddagger}$ and $\Delta S^{\ddagger}$ for **Ga_8In_5** converting to **Ga_7In_6**.

Table 4.3. Average thermodynamic data for the exchange of Ga_8In_5 to Ga_7In_6.

Units	kJ/mol	kcal/mol
E_a	140	33
$\Delta G^{\ddagger}$	110	25
$\Delta H^{\ddagger}$	140	33
$\Delta S^{\ddagger}$	0.11	0.025

The energies associated with the activation parameters for this exchange are considerably less than the bond dissociation energy of one G-OH bond (102 kcal/mol), let alone two.[120] This suggests an associative mechanism; however, the complexity of this system is likely to be strongly influenced by solvation effects. Further research is needed to differentiate the solvation effects from the reaction kinetics.

Ligand Exchange (DMSO/H_2O)

As we previously published, over the first few days in solution the ^{1}H-NMR signals of **Ga_{13}** simplify.[19] We stated this was due to an equilibrium between the solvent (DMSO) and the outer capping water ligands of the cluster.[19] The consistency of the hydrodynamic radius over this time period bolstered the speculation. This hypothesis still stands; however, our current theory is that **Ga_{13}** is almost completely ligated by DMSO in the dissolution process, followed by an equilibrium favoring the re-ligation of the cluster by H_2O (Scheme 4.2). The immense excess of DMSO drives the initial dissolution and ligation of the cluster, but the favorability of water as a capping ligand eventually prevails in the equilibrium. Three experiments unambiguously point to this conclusion. Scheme 4.2 also takes into account data which indicates that the cluster deprotonates at the μ_3-OH sites during this process.

$$Ga_{13}(\mu_3\text{-}OH)_6(\mu\text{-}OH)_{18}(H_2O)_{24-x}(DMSO)_x(NO_3)_{15} + 6NO_3^- + yH_2O$$

$$\downarrow\uparrow$$

$$Ga_{13}(\mu_3\text{-}O)_6(\mu\text{-}OH)_{18}(H_2O)_{(24-x)+y}(DMSO)_{x-y}(NO_3)_{21} + 6H^+ + yDMSO$$

Scheme 4.2. Ligand Exchange on Ga_{13}.

Evidence of DMSO Binding

^{1}H-NMR data supports the conclusion that DMSO binds to the **Ga_{13}** cluster. By running a ^{1}H-NMR of **Ga_{13}** in protio DMSO (with a d_6-DMSO insert to lock on), the cluster was able to interact solely with solvent that produces NMR signals. There are 3 possible substitution sites on the exterior of the cluster. For the water ligands these are referred to as axial, equatorial, and center (Figure 2.1). These are not seen in the ^{1}H-NMR.[59] Figure 4.7C reveals 3 new signals that arise in the protio DMSO sample. Diffusion Ordered Spectroscopy (DOSY) data indicates that these 3 peaks diffuse at a similar rate to the peaks associated with the cluster (Figure 4.7D). The measured diffusion coefficients, along with the number of new peaks produced, substantiates the claim that DMSO is binding.

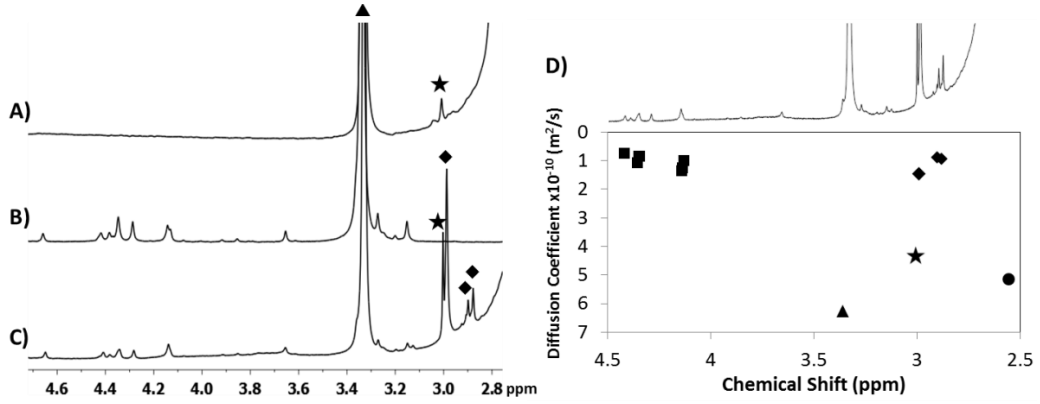

Figure 4.7. ^{1}H-NMR evidence DMSO binds to cluster. ^{1}H-NMR spectra for A) DMSO with a d_6-DMSO insert, B) 2 mM **Ga_{13}** in d_6-DMSO, and C) 2 mM **Ga_{13}** in DMSO with a d_6-DMSO insert. D) DOSY of sample C. (★) DMSO impurity (●) DMSO solvent (◆) DMSO "bound" (▲) H_2O (■) cluster hydroxides.

Aging/Simplification Study

The computational assignment of mother cluster protons ($H^{\mu_3}_{Ga\mathbf{Ga}Ga}$, $H^{\mu_{2int}}_{Ga\mathbf{Ga}Ga}$, and $H^{\mu_{2ext}}_{\mathbf{Ga}Ga}$) to specific peaks in the **Ga$_{13}$** spectrum allows us to investigate the aging studies with more detail.[59] These protons correspond to the 3 types of bridging hydroxides in the **Ga$_{13}$** cluster if it is fully ligated by water. The simplification process was observed in more detail over a shorter period of time by conducting a variable temperature NMR experiment (Figure 4.8). Monitoring the hydrodynamic radius by DOSY during heating indicates that the structure is stable at these temperatures. Diffusion coefficient alone cannot be used to determine stability at elevated temperatures due to changes in viscosity (η). The Einstein Stokes approximation (Equation 2.1) takes this into consideration when calculating size using the diffusion coefficient.

There are initially two types of μ_3-OH signals, which appear farthest downfield between 6.5-6.8 ppm. These are the protons that would be least effected by outer ligand changes because they are the furthest away spatially. One is proton $H^{\mu_3}_{Ga\mathbf{Ga}Ga}$ (F), the μ_3-OH of the mother **Ga$_{13}$** cluster, and the other signal $H^{\mu_3}_{Ga\mathbf{Ga}Ga_D}$ corresponds to a DMSO substituted daughter cluster. Although proton $H^{\mu_3}_{Ga\mathbf{Ga}Ga}$ (F) first grows in while $H^{\mu_3}_{Ga\mathbf{Ga}Ga_D}$ disappears, eventually both are gone due to de-protonation. The additional downfield shift of the μ_3-OH protons is evidence that these are the most acidic hydroxide bridge protons in the clusters.

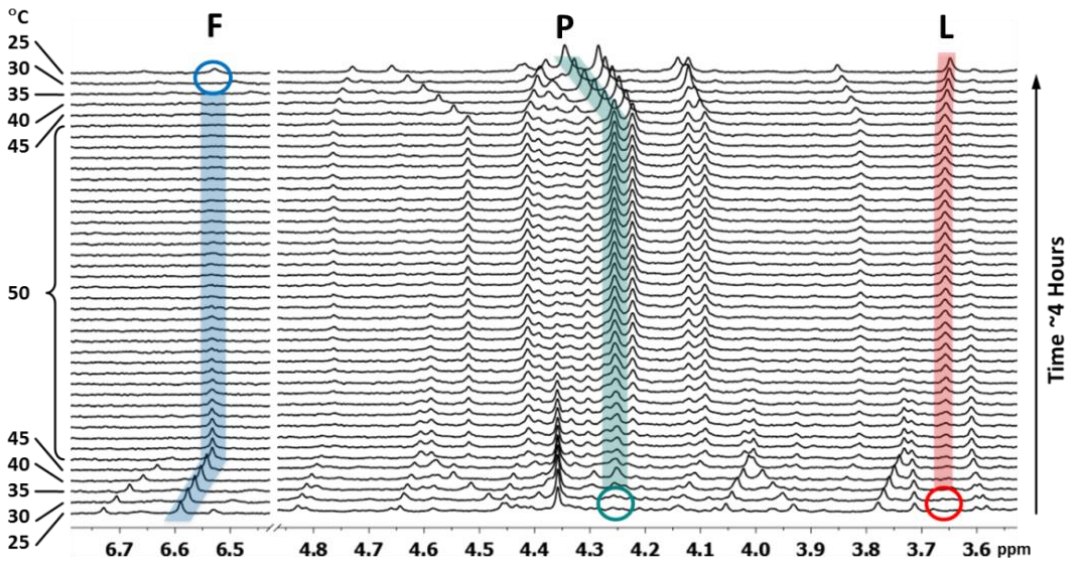

Figure 4.8. Simplification of Ga_{13} ^{1}H-NMR spectrum sped up through heating. Peaks $H^{\mu_3}_{Ga\mathbf{Ga}Ga}$ (F), $H^{\mu_{2int}}_{Ga\mathbf{Ga}Ga}$ (L), and $H^{\mu_{2ext}}_{\mathbf{Ga}Ga}$ (P)correspond to the mother **Ga_{13}** cluster. All others are caused by DMSO ligand substitution.

The μ_2-OH signals $H^{\mu_{2int}}_{Ga\mathbf{Ga}Ga}$(L) and $H^{\mu_{2ext}}_{\mathbf{Ga}Ga}$ (P) are not present in the initial NMR before simplification. This indicates that there are no **Ga_{13}** cluster species present with 100% water ligation. Many of the initial signals disappear through simplification indicating that the initial ligand substitution (possibly close to DMSO saturation) does not persist over time. The final stabilized spectrum still has DMSO substitution indicated by the unassigned signals; however, the amount of water ligation is much higher.

Concentration Studies

When different concentrations of H_2O are added to 2 mM **Ga_{13}** samples, the rate of simplification is changed. Figure 4.9 displays 3 of the 5 concentrations examined in this study. Proton $H^{\mu_3}_{Ga\mathbf{Ga}Ga}$ (F), the μ_3-OH signal highlighted in blue, disappears faster

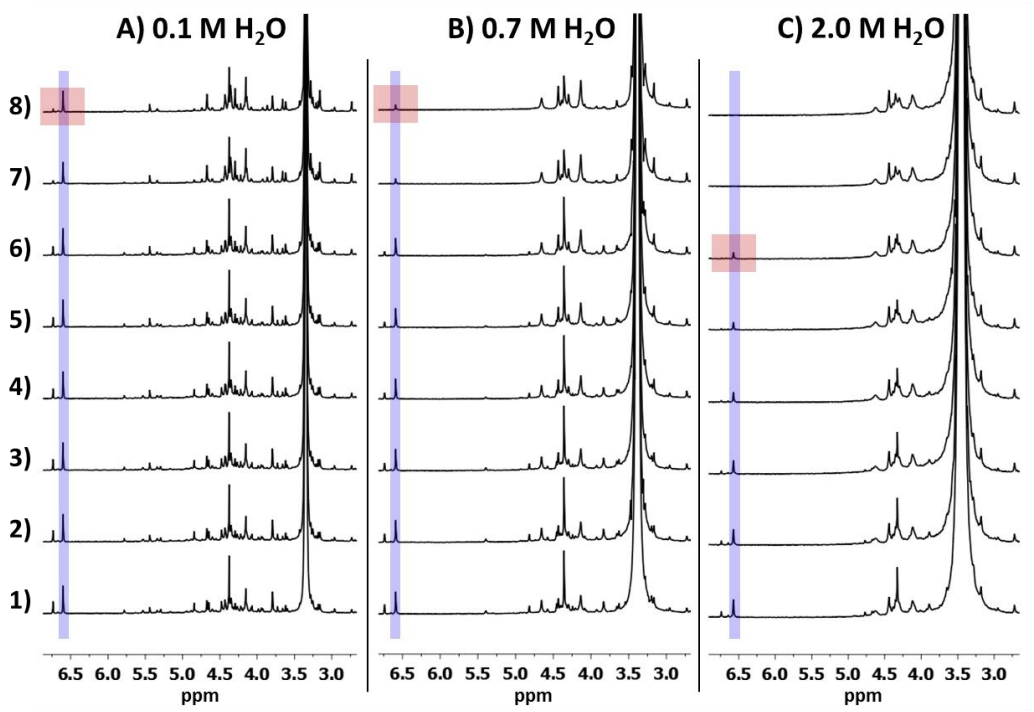

Figure 4.9. Various concentrations of H_2O added to Ga_{13} (2 mM) in d_6-DMSO over time. The signal for μ_3-OH F is highlighted in blue. 1) Δt = 1 hour, 2) Δt = 1.5 hours, 3) Δt = 3 hours, 4) Δt = 4.5 hours, 5) Δt = 6 hours, 6) Δt = 7.5 hours, 7) Δt = 29 hours and 8) Δt = 31 hours.

with the addition of water. This result and Le Chatelier's Principle support the theory that water is a reactant in the equilibrium occurring. If DMSO were the reactant then the addition of water would slow the equilibrium.

This experiment can provide information about the kinetics which occur during the ligand equilibrium. By once again plotting $\ln[H^{\mu_3}_{\mathbf{Ga}GaGa}]$ (M) vs time (s) from equation 2, rate information can be determined (Figure 4.10A). Table 4.4 shows the slope of each line, also known as the rate, in Figure 4.10A. Because the rate is different for each concentration of water, the rates must be plotted against the concentrations to determine the rate constant (k) (Figure 4.10B). The linearity of Figure 4.10A indicates that the ligand exchange on **Ga_{13}** is first order, the changes in rate relative to H_2O concentration

reveal the 1st order is with respect to water, and the slope from Figure 4.10B establish a $k=1.2x10^{-6}$ s^{-1}. Equation 4.9 is the proposed rate law for the **Ga_{13}** exterior ligand equilibrium suggested in scheme 4.2.

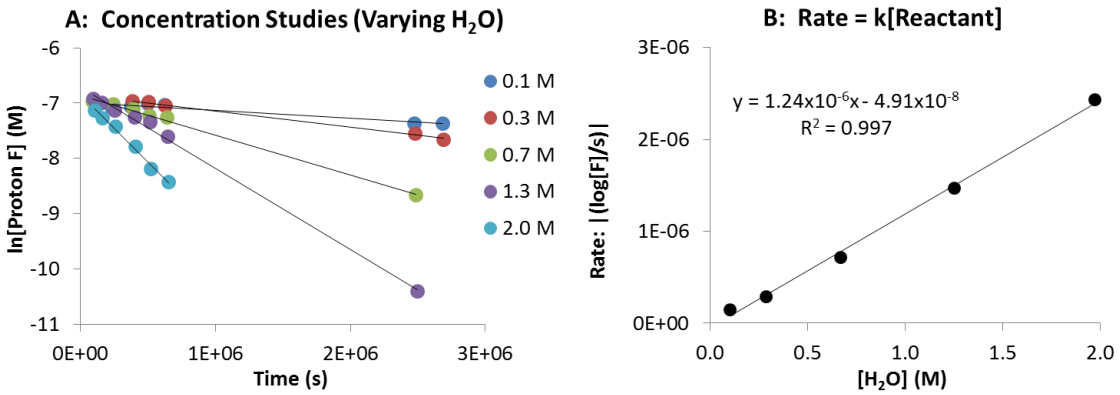

Figure 4.10. Rate calculations for Ga_{13} ligand exchange. A) The change in concentration of proton $H^{\mu_3}_{GaGaGa}$ (F) at five different H_2O concentrations. B) The rate of change over time vs each concentration provides the rate constant of the equilibrium.

Table 4.4. Rate data for the ligand equilibrium of Ga_{13} determined by the slopes of the various data series in Figure 4.10A. R^2 values are reported for experiments with only one trial.

Concentration of H_2O (M)	Trendline Slope/Rate (s^{-1})	Trendline R^2
0.1	-1.45×10^{-7}	0.943
0.3	-2.91×10^{-7}	0.996
0.7	-7.19×10^{-7}	0.995
1.3	-1.47×10^{-6}	0.997
2.0	-2.43×10^{-6}	0.991

$$\text{Rate} = 1.24x10^{-6}[H_2O]^1 \qquad \textbf{(Eqn. 4.9)}$$

Conclusion

In conclusion, kinetic and thermodynamic data has been reported for dynamic behavior observed by ^{1}H-NMR for **$Ga_{13-x}In_x$** ($0 \le x \le 6$) clusters. The E_a for the exchange of one outer metal ion (In(III) for Ga(III)) is 140 kJ/mol (33 kcal/mol). Thermodynamic

values of $\Delta G^{\ddagger}$ = 110 kJ/mol (25 kcal/mol), $\Delta H^{\ddagger}$= 140 kJ/mol (33 kcal/mol), and $\Delta S^{\ddagger}$= 0.11 kJ/mol (0.025 kcal/mol) were also calculated for this exchange. At room temperature (25°C), this reaction (**Ga_8In_5 to Ga_7In_6**) has a rate constant $k = 1.9x10^{-6} \pm 0.3x10^{-6}$ s^{-1}. The exchange of the ligands on the **Ga_{13}** cluster has a rate constant with the same order of magnitude, $k = 1.2x10^{-6}$ ($R^2 = 0.99$) s^{-1}. The similarity between the rate constants for the two types of dynamic behavior could indicate that a single mechanism is playing a shared role in the two types of exchange. The similarity could also be due to complex solvation effects that are driving many of the solution dynamics. These studies and data provide fundamental knowledge about the dynamics and reactivity of these clusters in solution, and provide a foundation for future research on this project (See Chapter VI for more future directions).

Bridge to Chapter V

The full characterization of these **$Ga_{13-x}In_x$** ($0 \leq x \leq 6$) clusters allows for prompt characterization, as well as, the ability to conduct intensive kinetic and thermodynamic studies. Chapter V presents a sample manuscript exploiting the use of this quick characterization during the preparation of precursors for thin film oxides.

CHAPTER V

APPLICATION OF ^{1}H-NMR RESULTS: ELECTROCHEMICAL SYNTHESIS OF FLAT-$[Ga_{13-x}In_x(\mu_3\text{-}OH)_6(\mu\text{-}OH)_{18}(H_2O)_{24}(NO_3)_{15}]$ CLUSTERS AS AQUEOUS PRECURSORS FOR SOLUTION-PROCESSED SEMICONDUCTORS

Contributions

The UO and CSMC provided students with an immersion course focused on conducting research with the end goal of a published manuscript. As the students worked towards their goals, they used ^{1}H-NMR as a key characterization technique and relied on my assistance and knowledge for proper deductions. The preliminary writing was done by the students in the class; however, the editing and revision process was completed by Milton N. Jackson Jr., Dr. Matthew E. Carnes, Dr. Christopher C. Knutson, Dr. Athavan Nadarajah, and Brandon M. Crockett. Prof. Shannon W. Beottcher and Prof. Darren W. Johnson were the principle investigators for this work and provided editorial assistance. This article was published 2014 in *The Journal of Materials Chemistry C* a publication of The Royal Society of Chemistry, volume 2, issue 40 pages 8492-8496.[117]

Introduction

Thin film deposition using aqueous inorganic-cluster precursors provides an alternative to traditional vacuum processing techniques for thin-film manufacture.[44,121–129] As one example, "flat" Group 13 $[M_{13}(\mu_3\text{-}OH)_6(\mu\text{-}OH)_{18}(H_2O)_{24}(NO_3)_{15}]$, homo- and heterometallic clusters (Figure 5.1) have been used to deposit high-performance semiconductor[3] and dielectric films[130]. Because of this, significant effort has been aimed

at improving Group-13 cluster synthesis. Early syntheses took two weeks and used dibutylnitrosamine (DBNA), a known carcinogen.[3,42,61] Wang *et al.* showed that the addition of Zn powder to acidic $Al(NO_3)_3$ solutions results in condensation of $[Al_{13}(\mu_3\text{-}OH)_6(\mu\text{-}OH)_{18}(H_2O)_{24}(NO_3)_{15}]$ (**Al_{13}**) clusters via a gradual pH increase of the solution through nitrate reduction. The reaction is complete in approximately two days and the carcinogenic DBNA is no longer needed.[43,131] A disadvantage to this method is that extensive purification is required to remove Zn^{2+} from the precursor solution. The preferential solubility of zinc nitrate in alcohol is used to purify the clusters, as M_{13} clusters are negligibly soluble in many organic solvents. In contrast, electrochemistry provides a direct mechanism to drive reduction reactions without the use of chemical reagents that must be later removed. Recently, both flat[132] and Keggin[133] **Al_{13}** clusters have been electrochemically synthesized.

Here we report the electrochemical synthesis of $[Ga_{13-x}In_x(\mu_3\text{-}OH)_6(\mu\text{-}OH)_{18}(H_2O)_{24}]^{15+}$ (x = 0, 4, 5) clusters and show that the aq. solutions obtained can be used, without purification, to deposit Ga-In-O channel layers with good thin-film transistor (TFT) performance. The elimination of secondary reagents and purification steps is beneficial for mass production, sustainability, and cost. Films can be cast directly from the modified salt solutions, making this a direct method for obtaining various homo- and heterometallic Group 13 oxide thin films with a variety of applications.

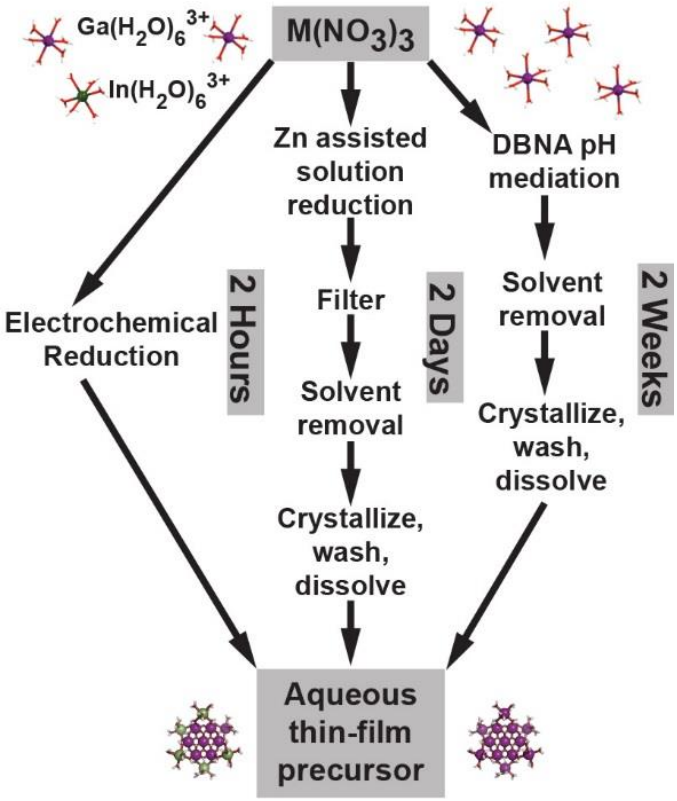

Figure 5.1. Comparison of M_{13} cluster synthesis routes.

Experimental

The synthesis is performed in a two-compartment electrochemical cell comprising 1) a beaker housing the Pt working electrode, a Ag/AgCl reference electrode, and pH probe and 2) a medium fritted tube, inside the beaker, containing a Pt counter electrode. The applied working electrode potentials were chosen to be slightly negative of the reduction potential of the metal cations at the pH of interest as described by their Pourbaix diagrams.[134] Potentials of -1.00 V vs. Ag/AgCl for Ga and -0.49 V vs. Ag/AgCl for Ga-In mixtures were used to generate the desired products with the given apparatus. The voltage of -1.00 V for aq. solutions of gallium nitrate caused a change in the luster of the Pt surface which could be seen by eye.[135] Yields of washed product show this plating results in a relatively small amount of Ga loss overall (< 2%).

Results and Discussion

The primary mechanism of this reaction appears to be the removal of nitrate from the solution via its reduction to ammonium, NO_x, and potentially other species. The removal of nitrate counter anions from the solution raises the pH of the solution by consuming protons as in (Scheme 5.1) and thus drives the formation of the cluster via LeChatelier's Principle as it acts on the reaction as given in (Scheme 5.2).

$$NO_3^- + e^- + H_3O^+ \rightarrow NO_2^- + H_2O$$

Scheme 5.1. pH raises when NO_3^- is removed electrochemically.

$$13\ M(H_2O)_6(NO_3)_3$$

$$\uparrow\downarrow$$

$$[M_{13}(\mu_3\text{-}OH)_6(\mu\text{-}OH)_{18}(H_2O)_{24}](NO_3)_{15} + 30\ H_2O + 24\ HNO_3$$

Scheme 5.2. General formation of the clusters.

Analysis of an air-dried aliquot of the crude reaction by ^{1}H-NMR shows a prominent triplet peak with equal peak heights corresponding to the ^{1}H-^{14}N coupling of ammonium ions centered at 7.1 ppm (Figure 5.2).[136] This indicates that nitrate is reduced to ammonium as a part of one pathway in which counterions are removed from solution and the pH is raised. Although the presence of ammonium ions indicates that nitrate reduction is involved in raising the pH of the cluster solution and forcing olation of the metal aqua species, it does not rule out other contributing mechanisms. We find that electrolysis at sufficiently high current results in evolution of a brown gas. This is likely due to the reduction of NO_3^- to NO_x gases.[137] We performed the electrochemical synthesis of **Ga_{13}** and **$Ga_{13-x}In_x$** mixed clusters at a constant applied voltage which was high enough to reduce small amounts of metal but low enough to prevent large losses of material to

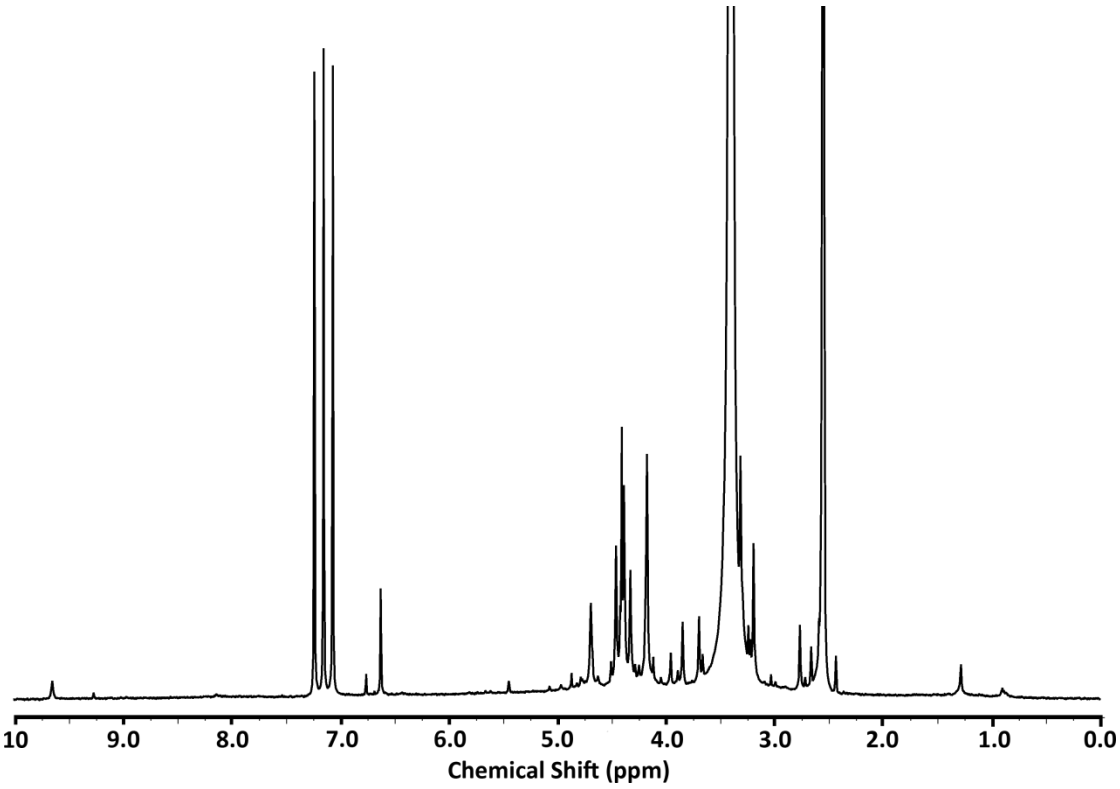

Figure 5.2. ^{1}H NMR spectrum of raw, electrochemically-synthesized Ga_{13}. Note three large peaks at values just greater than 7 ppm correspond to ammonium ion being present in the sample. The fingerprint region is between 6.5 and 6.9 ppm.

plating. We believe that some metal plating onto the electrode is important to condition the Pt toward nitrate reduction. Nitrate can undergo a number of reduction processes to form species including N_2O_4, HNO_2, NO, and NH_4^+. The standard reduction potentials are similar, between +0.8-1.0 V vs. NHE,[138] and all much more positive than the hydrogen reduction potential. At a clean Pt electrode, however, H_2 generation might be expected to dominate given the fast kinetics relative to nitrate reduction. We did not observe significant bubbles (that would be associated with H_2 formation) on the Pt electrode surface. After Pt is modified by Ga/In plating it likely becomes poisoned for hydrogen evolution and thus kinetically preferences the nitrate reduction reaction.[139] These data support the hypothesis that nitrate reduction is the predominate electrochemical reaction.

Regardless of the cathode reaction, charge balance requires additional positively charged species (e.g. $In(H_2O)_6^{3+}$ or $Ga(H_2O)_6^{3+}$) to migrate from the counter electrode compartment into the working electrode compartment or negatively charged species (e.g. NO_3^-) to migrate the opposite direction. Both migration processes serve to lower the nitrate-to-metal-ion ratio in the working-electrode-compartment film-precursor solution.

Proton NMR provides useful information for the identification and determination of the degree of substitution by indium in heterometallic clusters. Analysis of aq. inorganic clusters by ^{1}H-NMR spectroscopy is traditionally challenging in protic solvents, however, due to acidic proton exchange with the solvent. In most aprotic solvents, analysis of inorganic clusters by ^{1}H-NMR spectroscopy is made difficult by the low solubility of highly-charged clusters. These obstacles are overcome by using d_6-DMSO, which allows for the detection of signals arising from water molecules and hydroxide bridges of the cluster. To confirm the presence of clusters, a portion of the electrochemically generated samples was air dried and then dissolved in d_6-DMSO. These samples were allowed to equilibrate overnight to ensure even DMSO exchange at the outer hydroxyl shell of the clusters. The ^{1}H-NMR spectra of the reduced $Ga(NO_3)_3$ product is consistent with that of flat-**Ga_{13}** clusters previously reported (Figure 5.2).[19]

Using ^{1}H-NMR, we are able to distinguish between differently substituted heterometallic clusters once they have been dried and isolated. After equilibrating in d_6-DMSO for 24 hr the clusters for each Ga:In ratio gives rise to a distinctive spectrum with a clearly developed fingerprint region (Figure 5.3). Although we can identify the Ga:In ratio from this signature, we are still unable to distinguish between positional isomers of the In at the exterior of the clusters. Crystals were grown of each of the isomers

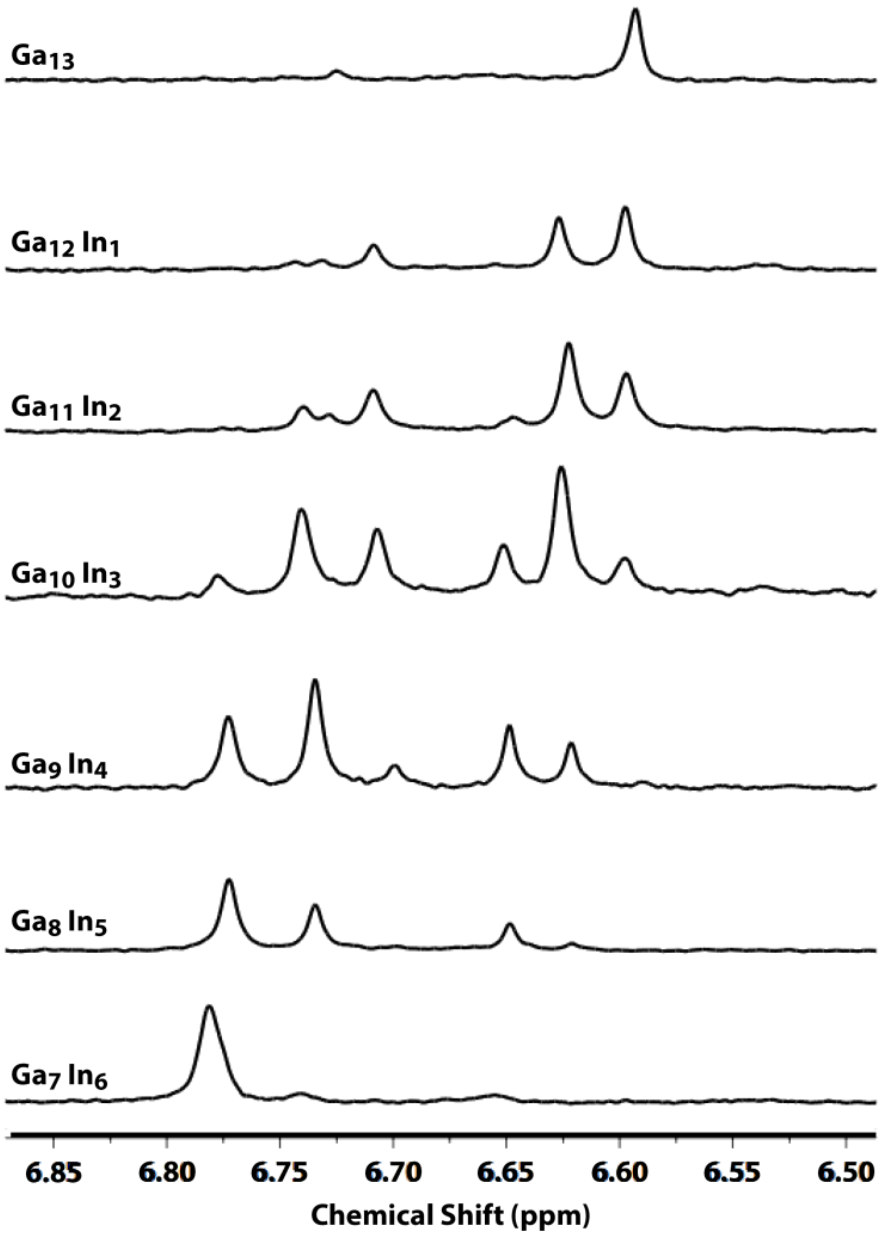

Figure 5.3. ^{1}H-NMR fingerprint region of the $Ga_{13-x}In_x$ clusters. Samples were synthesized by the DBNA and Zn-reduction method, and illustrate the definitive characteristics of each substitution.

independently and their spectra taken to calibrate our results.[62] The ^{1}H-NMR spectra obtained for the product of the mixed metal nitrate reduction, starting with a 6:7 ratio of Ga to In, is consistent with the **Ga_9In_4** cluster synthesized independently (Figure 5.3).

After washing the product of the electrochemical reaction with isopropanol, this product appears to have exchanged some of the external metal ions to form **Ga_8In_5** clusters as is evident by the change in their distinctive ^{1}H-NMR spectra. This suggests that the clusters may be dynamic in the presence of the washing solvent and that In readily substitutes for Ga within the cluster (Figure 5.4). Exchange of In atoms around flat M_{13} has recently been observed in solution to be a reversible, equilibrium process.[62]

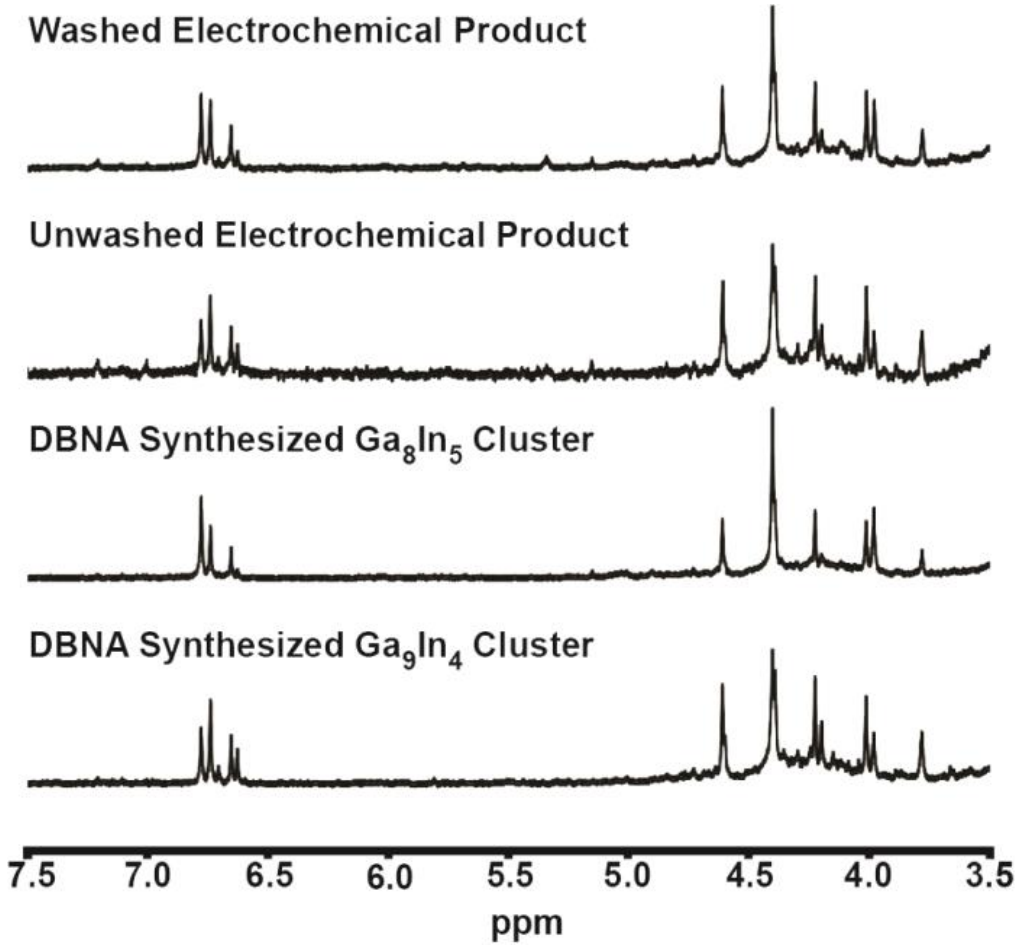

Figure 5.4. ^{1}H-NMR characterization of heterometallic electrochemical products. ^{1}H-NMR (d_6-DMSO) spectra of washed and unwashed precipitated cluster products from DBNA and electrochemical syntheses. Based on comparison to the DBNA-derived control samples, the unwashed electrochemical product is assigned the composition Ga_9In_4, while the washed electrochemical product is assigned the composition Ga_8In_5.

We find evidence for M_{13} species forming with fewer reducing equivalents than that reported for the Zn-based synthesis of $[Al_{13}(\mu_3\text{-}OH)_6(\mu\text{-}OH)_{18}(H_2O)_{24}(NO_3)_{15}]$.[43] **$Ga_{13}$** clusters are observed after passing a cathodic charge of 0.7-0.8 electrons per Ga, and 0.4-0.5 electrons per metal in the case of the $Ga_{13-x}In_x$ clusters. The Zn-based synthesis of **Al_{13}** used 1.0 reducing equivalents per Al (1:2 Zn:Al as Zn is a $2e^-$ reductant). The synthesis of a related Sc_2 cluster used 0.75 reducing equivalents per Sc.[131] Our hypothesis to explain such behavior is that if hydroxyl-bridged metal cluster formation is under equilibrium control, not all of the excess nitrate counterions need to be consumed for clusters to form. Our analysis does not however exclude the possibility that the reaction does not go to completion under the conditions used. Nitrate ions can also be effectively removed from association with the growing clusters by counterbalancing the positive charge associated with newly formed ammonium ions, leaving this new ammonium nitrate salt in solution but allowing ions to diffuse away from clustering species.

Raman spectroscopy has also been shown to be a useful technique for identifying M_{13} clusters.[22] The Raman spectra of aliquots from the electrochemical synthesis agree with previous reports of **Ga_{13}** clusters, highlighted by the v_1 Ga-O symmetric stretch, or breathing mode at 464 ± 1 cm^{-1} (Figure 5.5).[22] The Raman spectra of the structurally analogous $Ga_{13-x}In_x$ cluster reveal similar vibrational features to those observed in **Ga_{13}** clusters, with the v_1 breathing mode slightly red-shifted to 449 ± 1 cm^{-1}. This shift is consistent with the substitution of the larger In for Ga, and with the observed difference between the vibrational modes of In and Ga hexa-aqua salts (Figure 5.5).

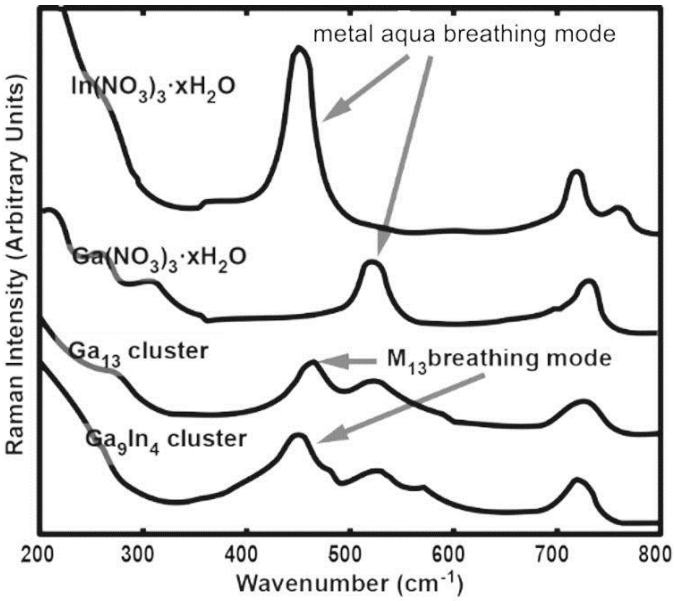

Figure 5.5. Solid-state Raman spectra of nitrate salts and electrochemically generated cluster samples. Spectra for cluster compounds were collected on a single crystal using a Raman microscope and are largely free of metal nitrate impurities. Note the red-shift in the v_1 breathing mode center for the In-substituted cluster (449 ± 1 cm^{-1}) when compared to that for the Ga cluster (464 ± 1 cm^{-1}). The uncertainties given are associated with the error in fitting the peak center.

The class of flat M_{13} Group 13 clusters prepared previously have been shown to be effective precursors for high-quality thin films.[3,130] In this study, aq. cluster-containing solutions with an In:Ga ratio of 6:7 produced by the electrochemical synthesis were directly spin-cast onto thermally grown SiO_2 on Si wafers and annealed at 550 °C. This process circumvents the recrystallization step and the need to wash and dissolve the solid products in another solvent, thus reducing the time and solvent needed for synthesis. Heterometallic clusters were used to generate channel layers within TFTs. A TEM image of a device cross-section confirms the uniform morphology of thin films processed from the electrochemically-synthesized precursor (Figure 5.6a). EDX measurements of the films (Figure 5.7) confirmed the presence of both In and Ga in the films.

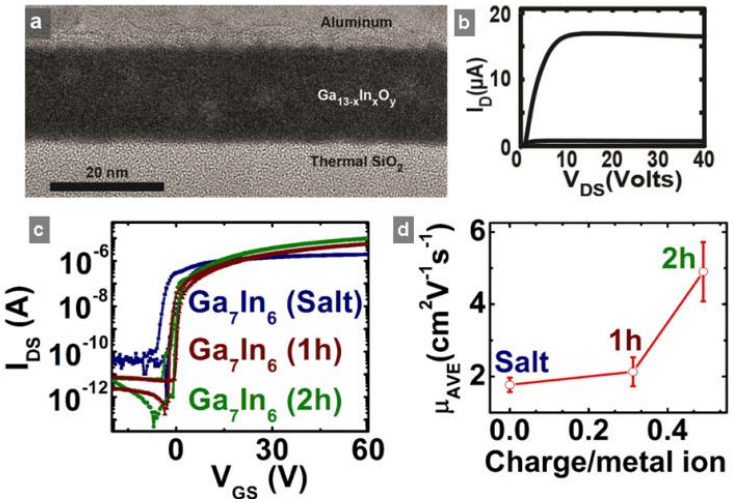

Figure 5.6. Overview of a thin film device produced from the electrochemical clusters. (a) Transmission electron microscopy image demonstrating the uniform morphology of thin films processed from the electrochemically-synthesized precursor. (b) Average transfer curve compiled from five bottom-gate TFTs processed using the electrochemically synthesized $\mathbf{Ga_{13-x}In_x}$ heterometallic clusters to generate channel layers. (c) Representative transfer plots for 550 ˚C air-annealed In-Ga-O films created using the electrochemically synthesized $\mathbf{Ga_{13-x}In_x}$ heterometallic cluster and starting salt solution precursors. (d) Average channel mobility determined at V_{GS} = 40 V for films made at various electrolyzed time intervals (and thus different average numbers of electrons passed into the solution per metal ion). Device performance is increased with longer electrolysis, consistent with removal of nitrate and formation of clusters. The devices consist of the following structures: Al/Si (p+)/SiO_2(100 nm)/In-Ga-O(15 nm)/Al, length = 150 μm, width = 1000 μm, and V_{DS} = 0.1 V (V_{DS} = drain source voltage; V_{GS} = gate source voltage; I_D = drain current).

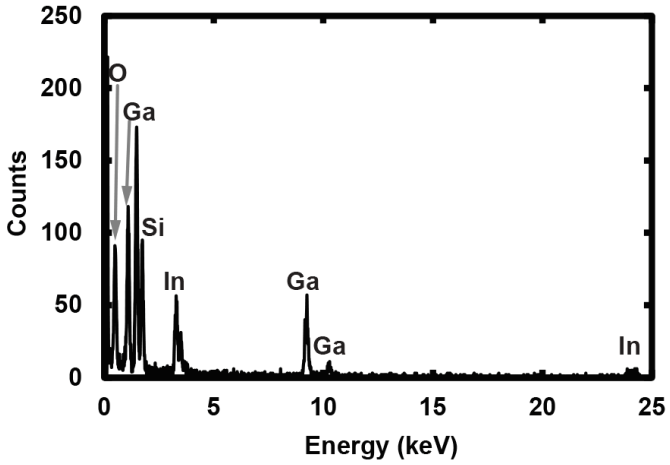

Figure 5.7. Energy dispersive x-ray (EDX) spectroscopy measurements of the film presented in Figure 5.4a confirming the presence of Ga, In and O in the final material.

Figures 5.6b, c, and d show the device properties of the heterometallic cluster channel layer in TFTs processed from the electrochemically generated cluster solutions and compares them to those made using a starting nitrate salt solution. The devices derived from electrochemically-synthesized precursors are comparable to previously reported devices using DBNA-derived precursors.[3] Devices obtained from cluster precursors show on-to-off current ratios of greater than 10^6 and turn-on voltages near -2 V whereas the devices made from starting salt solution show slightly negative turn-on voltages of ~ -3 V and on-to-off ratios greater than 10^5 (Figure 5.6c).

The average channel mobility of cluster films are greater than those obtained from starting salt solution films by at least a factor of two (Figure 5.6d). These values for mobility were calculated by the method of Wager *et al.*[140] Compared to the mixed salt solutions of $In(NO_3)_3$ and $Ga(NO_3)_3$, the $\mathbf{Ga_{13-x}In_x}$ clusters have fewer nitrate counter ions per active metal because the nitrates are consumed electrochemically during the cluster synthesis. This decrease in nitrate concentration drives olation and preorganization of the metal hydroxides into clusters.[141] Because nitrates are removed during the annealing step to give an oxide thin film, we attribute the enhanced performance of the electrolyzed solution to reduced porosity in the final semiconductor channel that would be caused by decomposing counter ions.

Although the goal of this work is to show the new electrochemical synthesis route yields cluster precursors whose TFT performance is similar to clusters made by conventional methods, it is also useful to compare the performance to other solution-derived oxide thin films. Kim *et al.* reported the use of "combustion processing" to deposit related In-Zn-O films at temperatures as low as 200°C from methoxyethanol

solutions.[142] Composition-optimized $In_{0.7}Zn_{0.3}O_{1.35}$ devices fabricated with a SiO_2 gate dielectric (as is done here) had saturation mobilities (μ_{sat}) of 10 $cm^2\ V^{-1}\ s^{-1}$ after annealing at 400°C. Hwang et. al. reported μ_{sat} of 8 $cm^2\ V^{-1}\ s^{-1}$ for $In_{0.7}Zn_{0.3}O_{1.35}$ after annealing at 300°C when $Zn(NO_3)_2$ and $In(NO_3)_3$ were deposited from an aqueous solution.[143] The $In_{0.46}Ga_{0.53}O_{1.5}$ studied here had average channel mobilities of 5 $cm^2\ V^{-1}s^{-1}$. Studies of vapor-deposited films show that mobility increases sharply with higher In concentration.[144] Increasing the In:Ga ratio in the clusters would be expected to further increase TFT performance. Alternative gate dielectrics (e.g. amorphous alumina),[142] and surface/interface passivation layers,[145,146] also dramatically improve the TFT performance of films made from other solution precursors. These strategies can directly be used to improve the performance of the cluster precursors reported here.

Conclusion

In summary, an alternate synthetic method is reported for the synthesis of flat homo- and heterometallic Group 13 cluster precursor solutions that can be directly used in the fabrication of thin-film transistors. This new method reduces the processing time to generate M_{13} cluster solutions from two days to two hours. The synthesis is carried out electrochemically so as to reduce protons and nitrate ions in a controlled fashion. Heterometallic clusters synthesized using this method are functionally similar in transistor applications to previously synthesized and characterized clusters.[3] These films are capable of being spin-cast directly from unpurified reaction solutions into high-quality thin films. The films are dense, smooth, and processable at relatively moderate temperatures under ambient atmospheric conditions. This reagent-free, electrochemical

synthesis may also find application in future mechanistic studies of cluster formation and speciation.

Bridge to Chapter VI

By developing a method to quickly characterize the $\mathbf{Ga_{13-x}In_x}$ clusters in solution, I have opened up an entire area of study that was preciously inaccessible. Early attempts to exchange counterions were met with frustration due to the lack of known options for solution characterization. In the final chapter of this thesis, I will elaborate on the potential fundamental behavior and understanding of these, and similar, inorganic nanoscale clusters that this research can assist.

CHAPTER VI

FUTURE WORK AND CONCLUSIONS

Future Work

In addition to the experiments listed in Chapter IV, the aforementioned progress involving the analysis of inorganic nanoscale clusters in solution, has set the stage for an entire group of experiments which can provide fundamental and advanced knowledge about these elusive species. Early on, I attempted to preform counterion exchange on the **Ga_{13}** cluster. My goal was to incorporate an additional metal into the thin film precursor via the counterions; however, the lack of characterization techniques available for solution analysis left me trying to crystallize products from every experiment. Even proof of concept experiments produced numerous aliquots, rarely leading to quality crystals. Eventually I attempted to use index of refraction to identify aliquots of interest, but conclusive data was never acquired. This is just one of many projects that can now be successfully continued with the new power of ^{1}H-NMR and DOSY analysis.

Anion Exchange

Initial anion exchange experiments were put on hold until proper characterization was available. As stated in Chapter III, the chemical shift of protons in these **$Ga_{13-x}In_x$** clusters is extremely depended upon counterion location and type; therefore, a lot of information can be obtained about counterion exchange using ^{1}H-NMR. Thus far, every ^{1}H-NMR of a **$Ga_{13-x}In_x$** cluster has had NO_3^- counterions present. Figure 6.1 shows the impact on the chemical shift of "mother cluster" protons $H_{\mathrm{Ga}\mathbf{Ga}\mathrm{Ga}}^{\mu_{2}\mathrm{int}}$ and $H_{\mathbf{Ga}\mathrm{Ga}}^{\mu_{2}\mathrm{ext}}$ when I^- is introduced to the **Ga_{13}** cluster. A combination of quantum mechanical computations and

an analysis of change in chemical shift (Δδ) could lead to "daughter cluster" peak assignments. It is possible that all μ_2-OH_{int} interact with counterions to a similar extent; and therefore, produce a similar Δδ to $H^{\mu_{2int}}_{\mathbf{GaGa}Ga}$. Similar chemical shifts have been seen by Susan R. Cooper for the addition of other counterions as well.

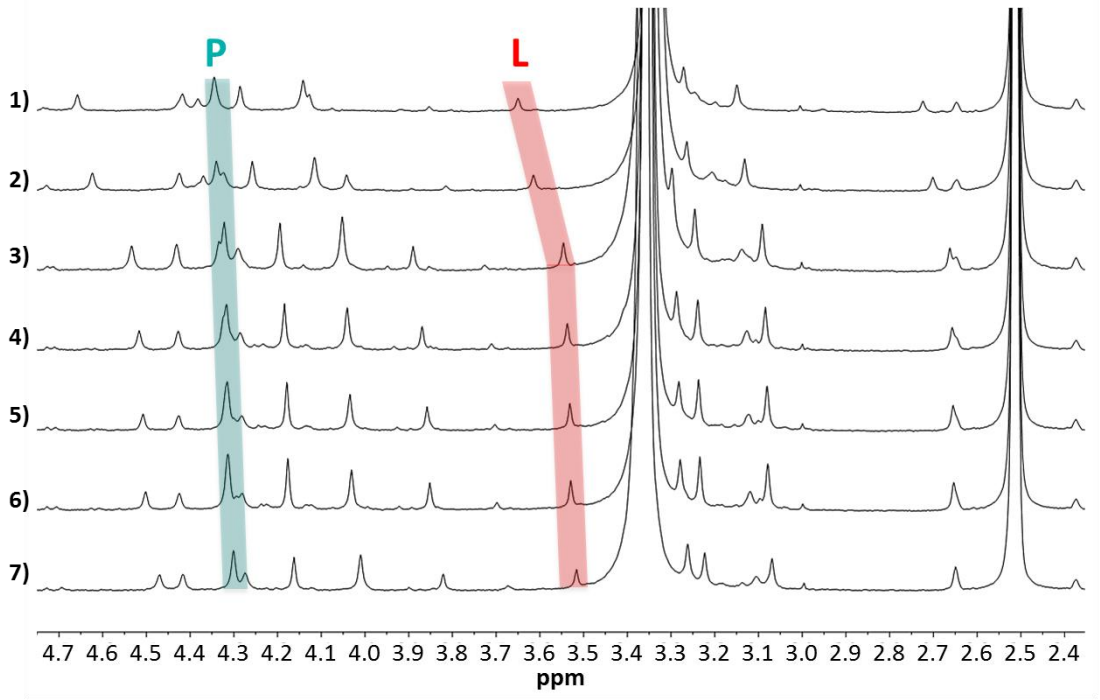

Figure 6.1. Addition of NaI to a 2 mM Ga_{13} in d_6-DMSO sample. Red: $H^{\mu_{2int}}_{\mathbf{GaGa}Ga}$ (L). Teal: $H^{\mu_{2ext}}_{\mathbf{GaGa}}$ (P). NaI added: 1) 0 equiv., 2) 1 equiv., 3) 7 equiv., 4) 8 equiv., 5) 9 equiv., 6) 10 equiv., and 7) 14 equiv.

Keggin-Ga_{13}

The **Ga_{13}** cluster is occasionally referred to as flat-**Ga_{13}**, as not to be confused with the legendary, yet elusive, $[GaO_4Ga_{12}(OH)_{24}(H_2O)_{12}]^{7+}$ (**Keggin-Ga_{13}**).[147,148] There are a limited number of reports characterizing the Keggin-Ga_{13}, and to date zero that have crystallized this illustrious species. In contrast, the aluminum equivalent (**Keggin-Al_{13}**) has been studied in great detail (Table 3.2). When **Keggin-Al_{13}** is observed using ^{1}H-NMR 3 signals are visible in 1:1:2 ratios. These correspond to the 2 types of μ_2-OH

bridges and the outer water ligands, respectively. The **Keggin-Al_{13}** has been studied with a variety of cournerions including Cl^-, NO_3^-, SO_4^{2-}, and SeO_4^{2-}.[118,148,149] When SO_4^{2-} and SeO_4^{2-} are added to solutions of the **Ga_{13}** cluster the number of peaks reduces to 2 or 3 (Figure 6.2). This is promising evidence that **Keggin-Ga_{13}** is forming in the presence of these anions. These results were obtained and are going to be continued by Susan R. Cooper.

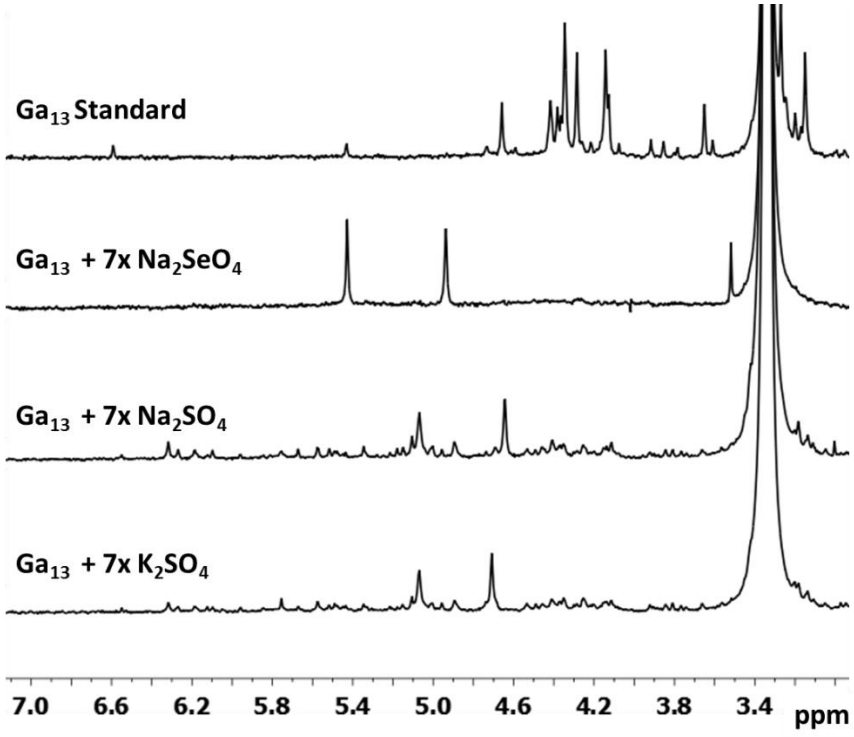

Figure 6.2. Addition of SO_4^{2-} and SeO_4^{2-} salts to a 2 mM Ga_{13} in d_6-DMSO sample.

Geochemistry and Clusters

I believe that clusters are much more prominent in nature than expected. On multiple occasions clusters have been shown to exist in natural settings.[118,119] Clusters tend to form in relatively acid conditions (pH = 2-4). It has recently been shown by Brantly Fulton, that the **Al_{13}** cluster can be synthesized by adding HNO_3 to basic $Al(OH)_3$. This has immense impacts in geochemistry. Aluminum ores (bauxites: gibbsite

$Al(OH)_3$ and boehmite AlO(OH)) in the presence of acid rain could be naturally synthesizing $\mathbf{Al_{13}}$ cluster. Acid rain, acid mine drainage, and geothermal vents are all acid environments. By taking samples and studying them via ^{1}H-NMR, geochemists could discover an entire step to the corrosion process that was previously ignored.

Discovery of New Clusters and Assignment of Peaks

^{1}H-NMR and DOSY will revolutionize the field of novel cluster synthesis. Instead of traditional "crystal fishing" for new inorganic species, solutions can be screened for promising results in a timely manner. While single crystal analysis will always be interesting and essential, the screening by ^{1}H-NMR can limit the number of samples characterized using this more time intensive technique. In addition to promoting the discovery of new species, this research can be used as a reference for assigning signals. The review in Chapter III can help future researchers to assign spectral signals to protons in known and forthcoming molecules with hydroxide bridges in their structures.

Conclusion

In conclusion, I was able to apply a set of corroborative and collaborative characterization techniques to analyze inorganic nanoscale clusters. Using ^{1}H-NMR, SAXS and DOSY, I was able to determine the presence and stability of $\mathbf{Ga_{13}}$ in d_6-DMSO solution. I then went on the characterize all of the $\mathbf{Ga_{13-x}In_x}$ clusters using this combination of techniques. By collaborating with researchers at OSU, we were able to assign all of the "mother clusters" protons to signals in the ^{1}H-NMR spectra. These peak assignments then clarified the dynamic behavior of these clusters in solution. ^{1}H-NMR has become a quick screening technique for cluster synthesis and has the potential to impact many future research projects. It is my hope that this research can pave the way

for new, exciting, relevant research in the fields of inorganic, materials, and geochemistry.

REFERENCES CITED

(1) Oliveri, A. F.; Elliott, E. W.; Carnes, M. E.; Hutchison, J. E.; Johnson, D. W. *ChemPhysChem* **2013**, *14*, 2655–2661.

(2) Silverstein, R.; Webster, F.; Kiemle, D. *Spectrometric Identification of Organic Compounds*; Seventh.; John Wiley & Sons, Inc: State University of New York, 2005.

(3) Mensinger, Z. L.; Gatlin, J. T.; Meyers, S. T.; Zakharov, L. N.; Keszler, D. A.; Johnson, D. W. *Angew. Chem. Int. Ed.* **2008**, *47*, 9484–9486.

(4) Heo, J.; Kim, J.; Choi, S.; Park, K. S.; Kim, C. D.; Hwang, Y. K.; Chung, I. J.; Meyers, S. T.; Anderson, J. T.; Clark, B. C.; Greer, M.; Jiang, K.; Grendille, A.; Keszler, D. A. *SID 10 Dig.* **2010**, *41*, 241–244.

(5) Von der Kammer, F.; Ferguson, P. L.; Holden, P. A.; Masion, A.; Rogers, K. R.; Klaine, S. J.; Koelmans, A. A.; Horne, N.; Unrine, J. M. *Environ. Toxicol. Chem.* **2012**, *31*, 32–49.

(6) Polte, J.; Erler, R.; Thünemann, A. F.; Sokolov, S.; Ahner, T. T.; Rademann, K.; Emmerling, F.; Kraehnert, R. *ACS Nano* **2010**, *4*, 1076–1082.

(7) Richman, E.; Hutchison, J. *ACS Nano* **2009**, *3*, 2441–2446.

(8) McKenzie, L. C.; Haben, P. M.; Kevan, S. D.; Hutchison, J. E. *J. Phys. Chem. C* **2010**, *114*, 22055–22063.

(9) Glatter, O.; Kratky, O. *Small Angle X-ray Scattering*; Academic Press: London, 1982; pp. 3–51.

(10) Pedersen, J. S. *Adv. Colloid Interface Sci.* **1997**, *70*, 171–210.

(11) Schwedt, G. *The Essential Guide to Analytical Chemistry*; John Wiley & Sons, Inc: Chichester, 1997; pp. 1–248.

(12) Claridge, T. D. W. *High-Resolution NMR Techniques in Organic Chemistry*; Second.; Elsevier: Oxford, 2009; pp. 303–334.

(13) Johnson Jr., C. S. *Prog. Nucl. Magn. Reson. Spectrosc.* **1999**, *34*, 203–256.

(14) Long, D.-L.; Tsunashima, R.; Cronin, L. *Angew. Chem. Int. Ed.* **2010**, *49*, 1736–1758.

(15) Ohlin, C. A. *Chem. Asian J.* **2012**, *7*, 262–270.

(16) Wyatt, P. J. *Anal. Chim. Acta* **1993**, *272*, 1–40.

(17) Tantra, R.; Schulze, P.; Quincey, P. *Particulology* **2010**, *8*, 279–285.

(18) Liu, X.; Atwater, M.; Wang, J.; Huo, Q. *Colloid. Surf. B* **2007**, *58*, 3–7.

(19) Oliveri, A. F.; Carnes, M. E.; Baseman, M. M.; Richman, E. K.; Hutchison, J. E.; Johnson, D. W. *Angew. Chem. Int. Ed.* **2012**, *51*, 10992–10996.

(20) M. D. Pluth, B. E. F. Tiedemann, H. van Halbeek, R. Nunlist, K. N. R. *Inorg. Chem.* **2008**, *47*.

(21) Longsworth, L. G. *J. Phys. Chem.* **1954**, *58*, 770.

(22) Jackson, M. N.; Wills, L. A.; Chang, I.-Y.; Carnes, M. E.; Scatena, L. F.; Cheong, P. H.-Y.; Johnson, D. W. *Inorg. Chem.* **2013**, *52*, 6187–6192.

(23) Canzi, G.; Mrse, A. A.; Kubiak, C. P. *J. Phys. Chem. C* **2011**, *115*, 7972–7978.

(24) Terrill, R.; Postlethwaite, T. *J. Am. Chem. Soc.* **1995**, *117*, 12537–12548.

(25) Elliott, E. W.; Oliveri, A. F.; Zaikova, T.; McKenzie, L.; Johnson, D. W.; Hutchison, J. E. Manuscript in Progress.

(26) Qiu, J.; Ling, J.; Sui, A.; Szymanowski, J. E. S.; Simonetti, A.; Burns, P. C. *J. Am. Chem. Soc.* **2012**, *134*, 1810–1816.

(27) Ling, J.; Wallace, C. M.; Szymanowski, J. E. S.; Burns, P. C. *Angew. Chem. Int. Ed.* **2010**, *49*, 7271–7273.

(28) Sigmon, G. E.; Ling, J.; Unruh, D. K.; Moore-Shay, L.; Ward, M.; Weaver, B.; Burns, P. C. *J. Am. Chem. Soc.* **2009**, *131*, 16648–16649.

(29) Ling, J.; Qiu, J.; Sigmon, G. E.; Ward, M.; Szymanowski, J. E. S.; Burns, P. C. *J. Am. Chem. Soc.* **2010**, *132*, 13395–13402.

(30) Johnson, R. L.; Ohlin, C. A.; Pellegrini, K.; Burns, P. C.; Casey, W. H. *Angew. Chem. Int. Ed.* **2013**, *52*, 7464–7467.

(31) Alivisatos, P.; Barbara, P. F.; Castleman, A. W.; Chang, J.; Dixon, D. A.; Klein, M. L.; McLendon, G. L.; Miller, J. S.; Ratner, M. A.; Rossky, P. J.; Stupp, S. I.; Thompson, M. E. *Adv. Mater.* **1998**, *10*, 1297–1336.

(32) Anderson, T. M.; Neiwert, W. A.; Kirk, M. L.; Piccoli, P. M. B.; Schultz, J.; Koetzle, T. F.; Musaev, D. G.; Morokuma, K.; Cao, R.; Hill, C. L. *Science* **2011**, *306*, 2074–2077.

(33) Yin, Q.; Tan, J. M.; Besson, C.; Geletii, Y. V; Musaev, D. G.; Kuznetsov, A. E.; Luo, Z.; Hardcastle, K. I.; Hill, C. L. *Science* **2010**, *328*, 342–345.

(34) Kanan, M. W.; Nocera, D. G. *Science* **2008**, *321*, 1072–1075.

(35) Karunadasa, H. I.; Chang, C. J.; Long, J. R. *Nature* **2010**, *464*, 1329–1333.

(36) McAlpin, J. G.; Surendranath, Y.; Dinca, M.; Stich, T. A.; Stoian, S. A.; Casey, W. H.; Nocera, D. G.; Britt, R. D. *J. Am. Chem. Soc.* **2010**, *132*, 6882–6883.

(37) Stamatatos, T. C.; Teat, S. J.; Wernsdorfer, W.; Christou, G. *Angew. Chem. Int. Ed.* **2009**, *48*, 521–524.

(38) Hill, S.; Edwards, R. S.; Aliaga-Alcalde, N.; Christou, G. *Science* **2003**, *302*, 1015–1018.

(39) Schneider, S.; Dzudza, A.; Raudaschl-Sieber, G.; Marks, T. J. *J. Chem. Mater.* **2007**, *19*, 2768–2779.

(40) Casey, W. H. *Chem. Rev.* **2006**, *106*, 1–16.

(41) Rather, E.; Gatlin, J. T.; Nixon, P. G.; Tsukamoto, T.; Kravtsov, V.; Johnson, D. W. *J. Am. Chem. Soc.* **2005**, *127*, 3242–3243.

(42) Gatlin, J. T.; Mensinger, Z. L.; Zakharov, L. N.; Macinnes, D.; Johnson, D. W. *Inorg. Chem.* **2008**, *47*, 1267–1269.

(43) Wang, W.; Wentz, K. M.; Hayes, S. E.; Johnson, D. W.; Keszler, D. A. *Inorg. Chem.* **2011**, *50*, 4683–4685.

(44) Jiang, K.; Anderson, J. T.; Hoshino, K.; Li, D.; Wager, J. F.; Keszler, D. A. *Chem. Mater.* **2011**, *23*, 945–952.

(45) Greaves, G. N.; Sen, S. *Adv. Phys.* **2007**, *56*, 1–166.

(46) Gilbert, B.; Lu, G.; Kim, C. S. *J. Colloid Interf. Sci.* **2007**, *313*, 152–159.

(47) C. P. Pradeep, F.-Y. Li, C. Lydon, H. N. Miras, D.-L. Long, L. Xu, L. C. *Chem. Euro. J.* **2011**, *17*, 7472–7479.

(48) Potton, J. A.; Daniell, G. J.; Rainford, B. D. *J. Appl. Cryst.* **1988**, *21*, 663–668.

(49) Ilacsky, J.; Jemian, P. R. *J. App. Cryst.* **2009**, *42*, 347–353.

(50) Akitt, J. W.; Elders, J. M. *J. Chem. Soc. Dalt.* **1988**, 1347–1355.

(51) Jackson, W. G.; McKeon, J. A.; Zehnder, M.; Neuberger, M.; Fallab, S. *Chem. Commun.* **2004**, *6*, 2322–2323.

(52) M. Åberg, J. G. *Inorg. Chim. Acta* **1993**, *206*, 53–61.

(53) Lemonnier, J.-F.; Duval, S.; Floquet, S.; Cadot, E. *Isr. J. Chem.* **2011**, *51*, 290–302.

(54) Périneau, F.; Pensec, S.; Sassoye, C.; Ribot, F.; van Lokeren, L.; Willem, R.; Bouteiller, L.; Sanchez, C.; Rozes, L. *J. Mater. Chem.* **2011**, *21*, 4470–4475.

(55) Cabrita, E. J.; Berger, S. *Mag. Reson. Chem.* **2002**, *40*, S122–S127.

(56) Sebastiãoa, R. C. O.; Pachecob, C. N.; Bragaa, J. P.; Piló-Velosoa, D. J. *Mag. Res.* **2006**, *182*, 22–28.

(57) Zielinski, M. E.; Morris, K. F. *Magn. Reson. Chem.* **2009**, *47*, 53–56.

(58) Kamunde-Devonish, M. K.; Fast, D. B.; Mensinger, Z. L.; Gatlin, J. T.; Zakharov, L. N.; Dolgos, M. R.; Johnson, D. W. *Inorg. Chem.* **2014**, Manuscript in Preparation.

(59) Oliveri, A. F.; Wills, L. A.; Hazlett, C. R.; Carnes, M. E.; Cheong, P. H.-Y.; Johnson, D. W. *J. Am. Chem. Soc.* Submitted.

(60) R. J. Abraham, J. Fisher, P. L. *Introduction to NMR Spectroscopy*; John Wiley & Sons Ltd: New York, 1988.

(61) Mensinger, Z. L.; Wang, W.; Keszler, D. A.; Johnson, D. W. *Chem. Soc. Rev.* **2012**, *41*, 1019–1030.

(62) Kamunde-Devonish, M. K.; Jackson, M. N.; Mensinger, Z. L.; Zakharov, L. N.; Johnson, D. W. *Inorg. Chem.* **2014**, *53*, 7101–7105.

(63) Akitt, J. W.; Elders, J. E.; Fontaine, X. L. R.; Kundu, A. K. *J. Chem. Soc. Dalt.* **1989**, 1889–1895.

(64) Fratiello, B. Y. A.; Lee, R. E.; Schuster, R. E. *Inorg. Chem.* **1969**, 82–85.

(65) Read, M. C.; Glaser, J.; Sandstrom, M.; Toth, I. *Inorg. Chem.* **1992**, *31*, 4155–4159.

(66) Fratiello, A.; Peak, S.; Schuster, R.; Davis, D. *J. Phys. Chem.* **1970**, *74*, 3730–3734.

(67) Houston, J. R.; Phillips, B. L.; Casey, W. H. *Geochim. Cosmochim. Ac.* **2006**, *70*, 1636–1643.

(68) Schweinfurth, D.; Klein, J.; Hohloch, S.; Dechert, S.; Demeshko, S.; Meyer, F.; Sarkar, B. *Dalt. T.* **2013**, *42*, 6944–6952.

(69) Bernal, I.; Cetrullo, J.; Berhane, S. *J. Coord. Chem.* **2000**, *52*, 185–205.

(70) Juranic, N.; Macura, S. *Inorg. Chim. Acta* **2000**, *298*, 103–106.

(71) Angus, P.; Fairlie, D.; Gunasingam, R.; Tao, Z.; Jackson, W. G. *Inorg. Chim. Acta* **1993**, *209*, 123–127.

(72) Carlson-Day, K. M.; Eglin, J. L.; Smith, L. T.; Staples, R. J. *Inorg. Chem.* **1999**, *38*, 2216–2220.

(73) Papaefstathiou, G. S.; Sofetis, A.; Raptopoulou, C. P.; Terzis, A.; Spyroulias, G.; Zafiropoulos, T. F. *J. Mol. Struct.* **2007**, *837*, 5–14.

(74) Hodge, P.; Piggott, B. *Chem. Commun.* **1998**, *4*, 1933–1934.

(75) Ogo, S.; Makihara, N.; Watanabe, Y. *Organometallics* **1999**, *18*, 5470–5474.

(76) Akitt, J. W.; Duncan, H. R. *J. Chem. Soc. Farad. T. I* **1980**, *76*, 2212–2220.

(77) Tossell, J. a. *J. Mag. Res.* **1998**, *135*, 203–207.

(78) Teng, W.; Guino-o, M.; Hitzbleck, J.; Englich, U.; Ruhlandt-Senge, K. *Inorg. Chem.* **2006**, *45*, 9531–9539.

(79) Cotton, F. A.; Daniels, L. M.; Jordan, G. T.; Lin, C.; Murillo, C. A. *Inorg. Chem. Commun.* **1998**, *1*, 109–110.

(80) Rosendorfer, P.; Beck, W. *Chem. Ber.* **1995**, *128*, 729–734.

(81) Cook, J.; Hamilin, J.; Nutton, A.; Maitlis, P. M. *J. Chem. Soc. Dalt.* **1981**, 2342–2352.

(82) Dostál, L.; Taraba, J.; Jambor, R. *J. Organomet. Chem.* **2009**, *694*, 1251–1253.

(83) Zhang, R.; Zhang, Q.; Shi, Y.; Ma, C. *J. Organomet. Chem.* **2006**, *691*, 1668–1672.

(84) Ma, C.; Li, J.; Zhang, R.; Qiu, L. *J. Mol. Struct.* **2007**, *830*, 1–7.

(85) Asato, E.; Furutachi, H.; Kawahashib, T.; Mikuriyab, M. *J. Chem. Soc. Dalt.* **1995**, 3897–3904.

(86) Tarushi, A.; Kastanias, F.; Psycharis, V.; Raptopoulou, C. P.; Psomas, G.; Kessissoglou, D. P. *Inorg. Chem.* **2012**, *51*, 7460–7462.

(87) Walther, D.; Ritter, B.; Gorls, H.; Zahn, G. *Z. Anorg. Allg. Chem.* **1997**, *623*, 1125–1130.

(88) Zhang, R.; Li, C.; Wang, Q.; Chunlin, M. *Struct. Chem.* **2010**, *21*, 745–753.

(89) Reger, D. L.; Pascui, A. E.; Pellechia, P. J.; Smith, M. D. *Inorg. Chem.* **2013**, *52*, 11638–11649.

(90) Wehmschulte, R. J.; Steele, J. M.; Khan, M. A. *Organometallics* **2003**, *22*, 4678–4684.

(91) Stender, M.; Power, P. P. *Polyhedron* **2002**, *21*, 525–529.

(92) Canal, J. P.; Jennings, M.; Yap, G. P. A.; Pomeroy, R. K. *Dalt. T.* **2008**, *4*, 1375–1382.

(93) Abedin, S. M. T.; Azam, K. A.; Hursthouse, M. B.; Kabir, S. E.; Malik, K. M. A.; Miah, R.; Vahrenkamp, H. *J. Organomet. Chem.* **1998**, *564*, 133–141.

(94) Ruiz, J.; Vicente, C.; Marti, J.; Cutillas, N.; Garcia, G.; Lopez, G. *J. Organomet. Chem.* **1993**, *460*, 241–248.

(95) Lopez, G.; Ruiz, J.; Garcia, G.; Vicente, C.; Casab, J.; Molins, E.; Miravitlles, C. *Inorg. Chem.* **1991**, *30*, 2605–2610.

(96) Sanchez, G.; Serrano, J.; Garcia, J.; Lopez, G.; Perez, J.; Molins, E. *Inorg. Chim. Acta* **1999**, *287*, 37–46.

(97) Nosova, V. M.; Ustynyuk, Y. A.; Bruk, L. G.; Temkin, O. N.; Kisin, A. V; Storozhenko, P. A. *Inorg. Chem.* **2011**, *50*, 9300–9310.

(98) Serrano, J. L.; Fairlamb, I. J. S.; Sánchez, G.; García, L.; Pérez, J.; Vives, J.; López, G.; Crawforth, C. M.; Taylor, R. J. K. *Eur. J. Inorg. Chem.* **2004**, 2706–2715.

(99) Bandini, A.; Banditelli, G.; Cinellu, M. A.; Sanna, G.; Minghetti, G.; Demartin, F.; Manassero, M. *Inorg. Chem.* **1989**, *28*, 404–410.

(100) Bergamini, P.; Sostero, S.; Traverso, O.; Kemp, T. J.; Pringle, P. G. *J. Chem. Soc. Dalt.* **1989**, 2017–2021.

(101) Bandini, A.; Banditelli, G.; Demartin, F.; Manassero, M.; Minghetti, G. *Gazz. Chim. Ital.* **1993**, *123*, 417–423.

(102) Longato, B.; Montagner, D.; Bandoli, G.; Zangrando, E. *Inorg. Chem.* **2006**, *45*, 1805–1814.

(103) Eychenne-Baron, C.; Ribot, F.; Nathalie, S.; Sanchez, C. *Organometallics* **2000**, *19*, 1940–1949.

(104) Mishra, S.; Daniele, S.; Hubert-Pfalzgraf, L. G.; Jeanneau, E. *Eur. J. Inorg. Chem.* **2007**, *15*, 2208–2215.

(105) Schneider, J.; Hagen, J.; Czap, N.; Kruger, C.; Mason, S.; Bau, R.; Ensling, J.; Gutlich, P.; Wrackmeyer, B. *Chem. Euro. J.* **2000**, *6*, 625–635.

(106) Jones, D. F.; Dixneuf, P. H.; Benoit, A.; Le Marouille, J. *Inorg. Chem.* **1983**, *22*, 29–33.

(107) Park, Y. J.; Cook, S. A.; Sickerman, N. S.; Sano, Y.; Ziller, J. W.; Borovik, A. S. *Chem. Sci.* **2013**, *4*, 717–726.

(108) Parzuchowski, P. G.; Kampf, J. W.; Roźniecka, E.; Kondratenko, Y.; Malinowska, E.; Meyerhoff, M. E. *Inorg. Chim. Acta* **2003**, *355*, 302–313.

(109) Preetz, A.; Baumann, W.; Drexler, H.-J.; Fischer, C.; Sun, J.; Spannenberg, A.; Zimmer, O.; Hell, W.; Heller, D. *Chem. Asian J.* **2008**, *3*, 1979–1982.

(110) Wang, L.; Sheng, T.; Zhang, J.; Hu, S.; Fu, R.; Wu, X.; Li, Y.; Huang, X.; Xiang, S. *Polyhedron* **2007**, *26*, 1098–1104.

(111) Vasiliu, M.; Knope, K. E.; Soderholm, L.; Dixon, D. A. *J. Phys. Chem. A* **2012**, *116*, 6917–6926.

(112) Mishra, S.; Jeanneau, E.; Daniele, S.; Hubert-Pfalzgraf, L. G. *CrystEngComm* **2008**, *10*, 814–816.

(113) Mishra, S.; Hubert-Pfalzgraf, L. G.; Daniele, S.; Rolland, M.; Jeanneau, E.; Jouguet, B. *Inorg. Chem. Commun.* **2009**, *12*, 97–100.

(114) Martinez, J.; Aiello, I.; Bellusci, A.; Crispini, A.; Ghedini, M. *Inorg. Chim. Acta* **2008**, *361*, 2677–2682.

(115) Hoveyda, H.; Rettig, S.; Orvig, C. *Inorg. Chem.* **1993**, *32*, 4909–4913.

(116) *The Group 13 Metals Aluminium, Gallium, Indium, and Thallium: Chemical Patterns and Peculiarities*; Aldridge, S.; Downs, A. J., Eds.; A John Wiley and Sons, Ltd., Publication: Chichester, 2011; pp. 52–55.

(117) Carnes, M. E.; Knutson, C. C.; Nadarajah, A.; Jackson, M. N.; Oliveri, A. F.; Norelli, K. M.; Crockett, B. M.; Bauers, S. R.; Moreno-Luna, H. A.; Taber, B. N.; Pacheco, D. J.; Olson, J. Z.; Brevick, K. R.; Sheehan, C. E.; Johnson, D. W.; Boettcher, S. W. *J. Mater. Chem. C* **2014**, *2*, 8492–8496.

(118) Furrer, G.; Phillips, B. L.; Ulrich, K.-U.; Pöthig, R.; Casey, W. H. *Science* **2002**, *297*, 2245–2247.

(119) Gebauer, D.; Völkel, A.; Cölfen, H. *Science* **2008**, *322*, 1819–1822.

(120) Bulewicz, E. M.; Sugden, T. M. *Trans. Faraday Soc.* **1958**, *54*, 830–837.

(121) Jiang, K.; Zakutayev, A.; Stowers, J.; Anderson, M. D.; Tate, J.; McIntyre, D. H.; Johnson, D. C.; Keszler, D. A. *Solid State Sci.* **2009**, *11*, 1692–1699.

(122) Meyers, S. T.; Anderson, J. T.; Hong, D.; Hung, C. M.; Wager, J. F.; Keszler, D. A. *Chem. Mater.* **2007**, *19*, 4023–4029.

(123) Anderson, J. T.; Munsee, C. L.; Hung, C. M.; Phung, T. M.; Herman, G. S.; Johnson, D. C.; Wager, J. F.; Keszler, D. A. *Adv. Funct. Mater.* **2007**, *17*, 2117–2124.

(124) Alemayehu, M.; Davis, J. E.; Jackson, M.; Lessig, B.; Smith, L.; Sumega, J. D.; Knutson, C.; Beekman, M.; Johnson, D. C.; Keszler, D. A. *Solid State Sci.* **2011**, *13*, 2037–2040.

(125) Nadarajah, A.; Carnes, M. E.; Kast, M. G.; Johnson, D. W.; Boettcher, S. W. *Chem. Mater.* **2013**, *25*, 4080.

(126) Murugavel, R.; Walawalkar, M. G.; Dan, M.; Roesky, H. W.; Rao, C. N. R. *Acc. Chem. Res.* **2004**, *37*, 763–774.

(127) Fujdala, K. L.; Tilley, T. D. *J. Am. Chem. Soc.* **2001**, *123*, 10133–10134.

(128) Sekar, P.; Greyson, E. C.; Barton, J. E.; Odom, T. W. *J. Am. Chem. Soc.* **2005**, *127*, 2054–2055.

(129) Kim, H. S.; Byrne, P. D.; Facchetti, A.; Marks, T. J. *J. Am. Chem. Soc.2* **2008**, *130*, 12580–12581.

(130) Smith, S. W.; Wang, W.; Keszler, D. W.; Conley Jr., J. F. *Vac. Sci. Technol., A.* **2014**, *32*, 041501.

(131) Wang, W.; Chang, I. Y.; Zakharov, L.; Cheong, P. H.-Y.; Keszler, D. A. *Inorg. Chem.* **2013**, *110*, 18397.

(132) Wang, W.; Liu, W.; Chang, I. Y.; Wills, L. A.; Zakharov, L. N.; Boettcher, S. W.; Cheong, P. H.-Y.; Fang, C.; Keszler, D. A. *Proc. Natl. Cad. Sci. U. S. A.* **2013**, *110*, 18397.

(133) Hu, C.; Liu, H.; Qu, J. *Colloids Surf., A.* **2005**, *260*, 109–117.

(134) Pourbaix, M. *Atlas of Electrochemical Equilibria in Aqueous Solutions*; 2nd Egnlis.; National Association of Corrosion Engineers: Houston, 1974.

(135) Saltman, W. M.; Nachtrieb, N. H. *J. Electrochem. Soc.* **1953**, *100*, 126–130.

(136) Pretsch, E.; Buhlmann, P.; Badertscher, M. *Structure Determination of Organic Compounds: Tables of Spectral Data*; 4th Editio.; Springer-Verlag: Berlin, 2009.

(137) Da Cunha, M. C. P. M.; De Souza, J. P. I.; Nart, F. C. *Langmuir* **2000**, *15*, 771–777.

(138) *Standard Potentials in Aqueous Solutions*; Bard, A. J.; Parsons, R.; J., J., Eds.; International Union of Pure and Applied Chemistry, 1985.

(139) Mahle, T. Metallic and bimetallic catalysts for electrochemical reduction of problematic aqueous anions, University of Illinois, Urbana-Champagne, 2012.

(140) Hong, D.; Yerubandi, G.; Chiange, H. Q.; Spiegelberg, M. C.; Wager, J. F. *Crit. Rev. Solid State Mater. Sci.* **2008**, *33*, 101–132.

(141) Henry, M.; Jolivet, J. P.; Livage, J. *Aqueous Chemistry of metal Cations: Hydrolysis, Condenstation and Complexation, Structure and Bonding*; Springer-Verlag: Berlin, 1992.

(142) Kim, M.-G.; Kanatzidis, M. G.; Facchetti, A.; Marks, T. J. *Nat. Mater.* **2011**, *10*, 382.

(143) Hwang, Y. H.; Seo, J.-S.; Yun, J. M.; Park, H.; Yang, S.; Park, S.-H. K.; Bae, B.-S. *NPG Asia Mater.* **2013**, *5*, e45.

(144) Kamiya, T.; Hosono, H. *NPG Asia Mater.* **2010**, *2*, 15.

(145) Rim, Y. S.; Chen, H.; Kou, X.; Duan, H.-S.; Zhou, H.; Cai, M.; Kim, H. J.; Yang, Y. *Adv. Mater.* **2014**, *26*, 4273.

(146) Street, R. A.; Ng, T. N.; Lujan, R. A.; Son, I.; Smith, M.; Kim, S.; Lee, T.; Moon, Y.; Cho, S. *ACS Appl. Mater. Interfaces* **2014**, *6*, 4428.

(147) Bradley, S. M.; Kydd, R. A.; Yamdagni, R. *J. Appl. Cryst.* **1990**, 413.

(148) Michot, L. J.; Montargès-Pelletier, E.; Lartiges, B. S.; d'Espinose de la Caillerie, J.-B.; Briois, V. *J. Am. Chem. Soc.* **2000**, *122*, 6048–6056.

(149) Seichter, W.; Mögel, H.; Brand, P.; Salah, D. *Eur. J. Inorg. Chem.* **1998**, *13*, 795–797.